Multi-particle Collision Dynamics for Microflows

A Thesis
Submitted for the Degree of
Master of Science (Engineering)

by

Vicky Kumar Verma

Engineering Mechanics Unit
Jawaharlal Nehru Centre for Advanced Scientific Research
(A Deemed University)
Bangalore – 560 064

DECEMBER 2014

Dedicated to my parents.

DECLARATION

I hereby declare that the matter embodied in the thesis entitled "**Multi-particle Collision Dynamics for Microflows**" is the result of investigations carried out by me at the Engineering Mechanics Unit, Jawaharlal Nehru Centre for Advanced Scientific Research, Bangalore, India under the supervision of **Dr. Santosh Ansumali** and that it has not been submitted elsewhere for the award of any degree or diploma.

In keeping with the general practice in reporting scientific observations, due acknowledgment has been made whenever the work described is based on the findings of other investigators.

Vicky Kumar Verma

CERTIFICATE

I hereby certify that the matter embodied in this thesis entitled "**Multi-particle Collision Dynamics for Microflows**" has been carried out by **Mr. Vicky Kumar Verma** at the Engineering Mechanics Unit, Jawaharlal Nehru Centre for Advanced Scientific Research, Bangalore, India under my supervision and that it has not been submitted elsewhere for the award of any degree or diploma.

Dr. Santosh Ansumali
(Research Supervisor)

Acknowledgements

First and foremost, I would like to thank my research advisor Dr. Santosh Ansumali for his continued guidance all through my work. His keen insights helped me approach problems systematically and his valuable suggestions kept me on the right path. It would have been really difficult to finish this work without his active involvement. I also express my gratitude to Prof. V. Kumaran (Chemical Engineering, IISc) and Prof. Ganesh Subramanian for fruitful discussions on multi-particle collision dynamics, which helped me develop a better understanding of the method.

In completing my thesis, I have received help from many of my friends and colleagues, and I take this opportunity to thank them all. In particular, I am thankful to my research group members - Shiwani, Manjusha, Siddharth, Reddy, Praveen, Mahan, and Shailendra for sharing ideas and experiences with me, and to my lab-mates - Rajesh, Prashanth, Deepak, and Milind, who have always helped me in my needs.

Getting through the research work over past two and half years have required more than just academic support. I am indebted to all my friends for their company inside and outside the campus, for listening to my doubts, giving suggestions, motivating me all the time, and at times tolerating me. I would like to thank Ponnu, Deepthi, Dhiraj, Navaneeth, Sarada, Sona, Meha, Kanwar, Sankalp, Shashi Kiran for their unwavering personal support, and making my stay at JNC a memorable one. I am also thankful to Priyesh for always motivating me despite being far, far away. Our friendship has only grown stronger since undergraduate days. I am also grateful to my flute teacher. It is under his tutelage, I have started my journey in the realm of music.

Apart from academics, my life in JNC has been a good learning experience, as I worked with my colleagues in different student bodies. During my first year, I enjoyed working with Sankalp, Shashi Kiran, Alok, Meenakshi, Abhijit, and Subhajit as a member of sports committee. Later, in second year, I shared responsibilities of being a student representative along with my colleagues - Piyush, Shveta, Anuj, Ananthu, and Ram. Working with them had been a wonderful experience. I am indebted to their cooperation and help, which permitted me to fulfill my duties while managing my research work.

I appreciate the effort of administrative staff and the library staff for making things easier for students. I also thank hostel staff and mess workers for making JNC hostel a comfortable place to live in.

Finally, I would like to thank my parents for their unconditional love and support. Furthermore, I would like to thank Priyanka for her help and support, specially towards the end of my thesis. Their encouragement has always kept me going whenever I was feeling down.

Abstract

Multiparticle collision dynamics (MPCD) is a particle based mesoscopic simulation technique for incorporating hydrodynamics and thermal fluctuations in complex fluid simulations. Due to its simplicity, the MPCD algorithm has become quite popular in the study of complex flow problems. In this thesis, kinetic nature of the algorithm is investigated for quantitative accuracy in case of flows at finite Knudsen numbers. In particular, microflow set-ups such as shear, gravity, and pressure driven flows have been used for the study, and the algorithm is benchmarked against the well know analytical and numerical results. In addition, the effectiveness of bounce back and diffuse wall boundary conditions are investigated for the above mentioned canonical flows.

Here, we also present a new collision scheme in the framework of MPCD, termed as Pseudo Binary Collision Model (PBCM), which ensures Galilean invariance for the system at small time steps. In standard MPCD, velocity correlations start building up among particles when the time step is small enough that the particles move only a fraction of the cell size of the grid used. These correlations in turn lead to the failure of Galilean invariance, and the system shows unphysical behaviour. By numerical means, we have shown that the performance of MPCD method improves substantially by the use of pseudo binary collision model in simulations with small time steps.

Finally, we show how the ideal gas equation of state of an MPCD fluid can be modified to a general non-ideal equation of state. Here, we have used a phenomenological mean field model for incorporating excluded volume effect into the system. In particular, we have used the Van der Waals and Carnahan-Starling equations of state for including the excluded volume effect into the MPCD system, and also the effectiveness of this approach is investigated. In addition, the effect of attraction between molecules is included by considering a Vlasov type force on the particles. With these changes a two phase system, condensation of a gas into liquid, is studied using MPCD. The study of Maxwell construction shows excellent agreement with the theory.

Contents

Chapter 1

Introduction

1.1 Motivation

Multiparticle collision dynamics (hereafter MPCD) is a particle based mesoscopic simulation tool introduced a decade back by Malevanets and Kapral as a convenient and efficient way of incorporating hydrodynamics and thermal fluctuations in complex fluid simulations (Malevanets & Kapral 1999, 2000). The system has discrete time dynamics; during each time step particles are streamed and multiparticle collisions are performed. They also showed that multiparticle collisions conserve mass, momentum, and energy and equilibrium distribution is given by the Maxwell-Boltzmann distribution. Similar to Boltzmann dynamics, an H-theorem is shown to hold for this model too. These microscopic consistencies in MPCD algorithm ensure that correct hydrodynamics corresponding to Navier-Stokes-Fourier model is recovered for an ideal gas system at macroscopic length and time scales (Malevanets & Kapral 1999; Ihle 2009). Due to simplicity of the update rules, it is possible to derive analytical expressions for transport coefficients which agree quite well with simulation results (Ihle & Kroll 2003*b*; Kikuchi *et al.* 2003). Transport coefficients are derived following two alternative approaches-discrete time projection operator approach (Ihle & Kroll 2003*a*,*b*) and kinetic theory approach (Kikuchi *et al.* 2003; Pooley & Yeomans 2005). The two alternative approaches are complementary to each other and coefficients obtained are in good agreement. The MPCD algorithm has been successfully applied to simulate various complex systems such as colloids (Padding & Louis 2006; Hecht *et al.* 2005, 2006), polymers (Mussawisade *et al.* 2005; Lee & Kapral 2006; Kikuchi *et al.* 2005; Ryder & Yeomans 2006), vesicles (Noguchi & Gompper 2005*a*,*b*), and reactive flows (Tucci & Kapral 2004). Thus the method can be viewed as a minimal microscopic model of fluid. For a comprehensive review on MPCD, readers are referred to Kapral (2008); Gompper *et al.* (2008).

Despite the success of MPCD model in complex fluid applications, a number of technical as well as conceptual issues remain. For example, though the method has its origin in kinetic theory, the range of applicability for finite Knudsen is not well understood. The aim of this thesis is to quantify the accuracy of the MPCD algorithm and resolve some of the problems associated with it (for example, specifying correct equation of state).

In particular, following issues are studied in this thesis:

- **Equation of State:** MPCD has been applied to a variety of problems such as colloidal suspensions, dilute polymer solutions, and flows in channels and over solid objects. We note that in most of these applications MPCD is used to mimic liquid like properties, although the equation of state (in MPCD) is that of an ideal gas. Therefore, the results

presented in literature correspond to systems evaluated at artificially high Mach numbers for numerical convenience. This thesis attempts to modify the equation of state of MPCD system using a phenomenological model which incorporates volume effect of the particles in the mean sense while working with point particles. Unlike Enskog system the excluded volume effect is introduced by changing the streaming velocity instead of treating them during the collision step as is conventionally done (Alexander *et al.* 1995). We have also included contribution due to attractive part of the molecular potential into the system. This modification has allowed us to use MPCD to simulate problems involving phase separation.

- **Boundary condition:** In kinetic theory, wall boundary conditions are often implemented via diffusive boundary condition (Alexander & Garcia 1997; Ansumali & Karlin 2002). In this boundary condition, one assumes that particles coming into the flow after wall interaction are distributed according to the Maxwell-Boltzmann distribution at the wall temperature. Thus the wall acts like a thermostat, and the thermal boundary condition is that of constant temperature. However, for mesoscale methods with bounce back boundary condition, where particles reverse their velocity directions after collision, provides an alternate framework for implementing no-slip boundary condition. This boundary condition mimics adiabatic condition as no energy exchange happens with the wall. In MPCD method, the most widely used boundary condition is bounce-back boundary condition. In this thesis, effectiveness of both boundary conditions are investigated for certain canonical flows.

- **Domain of Validity:** In addition to their importance in engineering applications as well as in scientific investigations, microflows also provide an important check for the kinetic nature of an algorithm. Microflow setups have already been used to benchmark DSMC (Direct Simulation Monte Carlo) (Piekos & Breuer 1996) and LBM (Lattice Boltzmann Method) (Nie *et al.* 2002; Lim *et al.* 2002; Ansumali *et al.* 2006). Here one of our main objectives is to study the kinetic nature of MPCD algorithm. In this thesis we have investigated this method for gaseous microflows to access its accuracy in a quantitative fashion. In this regard, we have chosen the set-up of shear driven flows, gravity driven flows, and pressure driven flows at finite Knudsen numbers, as test cases.

- **Galliean Invariance and Need of a New Collision Model:** Simulations using the conventional MPCD algorithm exhibits anomalous behavior for low temperature and small time steps (Ihle & Kroll 2001). The dependence of the algorithm on a grid for calculating cell centre velocities is speculated to be the main reason behind this failure when the grid is kept fixed. The use of a fixed grid makes the grid an important element for simulating a flow. This grid dependence is conventionally circumvented by shifting the grid before every collision. This method of grid-shift works well under the conditions in which use of a fix grid otherwise gives unphysical behaviour. However, using this method makes the algorithm more complicated especially for domains with wall boundary condition.

  In this thesis, we present a simple solution to this problem by modifying the collision rule of MPCD while maintaining the simplicity of the algorithm. This new collision model

(pseudo binary collision) is motivated by Monte Carlo binary collision model for plasma dynamics (Wang *et al.* 2008). In this collision model, MPCD multiparticle collisions have been replaced with binary collisions. This removes any grid dependence in performing collisions. The main role of the grid then is to coarse-grain the system, and to sample macroscopic flow properties.

1.2 Overall organization of the thesis

The overall organization of the thesis is as follows

- In Chapter 2, MPCD algorithm is introduced, and derivation of viscosity based on kinetic theory is outlined. In addition, some of the practical aspects related to using the method such as setting MPCD parameters, sampling macroscopic quantities, and the use of grid shift and ghost particles are discussed.

- In Chapter 3, MPCD is benchmarked for simulating microflows. Three different microflow setups are used - shear flow, gravity driven flow, and pressure driven flow. The results in each case are presented.

- In Chapter 4, a new collision model is presented for correcting MPCD anomalous behaviour for low temperatures and small time steps. We have also studied the equilibrium configuration of the system. Analytical expressions for kinetic and collisional viscosities are derived. Finally, we have studied microflow systems using this collision model. In this study also, we have used three canonical flow arrangements - shear driven flow, gravity driven flow, and pressure driven flow.

- In chapter 5, MPCD is modified for incorporating volume effect of the molecules in the mean sense by changing the streaming step. First, the phenomenological mean field model for incorporating Enskog like dynamics is introduced. The equation of state of the modified MPCD system is then studied; changes in the viscosity is also investigated and compared with the theory. Furthermore, speeds of sound in the modified system is studied. Finally, MPCD system is extended to include the effect of attractive forces between molecules, and the phase separation problem is investigated.

- In Chapter 6, an overview of the work done in this thesis is presented, and a few suggestions are made for future work.

Chapter 2

Multi-particle Collision Dynamics

2.1 Introduction

Multiparticle collision dynamics (MPCD) is a particle based mesoscopic simulation technique for incorporating hydrodynamics and/or thermal fluctuations into a system such as colloidal suspension (Malevanets & Kapral 1999, 2000; Kapral 2008). In this algorithm, fluid is modeled by a finite number (N) of point particles with positions $\mathbf{r}_i$ and velocities $\mathbf{v}_i$, where $i = 1, 2, ..., N$. The system evolves in a continuous phase space but discrete time domain following two steps - streaming and collision- repeatedly. In the streaming step, positions of the particles are updated as

$$\mathbf{r}_i(t + \delta t) = \mathbf{r}_i(t) + \mathbf{v}_i(t)\delta t \tag{2.1}$$

where $\mathbf{r}_i(t + \delta t)$ are the updated positions of the particles moving with velocities $\mathbf{v}_i(t)$ over time interval δt. This step mimics free flight of the particles. During streaming step, particles do not interact and in fact they can even pass through each other unaffected.

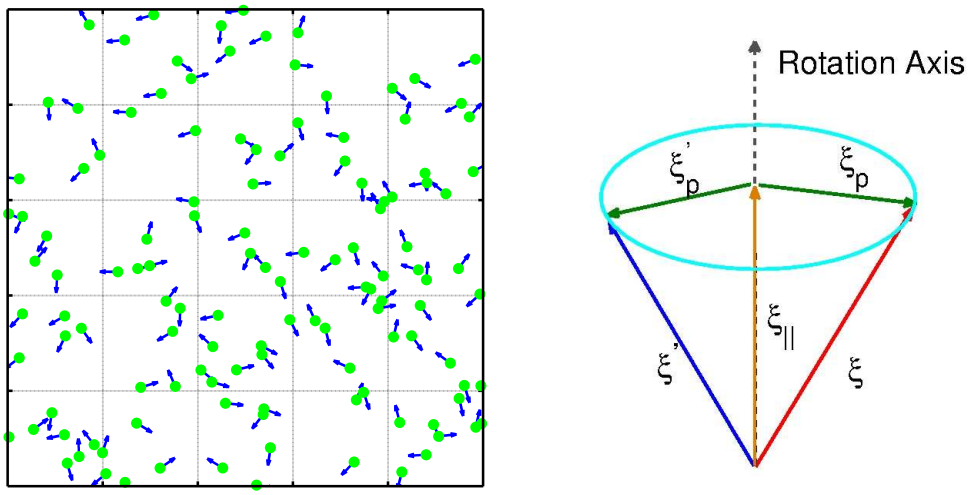

(a) (b)

Figure 2.1: *Multiparticle collision dynamics model. (a) Depicting simulation domain with particles sorted into different cells. (b) Schematic diagram of the velocity rotation. ξ is the particle velocity in the reference frame moving with cell velocity, $\xi_{||}$ and ξ_p are the components of ξ along and perpendicular to the rotation axis, respectively. ξ' is the final velocity after rotation which is the vector sum of $\xi_{||}$ and ξ_p', where the second component is generated by the anti-clockwise rotation of ξ_p about the rotation axis by a constant angle α. In the figure, both $|\xi_p|$ and $|\xi_p'|$ lie on the circle.*

In order to perform collisions, particles are first sorted into cells (collision cells) which divide the domain into a regular lattice. During this step, all the particles in a given cell interact with each other via momentum exchange. The velocity of each particle in a cell is then rotated by a constant angle (α) around a randomly chosen axis in a frame of reference moving with the cell velocity (average velocity of particles in a given cell) defined as:

$$\mathbf{u}^{(I)}(t) = \frac{1}{N^I}\sum_{i=1}^{N^I}\mathbf{v}_i(t). \tag{2.2}$$

Thus in collision step, all the particles inside a collision cell get affected and the velocity of each particle is updated as

$$\mathbf{v}_i^{(I)}(t+\delta t) = \mathbf{u}^{(I)}(t) + \mathbf{R}(\alpha)(\mathbf{v}_i^{(I)}(t) - \mathbf{u}^{(I)}(t)) \tag{2.3}$$

where, $\mathbf{R}(\alpha)$ is an orthogonal rotation matrix characterized by a given rotation angle α, and a randomly chosen axis $\mathbf{n}$. We assume $\mathbf{n}$ to be uniformly distributed over a sphere of unit radius. Furthermore, rotation axes in a cell at different time steps are stochastically independent. They are also independent for different cells at a given time step. All macroscopic observables are defined by an appropriate average value inside the cell. For example, the density ($\rho^{(I)}$), and internal energy ($e^{(I)}$) are calculated as:

$$\rho^{(I)} = \frac{N^{(I)}m}{V}, \quad e^{(I)} = \sum_{i=1}^{N^{(I)}}\frac{(\mathbf{v}_i^{(I)} - \mathbf{u}^{(I)})^2}{N^{(I)}}. \tag{2.4}$$

The chapter is organized as follows: In section 2.2 some of the useful properties of collision operator is discussed. In section 2.3, procedure for deriving viscosity expression based on kinetic theory is described. Use of grid shift and ghost particles are discussed in sections 2.4 and 2.5. Finally, a few issues associated with the implementation of MPCD is discussed in section 2.6.

2.2 Properties of Collision Model

By construction, the chosen collision model (Eq.(2.3)) conserves mass, momentum and energy. The momentum conservation can be seen by explicitly summing the post collision velocities of all the particle in Ith cell as

$$\sum_{i=1}^{N^I} v_{ij}^{(I)}(t+\delta t) = N^I\, u_j^{(I)}(t) + R_{jk}(\alpha)\left(\sum_{i=1}^{N^I} v_{ik}^{(I)}(t) - u_k{}^{(I)}(t)\right) = \sum_{i=1}^{N^I} v_{ij}^{(I)}(t), \tag{2.5}$$

where subscript j denotes jth component of the velocity and $\mathbf{u}^{(I)}(t) = \sum_{i=0}^{N^I}\mathbf{v}_i(t)/N^I$ is used to eliminate $\mathbf{u}^{(I)}(t)$. Similarly, energy conservation in the model can be seen by evaluating fluctuating part of the energy at time $t+\delta t$ as:

$$\sum_{i=1}^{N^I}\left(v_{ij}^{(I)} - u_j^{(I)}\right)^2\Bigg|_{t+\delta t} = \sum_{i=1}^{N^I} R_{jk}R_{jl}\left(v_{ik}^{(I)}(t) - u_k{}^{(I)}(t)\right)\left(v_{il}^{(I)}(t) - u_l{}^{(I)}(t)\right). \tag{2.6}$$

Thus, we see that the energy is conserved via time dynamics provided

$$R_{jk}R_{jl} = \delta_{kl}, \tag{2.7}$$

which is the condition that R is an orthogonal matrix. Thus, the basic requirement of hydrodynamics that the collision model has correct conservation laws is satisfied for MPCD algorithm. In addition, similar to Boltzmann systems, an H-theorem has been proved to exist for the system (Malevanets & Kapral 1999).

Next we consider the explicit expression of orthogonal matrix R used in the simulations. In 2D, rotation axis is fixed in orientation and is aligned with the direction in which system properties do not change. As a result, the collision operation is simply rotation of peculiar velocity $\boldsymbol{\xi} = (\mathbf{v}(t) - \mathbf{u})$, by a constant angle in clockwise (positive α) or counter-clockwise (negative α) directions; the direction of rotation is chosen randomly with equal probability. Thus, $\mathbf{R}(\alpha)$ is given by

$$\mathbf{R}(\alpha) = \begin{pmatrix} \cos\alpha & \pm\sin\alpha \\ \mp\sin\alpha & \cos\alpha \end{pmatrix}. \tag{2.8}$$

In three-dimensions, the explicit form of $\mathbf{R}(\alpha)$, which depends both on α and $\hat{\mathbf{n}}$, is:

$$\mathbf{R}(\alpha) = \begin{pmatrix} \cos\alpha + n_1^2(1-\cos\alpha) & n_1n_2(1-\cos\alpha) - n_3\sin\alpha & n_1n_3(1-\cos\alpha) + n_2\sin\alpha \\ n_1n_2(1-\cos\alpha) + n_3\sin\alpha & \cos\alpha + n_2^2(1-\cos\alpha) & n_2n_3(1-\cos\alpha) - n_1\sin\alpha \\ n_1n_3(1-\cos\alpha) - n_2\sin\alpha & n_2n_3(1-\cos\alpha) + n_1\sin\alpha & \cos\alpha + n_3^2(1-\cos\alpha) \end{pmatrix} \tag{2.9}$$

As we have mentioned before, $\mathbf{n}$ is chosen such that the unit vector is distributed uniformly over a sphere of unit radius. Thus, the stochastic rotation axis is set by generating two random numbers, ϕ and θ, distributed uniformly in $(0, 2\pi)$ and $(-1, 1)$, respectively. The three components of $\mathbf{n} = (n_1, n_2, n_3)$ are given by

$$n_1 = \sqrt{1-\theta^2}\cos(\phi), \quad n_2 = \sqrt{1-\theta^2}\sin(\phi), \quad n_3 = \theta. \tag{2.10}$$

We also emphasize here that use of the rotation matrix (Eq.(2.9)) is numerically unstable. Instead, geometrical construction shown in Fig.(2.1b) is used for computing the post collision velocities. Thus the post collision velocity is given by

$$\mathbf{v}(t+\delta t) = \mathbf{u} + \boldsymbol{\xi}_{\parallel} + \boldsymbol{\xi}_{\perp}\cos\alpha + (\mathbf{n}\times\boldsymbol{\xi}_{\perp})\sin\alpha, \tag{2.11}$$

where $\boldsymbol{\xi} = \mathbf{v}(t) - \mathbf{u}(t)$ is the velocity of a particle in a reference frame moving with the cell velocity, $\boldsymbol{\xi}_{\parallel} = \mathbf{n}(\boldsymbol{\xi}\cdot\mathbf{n})$, $\boldsymbol{\xi}_{\perp} = \boldsymbol{\xi} - \mathbf{n}(\boldsymbol{\xi}\cdot\mathbf{n})$, and $(\mathbf{n}\times\boldsymbol{\xi}_{\perp})$ is the cross-product between vectors $\mathbf{n}$ and $\boldsymbol{\xi}_{\perp}$.

2.3 Transport Properties

Simplicity of update rules in MPCD algorithm has allowed the study of the system for its transport properties (Kikuchi *et al.* 2003; Ihle & Kroll 2003*a*,*b*). Analytical expressions for transport coefficients of different transport processes such as mass transport (mass diffusion),

momentum transport (viscosity), and energy transport (thermal diffusion) have been derived. These expressions show quite good agreement with simulation data (Kikuchi *et al.* 2003; Ihle & Kroll 2003*b*). In this section, following Kikuchi *et al.* (2003) the procedure used for deriving viscosity of MPCD system is outlined.

Firstly, it should be pointed out that unlike kinetic description of a real fluids, fluid modeled by MPCD has two distinct contributions to the viscosity. The first contribution, which is often referred to as kinetic contribution, is due to transport of momentum by the movement of particles. The second contribution, termed as collisional viscosity, is due to the non-local nature of discrete collisions. While kinetic contribution is present for molecular fluid, the second contribution is purely a numerical artifact. Here, we remind that this non-locality is not similar to Enskog type non-locality (Chapman *et al.* 1970) and does not introduce any correction to the equation of state. In this section, we follow Kikuchi *et al.* (2003), to derive the viscosity of MPCD fluid.

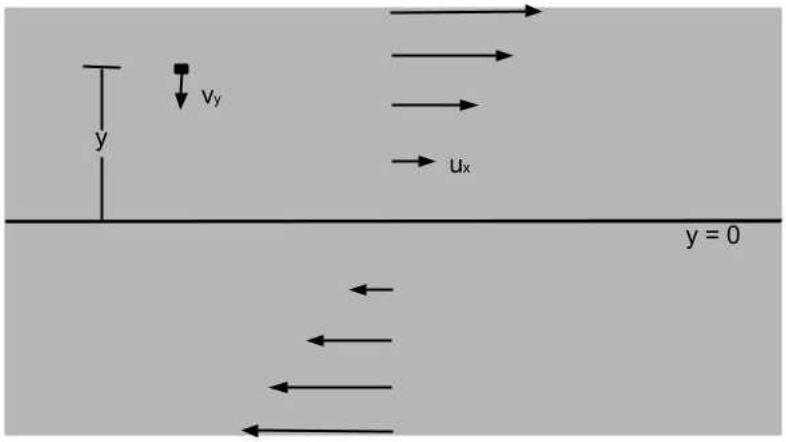

Figure 2.2: *Schematic diagram of shear flow.*

Kinetic Viscosity

In order to calculate the kinetic part of the viscosity we consider a system undergoing shear in x-direction with shear rate $\dot{\gamma} = \partial u_x(y)/\partial y$ as shown in Fig.(2.2). If we consider any plane at a given y, because of thermal fluctuations, fluid particles cross the plane from both sides carrying momentum along with them. However, on an average, particles crossing the plane from above have different x-momentum compared to those crossing the plane from below because of the applied shear. Consequently, there is a net flux of momentum across the surface in x-direction and a non-zero shear force is experienced by the surface, which can be expressed as

$$\sigma_{xy} = \eta \frac{\partial u_x(y)}{\partial y} \equiv \eta \dot{\gamma}, \tag{2.12}$$

where η is shear viscosity.

We aim to calculate this contribution to the viscosity hereafter termed as kinetic viscosity, η_{kin}, by analyzing the relationship between shear stress σ_{xy} and strain rate $\dot{\gamma}$ at location y, as the particles stream. It can be accomplished by computing total momentum flux crossing the plane y in x-direction; the shear stress at y is negative of this quantity. For simplicity, we

consider a given plane $y = y_0 = 0$. A particle at coordinate $\mathbf{x} \equiv (x, y)$ crosses the plane y_0 in the time interval δt provided it is moving towards the plane and the magnitude of y component of the velocity is greater than $|y|/\delta t$ where $|y|$ corresponds to the magnitude of y. Furthermore, we need to know the local density, $\rho = mM/a^2$, where M is the average number of particles per collision cell, and local velocity distribution function $P(\xi_x, \xi_y)$, in order to calculate the total flux through y_0. Note that the local distribution function $P(\xi_x, \xi_y)$ is normalized to unity. The shear stress at $y = y_0$ is

$$\begin{aligned}\sigma_{xy} = &-\frac{\rho}{\delta t}\int_{-\infty}^{\infty} dv_x \int_{-\infty}^{0} dy \int_{-\frac{y}{\delta t}}^{\infty} dv_y v_x P(v_x - \dot{\gamma} y, v_y) \\ &+\frac{\rho}{\delta t}\int_{-\infty}^{\infty} dv_x \int_{0}^{\infty} dy \int_{-\infty}^{-\frac{y}{\delta t}} dv_y v_x P(v_x - \dot{\gamma} y, v_y);\end{aligned} \tag{2.13}$$

The first integral on the right hand side denotes contribution to x-momentum flux from the particles in the region $y < 0$ as they move across the plane y_0 (notice that in this integral v_y is positive since y is negative). Similarly, in the second integral x-momentum flux contribution is calculated by the particles in the region $y > 0$. Also note that we have subtracted $\dot{\gamma} y$, which is the flow velocity at y, from the x-component of the particle velocity v_x since the distribution function considered here is written in the co-moving reference frame. By change of variables $(v_x - \dot{\gamma} y, v_y)$ to (ξ_x, ξ_y), the above equation is reduced to

$$\begin{aligned}\sigma_{xy} = &-\frac{\rho}{\delta t}\int_{-\infty}^{\infty} d\xi_x \int_{-\infty}^{0} dy \int_{-\frac{y}{\delta t}}^{\infty} d\xi_y (\xi_x + \dot{\gamma} y) P(\xi_x, \xi_y) \\ &+\frac{\rho}{\delta t}\int_{-\infty}^{\infty} d\xi_x \int_{0}^{\infty} dy \int_{-\infty}^{-\frac{y}{\delta t}} d\xi_y (\xi_x + \dot{\gamma} y) P(\xi_x, \xi_y).\end{aligned} \tag{2.14}$$

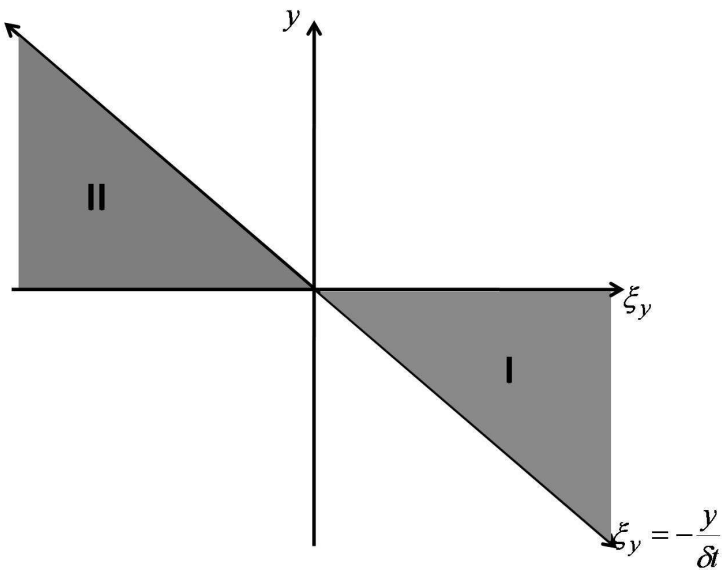

Figure 2.3: *Schematic diagram depicting region of integration (Eq.(2.14)) in ξ-y plane.*

Next, changing the order of integration between ξ_y and y (see Fig.(2.3)), the above equation

simplifies as

$$\begin{aligned}
\sigma_{xy} &= -\frac{\rho}{\delta t}\int_{-\infty}^{\infty} d\xi_x \int_{0}^{\infty} d\xi_y \int_{-\xi_y\delta t}^{0} dy(\xi_x + \dot{\gamma}y)P(\xi_x,\xi_y) \\
&\quad +\frac{\rho}{\delta t}\int_{-\infty}^{\infty} d\xi_x \int_{-\infty}^{0} d\xi_y \int_{0}^{-\xi_y\delta t} dy(\xi_x + \dot{\gamma}y)P(\xi_x,\xi_y) \\
&= \frac{\rho}{\delta t}\int_{-\infty}^{\infty}\int_{-\infty}^{\infty} d\xi_x d\xi_y(-\xi_x\xi_y\delta t + \dot{\gamma}\frac{\xi_y^2\delta t^2}{2})P(\xi_x,\xi_y) \\
&= \frac{\dot{\gamma}\rho\delta t}{2}\langle\xi_y^2\rangle - \rho\langle\xi_x\xi_y\rangle = \frac{\dot{\gamma}\rho\delta t}{2}\langle v_y^2\rangle - \rho\langle v_x v_y\rangle
\end{aligned} \tag{2.15}$$

where we have used the fact that the peculiar velocity (ξ_x, ξ_y) is same as the particle velocity (v_x, v_y) at $y = 0$.

Finally, the behavior of $\langle v_x v_y\rangle$ can be computed by considering the effects of streaming and collision separately. For simplicity, $\dot{\gamma}$ is assumed to be positive and a frame of reference moving with the flow velocity at any given y is chosen. In a time interval of δt, particles with positive v_y come from $y - v_y\delta t$, and have comparatively smaller flow velocity. In other words, as a particle moves in the positive y direction, a part of x component of the peculiar velocity, given by $\dot{\gamma}v_y\delta t$, transforms into the flow velocity. Consequently, the peculiar velocity has a smaller value at the changed position. Similarly, particles with negative v_y that come at y have relatively higher flow velocity, and the x component of the peculiar velocity increases as the particles move to new locations. Thus, the probability distribution for velocity at y after time δt can be written as $P(v_x, v_y)^{after} = P(v_x + \dot{\gamma}v_y\delta t, v_y)^{before}$, where $\dot{\gamma}v_y\delta t$ is added in v_x in the velocity distribution function before streaming to account for the change in x component of the peculiar velocity. This is a consequence of the applied shear in y, as the particles stream to new locations. The average velocity correlation, $\langle v_x v_y\rangle$, changes as

$$\langle v_x v_y\rangle^{after} = \int_{-\infty}^{\infty} dv_x \int_{-\infty}^{\infty} dv_y v_x v_y P(v_x + \dot{\gamma}v_y\delta t, v_y) \tag{2.16}$$

Again, by changing the variables $(v_x + \dot{\gamma}v_y\delta t, v_y)$ to (ξ_x, ξ_y) the equation transforms to

$$\begin{aligned}
\langle v_x v_y\rangle^{after} &= \int_{-\infty}^{\infty}\int_{-\infty}^{\infty} d\xi_x d\xi_y \left(\xi_x - \dot{\gamma}\xi_y\delta t\right)\xi_y P(\xi_x,\xi_y) \\
&= \int_{-\infty}^{\infty}\int_{-\infty}^{\infty} d\xi_x d\xi_y \left[(\xi_x\xi_y) - \dot{\gamma}{\xi_y}^2\delta t\right] P(\xi_x,\xi_y) \\
&= \langle\xi_x\xi_y\rangle - \dot{\gamma}\langle\xi_y^2\rangle\delta t
\end{aligned} \tag{2.17}$$

Using the fact that at $y = 0$, the peculiar velocity (ξ_x, ξ_y) is same as the particle velocity (v_x, v_y), the above equation can be written as

$$\langle v_x v_y\rangle^{after} = \langle v_x v_y\rangle - \dot{\gamma}\langle v_y^2\rangle\delta t, \tag{2.18}$$

which suggests that streaming operation changes $\langle v_x v_y\rangle$ by $-\dot{\gamma}\delta t\langle v_y^2\rangle$ and makes v_x and v_y increasingly anti-correlated.

Furthermore, we need to estimate the effect of collision on the velocity correlation. This

can be done by considering the I^{th} collision cell with n particles. After the collision velocity of each particle gets updated according to Eq.((2.3)). The velocity components of a particle after collision can be written as

$$\begin{aligned} v_{ix}(t+\delta t) &= \cos(\alpha)\xi_{ix} \pm \sin(\alpha)\xi_{iy} + u_x \\ v_{iy}(t+\delta t) &= \mp \sin(\alpha)\xi_{ix} + \cos(\alpha)\xi_{iy} + u_y \end{aligned} \tag{2.19}$$

Velocity correlation after collision, using this equation and averaging over particles in the cell and over different rotation angles (α, and $-\alpha$), is:

$$\langle v_{ix}(t+\delta t)v_{iy}(t+\delta t)\rangle = \langle u_x u_y\rangle + \langle \xi_{ix}\xi_{iy}\rangle \left(\cos^2(\alpha) - \sin^2(\alpha)\right) + \cos(\alpha)\left(\langle \xi_{ix}\rangle u_y + \langle \xi_{iy}\rangle u_x\right), \tag{2.20}$$

where all the terms containing ($\pm$) and ($\mp$) are absent due to averaging over angle. Also, the terms containing $\langle \xi_x\rangle$ and $\langle \xi_y\rangle$ are zero by definition. Thus the above equation simplifies to

$$\langle v_{ix}(t+\delta t)v_{iy}(t+\delta t)\rangle = \langle u_x u_y\rangle + \langle \xi_{ix}\xi_{iy}\rangle \cos(2\alpha). \tag{2.21}$$

The correlation $\langle \xi_{ix}\xi_{iy}\rangle$ can be expressed in terms of particle velocity correlation, $\langle v_{ix}v_{iy}\rangle$, as

$$\begin{aligned} \langle \xi_{ix}\xi_{iy}\rangle =& \langle (v_{ix}-u_x)(v_{iy}-u_y)\rangle \\ =& \langle v_{ix}v_{iy}\rangle - \langle u_y v_{ix}\rangle - \langle u_x v_{iy}\rangle + \langle u_x u_y\rangle \end{aligned} \tag{2.22}$$

The average velocity can be written as $\mathbf{u} = (\mathbf{v}_i + \hat{\mathbf{v}})/n$, where $\hat{\mathbf{v}} = \sum_{k=1,k\neq i}^{n} \mathbf{v}_k$. Furthermore, we assume that molecular chaos is valid, that is, velocities of the different particles are uncorrelated and thus $\langle \hat{v}_x v_{iy}\rangle = 0$, and $\langle \hat{v}_y v_{ix}\rangle = 0$. Thus, under molecular chaos assumption following relations holds:

$$\langle u_y v_{ix}\rangle = \frac{1}{n}\langle v_{ix}v_{iy}\rangle, \quad \langle u_x v_{iy}\rangle = \frac{1}{n}\langle v_{ix}v_{iy}\rangle. \tag{2.23}$$

Similarly, as there is no distinction between the particles, one can write:

$$\langle u_x u_y\rangle = \frac{1}{n}\langle u_x v_{1y}\rangle + \frac{1}{n}\langle u_x v_{2y}\rangle + \cdots = \langle u_x v_{iy}\rangle = \frac{1}{n}\langle v_{ix}v_{iy}\rangle. \tag{2.24}$$

Using the relations in Eq.((2.22)), the correlation $\langle \xi_x \xi_y\rangle$ is

$$\langle \xi_{ix}\xi_{iy}\rangle = \frac{n-1}{n}\langle v_{ix}v_{iy}\rangle. \tag{2.25}$$

Finally, substituting the expressions for $\langle \xi_{ix}\xi_{iy}\rangle$ and $\langle u_x u_y\rangle$ from Eq.((2.25)), ((2.23)) into Eq.((2.21)), the expression for correlation is:

$$\langle v_{ix}(t+\delta t)v_{iy}(t+\delta t)\rangle = \left[1 - \left(\frac{n-1}{n}\right)(1-\cos 2\alpha)\right]\langle v_{ix}(t)v_{iy}(t)\rangle \tag{2.26}$$

For simplicity, we drop the index i since all the particles are identical. If we consider density fluctuation inside the cell to follow Poisson distribution $P(n) = e^{-M}M^n/n!$, the probability of finding a particle together with other $n-1$ particles is $nP(n)/M$. So, taking an average over

all possible configurations, the equation is modified to

$$\sum_{n=1}^{\infty} \frac{nP(n)}{M} \langle v_x(t+\delta t) v_y(t+\delta t) \rangle = \sum_{n=1}^{\infty} \frac{nP(n)}{M} \left[1 - \left(\frac{n-1}{n} \right) (1 - \cos 2\alpha) \right] \langle v_x(t) v_y(t) \rangle \quad (2.27)$$

$$= \left[1 - \left(\frac{M - 1 + e^{-M}}{M} \right) (1 - \cos 2\alpha) \right] \langle v_x(t) v_y(t) \rangle \quad (2.28)$$

$$= f(\alpha, M) \langle v_x(t) v_y(t) \rangle \quad (2.29)$$

Hence we see that the velocity correlation $\langle v_x(t) v_y(t) \rangle$ first decreases due to streaming step and then gets multiplied by a factor $f(\alpha, M)$ after the collision step. Thus, in steady state following self-consistency condition must hold

$$(\langle v_x v_y \rangle - \dot{\gamma} \delta t \langle v_y^2 \rangle) f = \langle v_x v_y \rangle, \quad (2.30)$$

which implies

$$\langle v_x v_y \rangle = -\frac{\dot{\gamma} \delta t f}{1 - f} \langle v_y^2 \rangle. \quad (2.31)$$

Substituting into Eq.((2.15)) gives

$$\sigma_{xy} = \rho \dot{\gamma} \delta t \langle v_y^2 \rangle \left(\frac{1}{2} + \frac{f}{1 - f} \right), \quad (2.32)$$

and we use the equipartition argument, $\langle v_y^2 \rangle = k_B T / m$, to get

$$\eta_{kin}^{2D} = \frac{\rho k_B T \delta t}{2m} \left[\frac{2M}{(M - 1 + e^{-M})(1 - \cos 2\alpha)} - 1 \right]. \quad (2.33)$$

A similar procedure can be followed in 3D to get the following expression for kinetic viscosity (Pooley & Yeomans 2005):

$$\eta_{kin}^{3D} = \frac{\rho k_B T \delta t}{2m} \left[\frac{5M}{(M - 1 + e^{-M})(2 - \cos(\alpha) - \cos 2\alpha)} - 1 \right]. \quad (2.34)$$

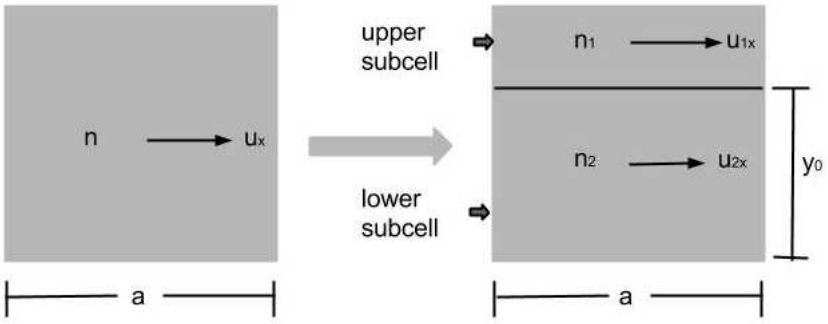

Figure 2.4: *Schematic diagram for partitioning the collision cell to calculate momentum exchange between the two subcells due to collision.*

Collisional Viscosity

Finally, we need to estimate the so called "collisional viscosity"which emerges due to non-local nature of momentum exchange during the collisions. To compute this contribution, as shown in Figure (2.4), I^{th} collision cell with n particles is considered. A horizontal plane at a distance y_0 from the bottom of the cell, which divides the cell into two subcells with upper subcell containing n_1 particles with average velocity u_{1x} and lower subcell containing n_2 particles with average velocity u_{2x} is considered. The average velocity in the cell is $u^I = (n_1u_{1x} + n_2u_2)/(n_1 + n_2)$. The goal is to calculate the momentum exchange across the plane during the collision step. If the cell size a is small enough, the average quantities do not change substantially over distances comparable to a. Thus, the shear rate in the cell is:

$$\dot{\gamma} = \frac{\partial u_x}{\partial y} = \frac{u_{1x} - u_{2x}}{\delta y} \tag{2.35}$$

where $\delta y = a/2$ is the distance between the centers of the two collision cells. Using the expression for $u_{1x} - u_{2x}$ in the above equation for shear stress, we get

$$\dot{\gamma} = \frac{u_{1x} - u_{2x}}{\delta y} = \frac{2n}{a(n - n_1)}(u_{1x} - u_x^I) \tag{2.36}$$

where we have used the fact that $n = n_1 + n_2$ and also $u_{1x} - u_x^I = n_2(u_{1x} - u_{2x})/(n_1 + n_2)$.

To calculate contribution to shear stress, σ_{xy}, at plane y_0, the momentum change in the upper subcell resulting from the collision needs to be estimated, as there is a net transfer of x-momentum across y_0 because of the collision. Thus, the shear stress is given by

$$\sigma_{xy} = -\frac{m}{a^{D-1}\delta t}\left[\sum_{i=1}^{n_1}(v_{ix}(t + \delta t) - v_{ix}(t))\right] \tag{2.37}$$

where a^{D-1} is the area of the plane y_0 across which momentum transfer takes place. Using Eq.((2.19)) to substitute for $v_{ix}(t + \delta t) - v_{ix}(t)$ in the above equation, we get

$$\begin{aligned}\sigma_{xy} &= -\frac{m}{a^{D-1}\delta t}\left[\sum_{i=1}^{n_1}\{(\cos\alpha - 1)(v_{ix} - u_x^I) \pm v_{iy}\sin\alpha\}\right], \\ &= -\frac{m}{a^{D-1}\delta t}\left[n_1(\cos\alpha - 1)(u_{1x} - u_x^I) \pm \sin\alpha\sum_{i=1}^{n_1} v_{iy}\right].\end{aligned} \tag{2.38}$$

Next, averaging over the isotropic distribution of the rotation axis, the second term in the numerator drops off, and the equation simplifies to

$$\sigma_{xy} = \frac{m}{a^{D-1}\delta t}\left[\frac{2}{D}n_1(1 - \cos\alpha)(u_{1x} - u_x^I)\right], \tag{2.39}$$

Substituting for $(u_{1x} - u_x)$ from Eq.((2.36)) and using the definition of viscosity, we get

$$\eta_{col} = \frac{mn_1(n - n_1)}{a^{D-2}dn\delta t}(1 - \cos\alpha) \tag{2.40}$$

We assume that the probability of finding a particle in a subcell is proportional to the subcell area. This implies that the number of particles in the upper subcell, n_1, follows binomial distribution with $p = (1 - y_0/a)$, and $q = y_0/a$. When we take the average over all possible n_1, the equation reduces to

$$\eta_{col} = \frac{m(1-\cos\alpha)}{a^{D-2}D\delta t}(n-1)\frac{y_0}{a}\left(1-\frac{y_0}{a}\right). \tag{2.41}$$

In the above equation, we have used the fact that for a binomially distributed random variable, n_1, $\langle n_1\rangle = np$ and $\langle n_1^2\rangle = npq + n^2p^2$, where n is the total number of particles in the I^{th} cell, and corresponds to the maximum number of particles that the subcell can accommodate. Furthermore, considering the fluctuations in the number of particles (n) inside the cell to follow Poisson distribution, and averaging over all possible particle configurations, the equation becomes

$$\eta_{col} = \frac{m(1-\cos\alpha)}{a^{D-2}D\delta t}(M-1+e^{-M})\frac{y_0}{a}\left(1-\frac{y_0}{a}\right) \tag{2.42}$$

Finally, averaging for $0 < y_0 < a$, we obtain the final expression for the collisional viscosity as

$$\eta_{col} = \frac{m(1-\cos\alpha)}{6\,a^{D-2}D\delta t}(M-1+e^{-M}) \tag{2.43}$$

In 2D and 3D, collisional contributions are thus given by

$$\eta_{col}^{2D} = \frac{m(1-\cos\alpha)}{12\,\delta t}(M-1+e^{-M}), \quad \eta_{col}^{3D} = \frac{m(1-\cos\alpha)}{18\,a\delta t}(M-1+e^{-M}). \tag{2.44}$$

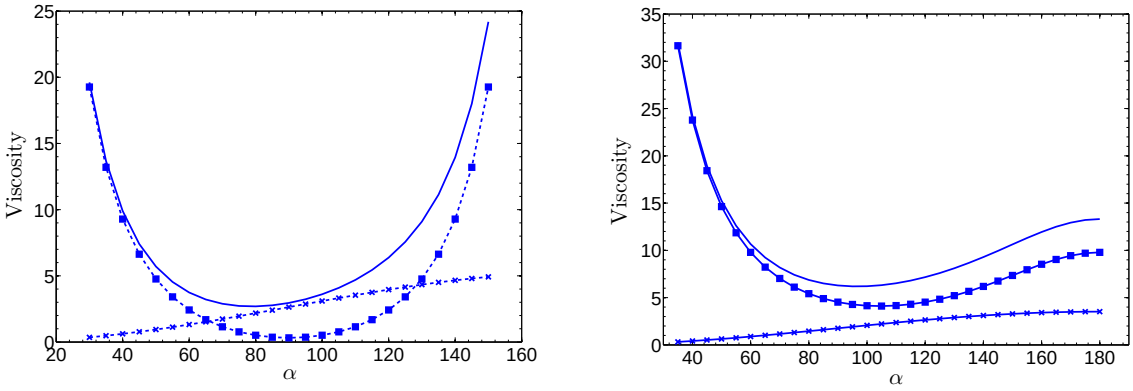

(a) 2D (b) 3D

Figure 2.5: *Plot of viscosity with α; η is shown by the solid line, η^{kin} in broken line with filled squares, and η^{col} broken line with cross. For these two plots $M = 20$, $a = 1.0$, $k_BT/m = 1.0$, $\delta t = 0.6$*

As we mentioned before, the total viscosity of MPCD fluid is a sum of kinetic and collisional viscosities (Fig.(2.5)). In 2D following Eq.((2.33)) and ((2.43)), it can be expressed as

$$\eta^{2D} = \frac{\rho k_B T\delta t}{2m}\left[\frac{2M}{(M-1+e^{-M})(1-\cos 2\alpha)} - 1\right] + \frac{m(1-\cos\alpha)}{12\delta t}(M-1+e^{-M}). \tag{2.45}$$

Similarly in 3D, we arrive at the following expression for viscosity (Eq.((2.34)) and ((2.43)))

$$\eta^{3D} = \frac{\rho k_B T \delta t}{2m}\left[\frac{5M}{(M-1+e^{-M})(2-\cos\alpha-\cos 2\alpha)} - 1\right] + \frac{m(1-\cos\alpha)}{18a\delta t}(M-1+e^{-M}), \quad (2.46)$$

where the first term on the right hand side corresponds to the kinetic contribution to the viscosity, and the second term that of the collisional contribution.

2.4 Galilean Invariance and Grid Shift

MPCD systems at low temperatures and small time steps ($\delta t < 0.4$) show anomalous behaviour when a fixed grid is used (Ihle & Kroll 2001). The reason is that, under such conditions same particles in a cell undergo collisions over multiple time steps. As a result, velocity correlations start building up, i.e. particles retain memory of their previous collisions. This results breaking of Galilean invariance and the system shows unphysical behaviour such as flow dependent transport properties.

Ihle and Kroll (Ihle & Kroll 2001) have shown that it is possible to restore Galilean invariance by shifting the particle, or alternatively by placing the grid randomly by a constant vector before each collision. The different components of the shift vector is drawn from an uniform distribution in $[-a/2, a/2]$. The grid-shift (or particle-shift) ensures that at each time step, different particles participate in a collision, and so, the problem of velocity correlation is remedied. Due to grid-shift, the average jump in moment is enhanced, which in turn leads to increase in the viscosity of the system. This additional correction to the viscosity should be accounted for in simulations using grid shift (Kikuchi *et al.* 2003).

2.5 Ghost Particles or Wall Particles

When the domain boundaries are complicated, often partially filled collision cells are encountered. With grid-shift partially filled cells are quite common and can not be avoided. If the partially filled cells result from wall boundaries, different fluid behaviour, compared to bulk, can be observed in the vicinity of the wall. In order to overcome this problem, use of ghost particles or wall particles have been suggested (Lamura *et al.* 2001; Bolintineanu *et al.* 2012), and are used for calculating the cell velocity during collision step. These particles have average velocity same as the wall, and fluctuating part of the velocity is drawn from the Maxwell-Boltzmann distribution at the wall temperature. The cell velocity is thus computed as

$$\mathbf{u}^I = \frac{\sum_{i=1}^{\tilde{M}} \mathbf{v}_i^I + \mathbf{g}}{M}, \quad (2.47)$$

where $\mathbf{g}$ is velocity contributions from the wall particles. Since sum of Gaussian random numbers is also a Gaussian, only one velocity vector is needed with velocity components drawn from the Maxwell-Boltzmann distribution with mean U_w and variance $((\tilde{M}-M)k_BT/m)$; $\tilde{M}$ is the number of particles in the partially filled cell and U_w is the wall velocity.

2.6 Few Practical Issues

In this section, specifics of setting the simulation parameter setting, and sampling macroscopic quantities are presented briefly. In addition to temperature and density of the system, transport properties of an MPCD fluid also depend upon parameters such as, time step (δt), average number of particles per collision cell (M), and angle of rotation (α). For different flow problems we need to set appropriate non-dimensional numbers, e.g. Schmidt number (ν/D), Reynolds number (lv/ν), Peclet number ($\nu l/D$), where $\nu = \eta/\rho$ is the kinematic viscosity, D is the diffusion coefficient, and v and l are the characteristic velocity and length scale in the problem, respectively. For example, a fluid modeled using MPCD, the Schmidt number can be increased by lowering δt, and the fluid behaviour can thus be changed to that of a gas or a liquid (Ripoll *et al.* 2005) by adjusting δt. The MPCD parameters should be set such that, the required non-dimensional number is set appropriately for the problem.

Finally, it should be noted that fluctuations are inherent in MPCD algorithm, and to get a smoother values of these observable quantities, further averaging might be required. We often take ensemble averaging, especially for a transient simulation, from a large number of independent runs with same initial conditions. However, for steady state calculations, time averaging can be used once the initial transience has passed. Similarly, in a flow simulation with periodic boundary condition, physical properties do not change in the direction of periodicity and thus, slab wise averaging is done to reduce the fluctuations in macroscopic quantities.

Chapter 3

Microflows with Standard MPCD

3.1 Introduction

A quantitative understanding of the effectiveness of MPCD algorithm is required for its application to the hydrodynamic problems. Furthermore, as the method has molecular background and a well defined notion of mean-free path, one would like to know the domain of validity of the method in terms of Knudsen number. In this regard, gaseous microflows provide an ideal benchmark condition, as well as possible new applications for the method. Such flows are typically observed in devices where characteristic length scales are in micro-meters (in the range of 1-100 microns)(Ho & Tai 1998). As the operating pressures are atmospheric, the mean free path of the fluid ($\sim 68nm$ at room temperature) is comparable to the geometry, i.e the flows are finite Knudsen flows and, in particular, in the slip flow regime (Karniadakis *et al.* 2002).

In this regime, one expects to observe departure from the continuum hydrodynamics described by Navier-Stokes-Fourier equations, and a good amount of understanding already exists for this departure. In Fig.(3.1) range of applicability for various methods, used to study finite Knudsen flows, are shown. Traditionally, three distinct approaches were used, with varying degree of success. In the first approach, Navier-Stokes-Fourier description was used with slip boundary condition. It was argued that the dominant effect for finite but small Knudsen flows is the appearance of slip at the wall (Beskok & Karniadakis 1994, 1999; Arkilic *et al.* 1997). In the second approach, simplified collision description, e.g. Boltzmann-BGK approximation, was used to get semi-analytical results in simple geometries such as channel flows (Cercignani 1975). The third route was numerical solutions using Direct Simulation Monte-Carlo (DSMC) method, which is accurate as well as general enough for most of the applications in the microflow regime (Piekos & Breuer 1996; Oran *et al.* 1998). However, this route is computationally very demanding due to inefficiency of DSMC for sub-sonic flows (which is often the case in microflows) (Oran *et al.* 1998).

Due to increased importance of gaseous microflows in engineering applications (e.g. Micro-Electro-Mechanical Systems (MEMS)), and lack of accurate and fast simulation tools, in the last decade various new methodologies were developed for modeling gaseous microflows. Mesoscale simulations tools such as LBM, DPD and MPCD due to their good computational efficiency, are potentially quite attractive for modeling them. The vast amount of available data for canonical flows (e.g. shear flow, Poiseuille flow) using Boltzmann-BGK model, or slip flow models make this regime an ideal case for checking the domain of validity of a given mesoscale method. These set-ups have already been used to establish the kinetic nature of the mesoscale algorithms such

as DPD and LBM (Czerwinska & Adams 2003; Nie *et al.* 2002; Lim *et al.* 2002; Ansumali *et al.* 2006). In this chapter, the effectiveness of MPCD algorithm for simulating gaseous flows in the slip-flow regime is investigated. In this regard, as test cases, the set-up of shear driven flows, gravity driven flows, and pressure driven flows at finite Knudsen numbers are chosen.

The chapter is organized as follows: In section 3.2, a brief description of gaseous microflows is presented and different tools for predicting flow properties are described. In section 3.3, two different wall boundary conditions (bounce back and diffuse wall) are discussed, and preference for diffuse wall boundary for simulating microflows is explained. Applicability of MPCD for different Knudsen range is investigated in section 3.4. In section 3.5, different flow set-ups are described and relevant results are presented. Finally, few conclusions are drawn in section 3.7 based on our findings.

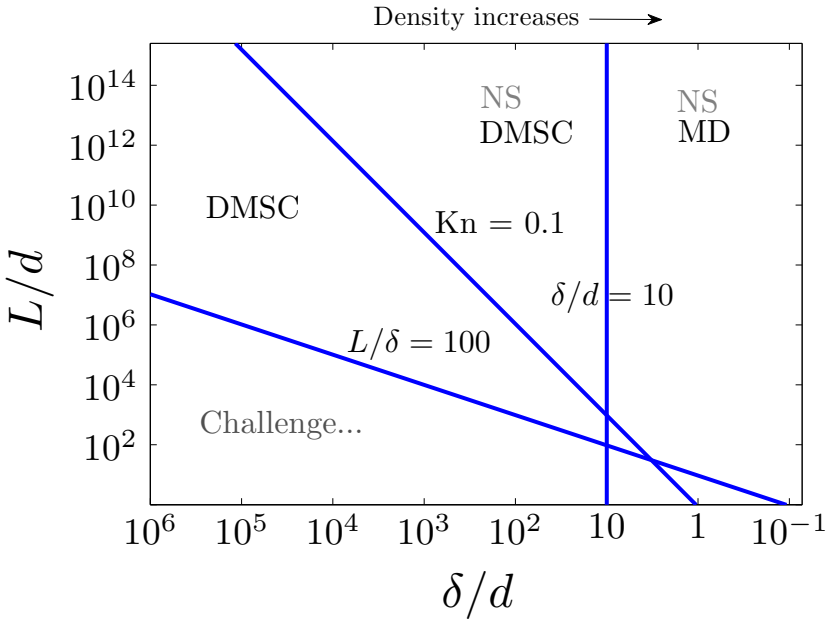

Figure 3.1: *A rough sketch showing computational feasibility of different methods in different regimes (Oran* et al. *1998). Here, L is a characteristic length scale, d is the molecular diameter, and δ is the average spacing between two molecules.*

3.2 Gaseous Microflow

The continuum model of fluid dynamics for gases, as described by Navier-Stokes-Fourier (NSF) description, assumes that macroscopic length scales are much larger than mean free path. In this description, stress tensor and heat flux do not have independent dynamics and are known in terms of constitutive relation of Stokes and Fourier. The validity of hydrodynamics is quantified in terms of the Knudsen number (Kn), which is defined as a ratio of the mean free path to a characteristic length scale of the system (e.g. channel width). It is widely accepted that the Navier-Stokes-Fourier description with no-slip boundary condition is valid for $\mathrm{Kn} < 0.001$, and the first departure from this description is in terms of the failure of no slip boundary condition. As Knudsen number is increased, constitutive relations break down and one notices non-Newtonian behaviours (Ansumali *et al.* 2007). Gaseous flows through a microdevice are

often in the intermediate regime of slip flow ($0.001 \leq \mathrm{Kn} \leq 0.1$). It can be safely said that the flow is weakly rarefied in this regime.

The flow is usually highly sub-sonic such that Mach number of the flow, $\mathrm{Ma} \ll 0.3$. Though the continuum flow in this range of Mach number is considered incompressible, it is often argued that mild compressible behavior does show up in the slip-flow regime (Beskok *et al.* 1996; Arkilic *et al.* 1997). For example, it has been found experimentally that centre line pressure in microchannels, in which flow is driven by maintaining a pressure difference at the inlet and at the outlet, is non-linear (Pong *et al.* 1994). For numerical simulations, such low Mach numbers imply that the fluctuations in hydrodynamic quantities can make resolution requirements on particle methods such as DSMC, MPCD etc. quite stringent (Oran *et al.* 1998). Another interesting aspect of microflow, that is generally noticed, is relatively high viscous heating due to low Reynolds number (Re). Thus, in realistic applications such as gas flow in electronic devices, where the fluid medium has bad conductivity, temperature variations can not be ignored.

As discussed earlier, in the continuum modeling of gaseous microflow, it is assumed that the bulk hydrodynamics remains same as the Navier-Stokes-Fourier description, but the slip boundary conditions are used to model the boundary effects. Though, first order velocity slip model works quite well for shear flow or pressure driven flow simulations, second order correction is required for simulating gravity driven flows. Hadjiconstantinou (see Hadjiconstantinou (2003)) has suggested a modified form of Cercignani's second order velocity-slip model, in which first and second order coefficients are adjust to suit a hard sphere gas. It is generally accepted that a hard sphere gas is a reasonable approximation to a real gas in an isothermal flow; the hard sphere model is often used in particle based algorithms, such as DSMC, for simulating gases. In literature, following form is suggested for the second order velocity-slip model:

$$u|_{wall} = \delta_1 \lambda \frac{\partial u}{\partial y}\Big|_{wall} - \delta_2 \lambda^2 \frac{\partial^2 u}{\partial y^2}\Big|_{wall}, \tag{3.1}$$

the positive y direction is taken perpendicular to the wall pointing into the flow, and slip coefficient δ_1 and δ_2 are typically obtained by asymptotic theories using microscopic Boltzmann-BGK description. This slip flow model shows a good agreement for the velocity profile when compared with the DSMC simulations of hard spheres molecules.

An alternate, more microscopic approach, as already indicated, is to use DSMC (Oran *et al.* 1998). In this algorithm, the motion is decoupled into two distinct steps of collision and advection. This decoupling of streaming and collision imposes that the streaming time step is smaller than the mean collision time. During streaming, particles do not interact and move ballistically over time step δt. In the collision step, binary collisions are performed in a small volume (collision cell) between particles chosen randomly. The collision step is an stochastic procedure which tries to capture the overall scattering effects between colliding molecules, where any two particles inside a collision cell is allowed to collide. Thus, cell size in the method should be smaller than the mean free path. Similarly, every cell must have a minimum number of particles to avoid large fluctuations. Empirical studies suggest that cell size should be approximately one third of the mean-free path, and number of particles in each collision cell should be greater than 20. A brief introduction about this method can be found in (Alexander & Garcia 1997), and a detailed description can be found in the monogram (Bird 1994). Theoretically, DSMC

can be used for simulating flows at all Knudsen numbers but limitations on the computational resources restricts its uses to high Knudsen, high Mach applications. It is an accepted view that in the regime of microflows, the method is not very efficient due to large statistical fluctuations (in microflows, the difference between the flow velocity ($1 - 10$ cm/s) and the molecular speed (330 m/s) may differ by orders of magnitude) as well as due to the need of long time simulations (Oran *et al.* 1998). Here, it should be reminded that the time step in DSMC is of the order of mean free time (10^{-9}s), but the flow properties in microchannels are required at a much larger time scales (~ 1 sec).

Recently, Ansumali and Karlin using shear flow set-up showed that hierarchy of LBM kinetic equations with diffuse wall boundary condition form a closed system which can be solved exactly in 1D to predict flow properties such as velocity profile, shear stress in a microflow (Ansumali *et al.* 2007). Furthermore, they showed that by including more terms in the hierarchy, higher order effects can be resolved. For example, by including forth-order terms development of Knudsen layer in the velocity profile can be captured. Later, Yudistiawan et al. solved LBM hierarchy with gravity, and by including forth and sixth order terms in the hierarchy, captured Knudsen layer effects in the velocity profile (Yudistiawan *et al.* 2008, 2010). Success of LBM in formulating a consistent closed system with diffuse wall boundary condition also suggests a possible remedy to the consistency problems in solving Boltzmann equation via expansion of distribution function in Hermite polynomials. Note that hierarchy of equations obtained by this method, with diffuse wall boundary condition, remain inconsistent. Solving Boltzmann hierarchy is expected to result in more accurate solutions compared to LBM kinetic equations.

3.3 Wall Boundary Conditions for MPCD

Appropriate treatment of wall boundaries is important for internal flows in microdevices. It is well known that for flows at finite Knudsen numbers, velocity slip and temperature jump can be observed at the wall. In MPCD, one of the most widely used boundary condition is bounce back (Lamura *et al.* 2001; Whitmer & Luijten 2010; De Angelis *et al.* 2012). However a few authors have also used diffusive wall boundary condition (Padding *et al.* 2005; Padding & Louis 2006). In this section, both of these boundary conditions is reviewed.

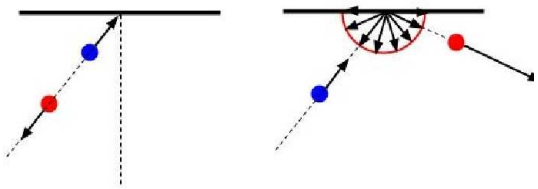

Figure 3.2: *Wall boundary conditions. (a) Bounce Back (b) Diffuse Wall.*

3.3.1 Bounce Back

In mesoscale methods such as MPC and LBM, bounce back condition is often used for modeling no slip boundary condition (for LBM see Succi (2001); Chen *et al.* (1996), and for MPCD see Bolintineanu *et al.* (2012)). In this boundary condition the velocity of the particle is reversed after it interacts with the wall, i.e. the particle traces back the same path it followed to approach the wall (see Fig.(3.2a)). Thus, velocity components parallel, $v'_{||}$, and perpendicular, $v'_{\perp}$, to the wall are changed to

$$v_{||} = -v'_{||}, \quad v_{\perp} = -v'_{\perp}, \tag{3.2}$$

just after the wall interaction. It is clear that with bounce back, the energy of the particle, before and after the wall interaction, remains unchanged. This suggests that the wall acts like an adiabatic boundary for the fluid. It is also apparent that the bounce back boundary condition can not be used for simulating flows in which energy is supplied to the system by an external force. In such cases, the thermal energy of the system will keep increasing leading to a blow up scenario. In order to keep the energy bounded thermostating is used which sets the temperature of the system to a given value (Gompper *et al.* 2008). Thus, this boundary condition is applied for the problems where temperature variations are not important, i.e. for isothermal flows.

3.3.2 Diffuse Wall

An alternative methodology, for modeling walls in simulations, is diffuse wall approximation. In implementing diffuse wall boundary condition, it is assumed that the particles get adsorbed into the wall and undergoes multiple collisions before re-emerging into the fluid (Fig.(3.2b)). Because of multiple collisions with the wall, particles forget everything about the velocity before wall interaction and get equilibrated to the wall temperature (T_w). Furthermore, physically fast moving particles interact more frequently than the slower moving particles, and the diffuse boundary condition tries to capture this phenomena by using biased Maxwellian distribution for generating the velocity components of the re-emitted particles (Alexander & Garcia 1997). The velocity component normal to the wall is generated using following distribution:

$$P_{\perp}(v_{\perp}) = \frac{m}{k_{\mathrm{B}}T_w} v_{\perp} e^{-mv_{\perp}^2/2k_{\mathrm{B}}T_w}, \tag{3.3}$$

and each parallel velocity component is generated using

$$P_{\parallel}(v_{\parallel}) = \sqrt{\frac{m}{2\pi k_{\mathrm{B}}T_w}} e^{-mv_{\parallel}^2/2k_{\mathrm{B}}T_w}, \tag{3.4}$$

where m is the mass of the particle and k_{B} is the universal Boltzmann constant.

Since the particles get equilibrated to wall temperature, the wall behaves like an isothermal boundary. Furthermore, no thermostats are required with this wall boundary condition as the wall itself acts like a heat bath. This method is regularly used in the context of gaseous microflows with DSMC (Alexander & Garcia 1997) and LBM (Ansumali & Karlin 2002) to produce velocity slip and temperature jump at the wall. Moreover, the slips have been shown

to be consistent with the known results from Botzmann-BGK equation (Ansumali *et al.* 2007; Yudistiawan *et al.* 2008, 2010). It is known that this boundary condition leads to slip flow in MPCD simulations (Bolintineanu *et al.* 2012). However, consistency of such slip with kinetic theory has not been investigated so far. In this chapter, the slip observed in MPCD with diffusive boundary condition will be contrasted with the slip flow models and other known results from kinetic theory.

3.4 Kndsen Number for MPCD Fluid

Though molecular collisions are modeled in the MPCD algorithm, there are no explicit molecular parameters involved. In this method, one relates the rotation angle and time step with the transport coefficients such as viscosity. Thus, one needs to consistently define Knudsen number so that the method can be contrasted with the results known from kinetic theory. In this thesis, viscosity based definition of the mean free path is used. In Ref. Hadjiconstantinou (2003), following form is suggested for the viscosity:

$$\lambda = \frac{\eta}{p}\sqrt{\frac{\pi RT}{2}}, \tag{3.5}$$

where η is the dynamic viscosity, p and T are the pressure and temperature, respectively, and $R = k_{\mathrm{B}}/m$ is the gas constant of the fluid. In this definition, by substituting the viscosity of the MPCD fluid (Chapter 2, section 3), we get

$$\eta = \frac{\rho k_{\mathrm{B}} T \delta t}{2m}\left\{\frac{5M}{(M-1+e^{-M})(2-\cos\alpha-\cos 2\alpha)} - 1\right\} + \frac{\rho a^2}{\delta t}\left\{\frac{M-1+e^{-M}}{6DM}(1-\cos\alpha)\right\}, \tag{3.6}$$

where D is the dimensionality of the problem. The expression for Kn is:

$$\mathrm{Kn} = \frac{\mathrm{a}}{\mathrm{L}}\sqrt{\frac{\pi}{2}}\left[\frac{\tau}{2}\left\{\frac{5\mathrm{M}}{(\mathrm{M}-1+\mathrm{e}^{-\mathrm{M}})(2-\cos\alpha-\cos 2\alpha)} - 1\right\} + \frac{1}{\tau}\left\{\frac{\mathrm{M}-1+\mathrm{e}^{-\mathrm{M}}}{6\mathrm{DM}}(1-\cos\alpha)\right\}\right], \tag{3.7}$$

where $p = \rho k_{\mathrm{B}} T/m$ is used to simplify the equation and time factor τ is defined as

$$\tau = \frac{\delta t\sqrt{\frac{k_{\mathrm{B}}T}{m}}}{a}, \tag{3.8}$$

and it is related to δt such that a particle moving with velocity $\sqrt{k_{\mathrm{B}}T/m}$ travels a distance τa. In practice, the factor τ is an $O(1)$ quantity. This happens due to the fact that $\tau \ll 1$ tends to build correlations among the particles which leads to the break down of Galilean invariance, and $\tau > 1.0$ shows unphysical flow behavior near the wall.

Eq.(3.7) suggests that the Knudsen number is a function of the following parameters: the average number of particles per collision cell (M), lattice size (a), time factor (τ), rotation angle (α), and the characteristic length L. It is clear that Kn dependence on M is extremely weak and can be ignored. Furthermore, for a given density of the fluid corresponding variation in a is very slow. Later, it would be shown that for $\alpha < 45^0$ numerically yielded value of the viscosity departs significantly from the theoretical value, and the observed departure depends

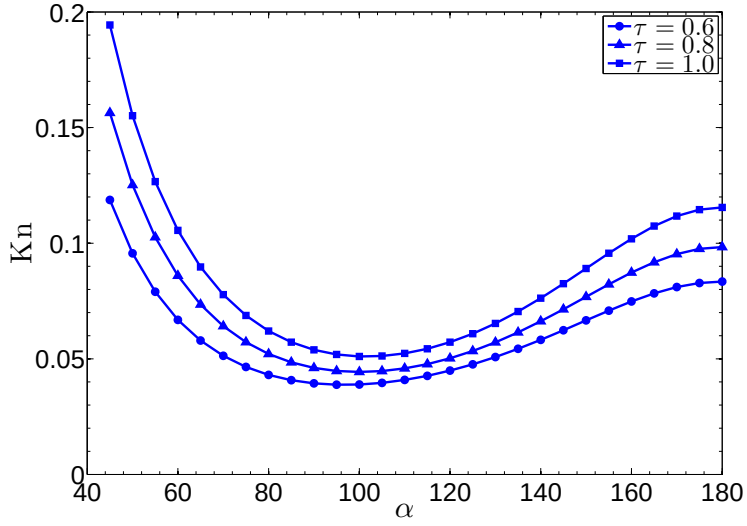

Figure 3.3: *Plot of* Kn *with* α *for MPCD (Eq.(3.7)) at different values of* τ*;* $a/L = 0.1$*,* $M = 20$*.*

strongly on the Knudsen number of the flow. Also note that for $\alpha > 45^0$, only a small variation in the viscosity can be observed. Thus, only free parameter remaining is L. Our experience with MPCD shows that for various values of these parameters, only flows with $\mathrm{Kn} \lesssim 0.1$ can be simulated (see Fig.(3.3)). It is worth mentioning here that in this range, DSMC is very expensive, and an alternative simulation tool is required (Oran *et al.* 1998).

3.5 Canonical Flow Arrangements

In this thesis, attention is restricted to 2D unidirectional flows only. In particular, we consider flows between two infinitely large parallel plates (Fig.(3.4)) located at $y = 0$ and $y = L$, where L is the separation between the two plates. It is also assumed that the flow is in steady state with flow velocity in x-direction, and the flow quantities (e.g. velocity, and temperature) vary only in y.

Here, we have considered canonical flow arrangements such as shear driven, gravity driven, or pressure driven flows. In shear flow, the flow is driven by the motion of the confining walls through momentum diffusion; in gravity driven the flow results due to the action of a constant force (e.g. gravity) on the fluid particles; and in pressure driven, which is most common in the microfluidic devices, the flow is driven by maintaining a pressure gradient along the length of the channel. Though, gravity and pressure driven flows appear similar on the macro scales, the microscopic details are quite different (Zheng *et al.* 2002).

Navier-Stokes equations can be solved, for the canonical flow arrangements described here, using the second order velocity-slip boundary condition. The resulting velocity profile is

$$u_x(y) = \frac{L^2}{2\eta}\left(\rho F_x - \frac{\partial p}{\partial x}\right)\left[-\frac{y}{L}\left(\frac{y}{L} - \frac{1}{2}\right) + \delta_1 \mathrm{Kn} + 2\delta_2 \mathrm{Kn}^2\right] + \frac{(U_2 - U_1)}{(2\mathrm{Kn}\delta_1 + 1)}\left(\frac{y}{L} - \frac{1}{2}\right) + \frac{(U_1 + U_2)}{2}, \tag{3.9}$$

where F_x is the constant force (per unit mass), $\partial p/\partial x$ is the pressure gradient at a given x,

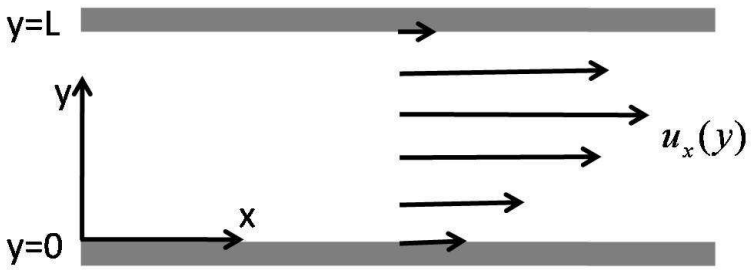

Figure 3.4: *Schematic depicting the flow arrangement.*

and U_1 and U_2 are the lower and upper wall velocities, respectively. The cross-stream velocity profile corresponding to the gravity and pressure driven cases is shown in Fig.(3.5b), and for shear driven flow the same is shown in Fig.(3.5a). It is evident that the velocity profile is parabolic for the gravity and pressure driven flows, while it is linear for the shear flow. The velocity slip at the walls is also apparent.

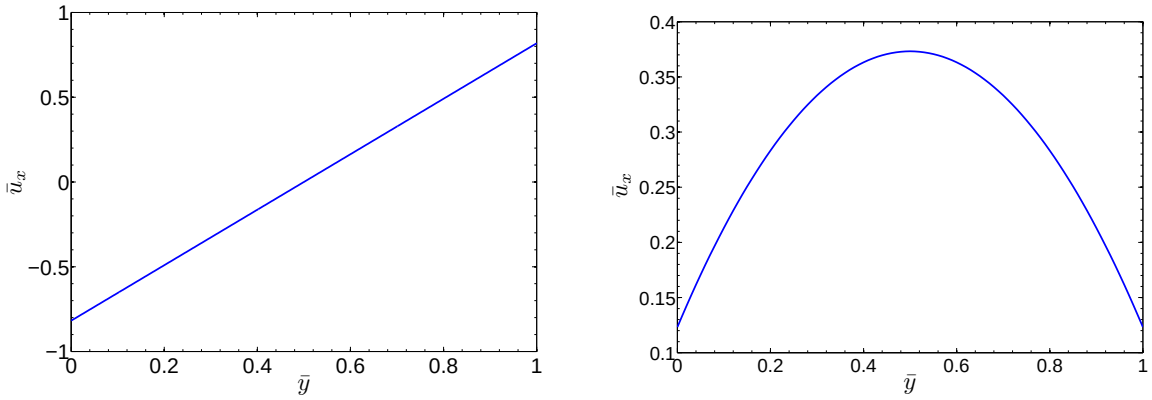

(a) (b)

Figure 3.5: *Cross-stream velocity profiles. In these figures u_x is scaled with U, which is chosen appropriately for different flow scenarios, and y with L. (a) Gravity or pressure driven flows. $U = \frac{L^2}{2\eta}\rho F_x$ for gravity flow, while for pressure driven flow $U = -\frac{L^2}{2\eta}\frac{\partial p}{\partial x}$ (b) Shear driven flows. We have chosen $U_2 = -U_1 = U_w$, and $U = U_w$.*

3.6 Numerical Simulations

In all the simulations, the mass of each particle, $m = 1$, the particle diameter, $\sigma = 1$, and the energy was measured in the units of $k_{\mathrm{B}}T/m$. We have also set $T = 1$ and $k_{\mathrm{B}} = 1$, except in pressure driven flow scenario in which $k_{\mathrm{B}} = 0.5$. The density of the gas, $\rho = 1.21 \times 10^{-03}$, and the time factor, τ, was set to 0.6 such that we were working in the gas flow regime (Ripoll *et al.* 2005). The average number of particles per collision cell (M) in simulations was fixed to 20. The cell size (a) obtained form this number and the density is 25.4731. In simulations flow Knudsen number was changed by changing the separation (L) between the two walls.

We have also compared the MPCD data with that of DMSC for a hard sphere gas (the code was developed following Alexander & Garcia (1997)). The same set of parameters, as MPCD

simulations, were considered for DSMC. Based on the chosen density and temperature the mean free path, $\lambda \approx 182.04$ (Eq.(3.5)), for the gas in DSMC simulations, where viscosity is estimated using $\eta = 5m\pi^{1/2}(RT)^{1/2}/(16\sigma)$ (Lifshitz & Pitaevskii 1981). Furthermore, time step used for streaming was roughly $0.1 \times \tau_c$, where $\tau_c = \lambda/\sqrt{k_B T/m}$ is a measure of mean free time. In this section, the velocity profiles obtained form different simulations ($\mathrm{Kn} \in (0.05, 0.001)$) are contrasted with the exact solution (Eq.(3.9)) and the data obtained from DSMC simulations. In order to make the comparison possible, the observed quantities are non-dimensionalized appropriately (u_x with U, and y with L).

In case of shear flow simulations, we have assumed that the bottom plate velocity, $U_1 = -U_w$, and the top plate velocity, $U_2 = U_w$, where $U_w = 0.2$. The characteristic velocity, $U = U_w$. In this case, using Eq.(3.9) the expression for the velocity is:

$$u_x(y) = \frac{2U_w}{2\delta_1 \mathrm{Kn} + 1}\left(\frac{y}{L} - \frac{1}{2}\right). \tag{3.10}$$

Here, it should be noted that the second order slip coefficient (δ_2) does not appear in the velocity expression, which suggests that first order slip model is adequate for predicting the velocity profile in shear flows. Fig.(3.6) shows that in the slip flow regime, velocity profiles obtained from MPCD are in good agreement with the profiles obtained from second order velocity-slip as well as DSMC simulations.

As the second set-up, gravity driven flow was considered. In this case, using Eq.((3.9)), the expression for the velocity is:

$$u_x(y) = \frac{\rho F_x L^2}{2\eta}\left[\frac{y}{L}\left(\frac{y}{L} - 1\right) + \delta_1 \mathrm{Kn} + 2\delta_2 \mathrm{Kn}^2\right]. \tag{3.11}$$

It is evident from the above equation that the velocity slip at the walls ($y = 0$, and $y = L$) is not zero, and the corresponding value of the velocity slip is:

$$u_{slip} = \frac{\rho F_x L^2}{2\eta}\left(\delta_1 \mathrm{Kn} + 2\delta_2 \mathrm{Kn}^2\right). \tag{3.12}$$

This set-up also provides a convenient means for measuring the viscosity of the fluid (Allahyarov & Gompper 2002), which can be written using Eq.((3.11)) as

$$\eta = \frac{\rho F_x L^2}{8(u_{max} - u_{slip})}. \tag{3.13}$$

where the maximum velocity at the center line is:

$$u_{max} = \frac{\rho F_x L^2}{2\eta}\left(\frac{1}{4} + \delta_1 \mathrm{Kn} + 2\delta_2 \mathrm{Kn}^2\right). \tag{3.14}$$

This expression (Eq.(3.13)) is used to calculate the viscosity of an MPCD fluid as a function of rotation angle (α), using both bounce back and diffuse wall boundary conditions. As discussed earlier, bounce back simulations are stable only when system is coupled with a thermostat. As a thermostat, a simplified procedure of rescaling the components of peculiar velocity of each particle corresponding to the system temperature is used (Bolintineanu *et al.* 2012). This

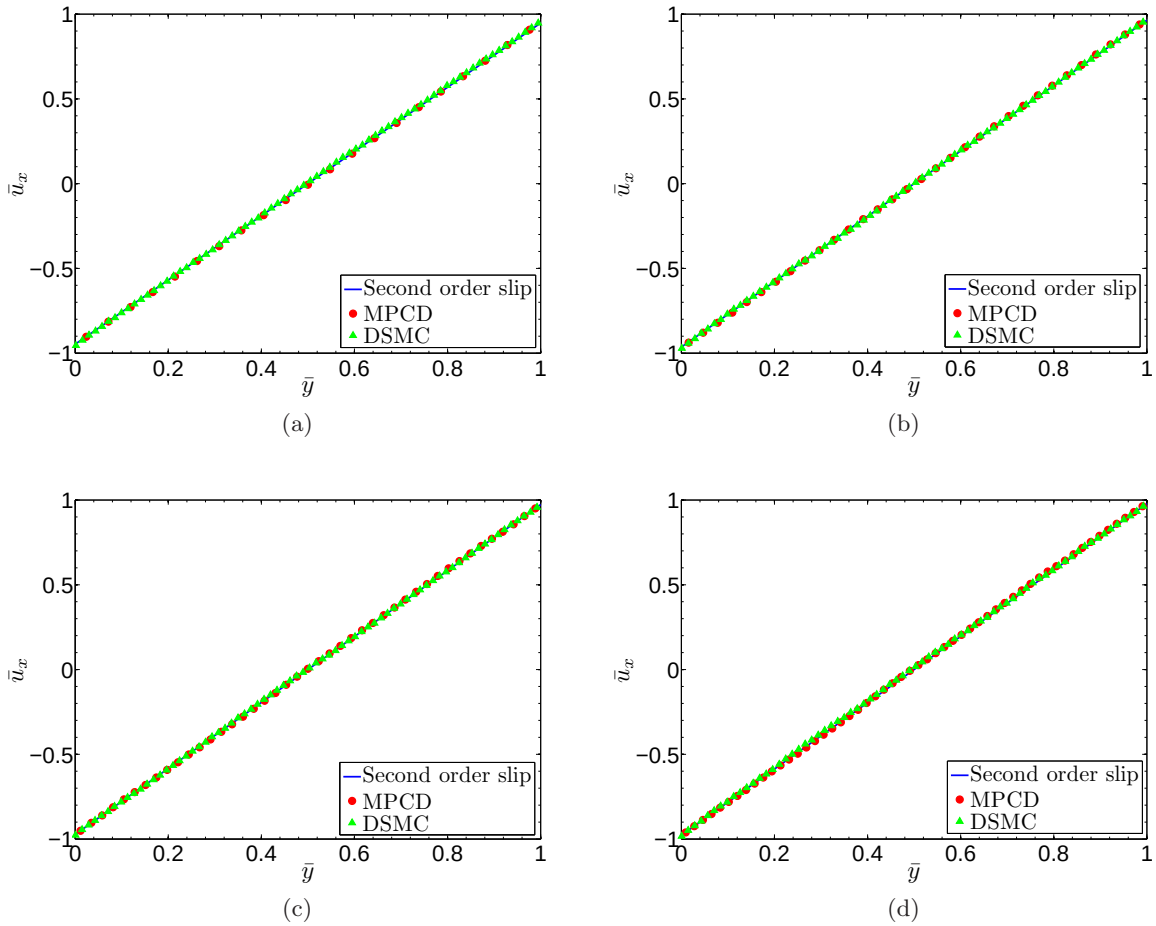

Figure 3.6: *Couette flow velocity profiles at different Knudsen numbers (a)* Kn = 0.025 *(b)* Kn = 0.0167 *(c)* Kn = 0.0125 *(c)* Kn = 0.01.

procedure can be expressed as:

$$\mathbf{v}_i^I(t+\delta t) = \mathbf{u}^I + s\mathbf{R}(\alpha)(\mathbf{v}_i^I(t) - \mathbf{u}^I), \tag{3.15}$$

where $\mathbf{v}_i^I$ is a particle in the I^{th} collision cell, $\mathbf{u}^I$ is the cell velocity, $\mathbf{R}(\alpha)$ is an MPCD multi-particle collision operator, and s the scaling factor. The scaling factor, s, is given by

$$s = \sqrt{\frac{k_{\mathrm{B}} T_{set} D(n-1)}{m \sum_{i=1} |\mathbf{v}_i^I - \mathbf{u}|^2}}. \tag{3.16}$$

In the above equation T_{set} is the desired temperature, D is the number of dimensions treated with the thermostat, and summation in the denominator is performed over all the particle in the I^{th} collision cell. In the simulations presented here, thermostats are used only in the z-direction, which means $D = 1$.

Fig.(3.7) shows that the measured viscosity using bounce back boundary condition is in good agreement with the analytical prediction for the range of α plotted. Furthermore, It is also visible in Fig.(3.7) that the measured viscosity with bounce back boundary condition does not match with that from diffuse wall boundary condition for small α. Here, we remind

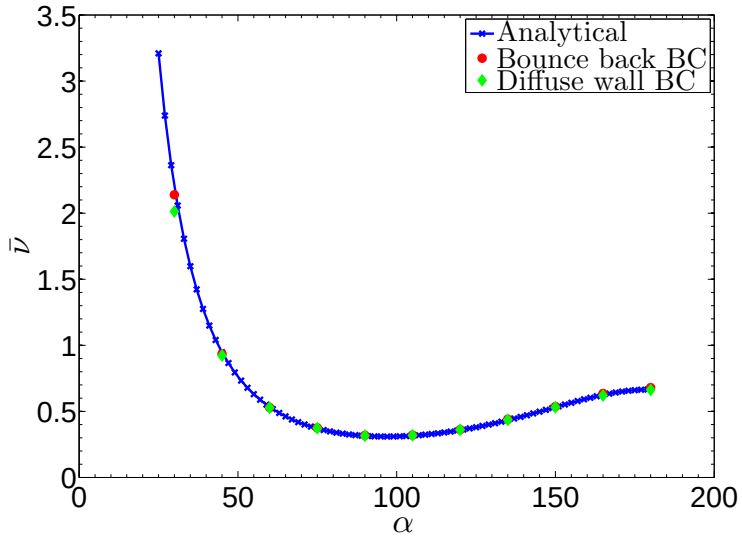

Figure 3.7: *Plot of kinematic viscosity, $\bar{\nu} = \nu/(a\sqrt{\frac{k_B T}{m}})$, with α from two sets of simulations with bounce back and diffuse wall boundary conditions. A good agreement between numerically measured viscosity and theoretical prediction is evident for the range of α plotted. It is clear that the measure viscosity with two boundary conditions do not match for $\alpha < 45^0$. The reason is evident in Fig.(3.8).*

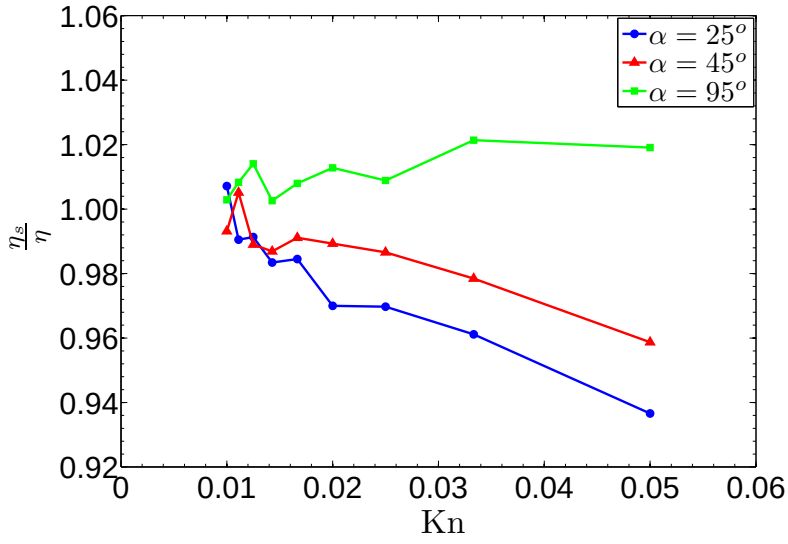

Figure 3.8: *Plot of measured viscosity (diffuse wall boundary condition) to predicted viscosity ratio, (η_s/η) with Knudsen number. Strong dependence of the viscosity ratio for small α can be seen in this plot.*

that the molecular chaos assumption can break down if collisions are weak (i.e. $\alpha \to 0$). For example, one can expect that at α close to zero, any particle will remember its past history for a longer duration. In Fig.(3.8), it can be seen that for small angles, $(\alpha < 45^0)$, the ratio of numerically observed viscosity to theoretical viscosity shows strong dependence on the Knudsen number. These observations suggest that there is a coupling between correlation related error and boundary related error, which needs to be investigated in details. As stated in section 3.4, this restrictions on α limits the range of Knudsen flows which can be simulated using MPCD.

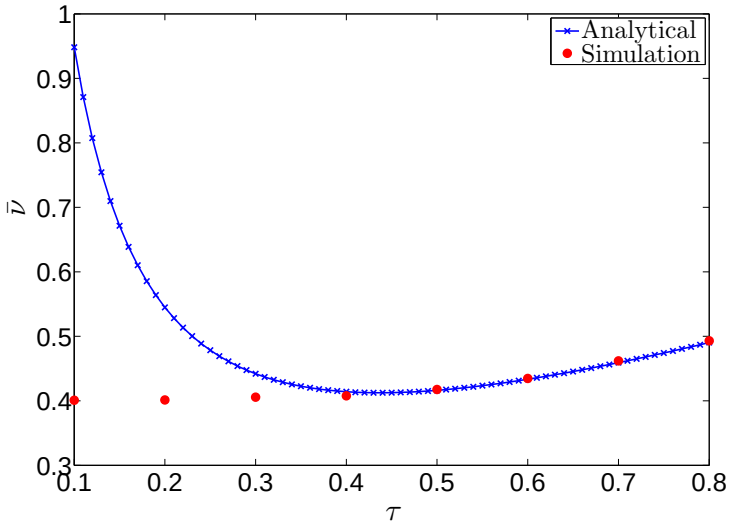

Figure 3.9: *Plot of kinematic viscosity, $\bar{\nu} = \nu/(a\sqrt{\frac{k_B T}{m}})$, with τ. In this figure it can be seen that measured viscosity do not match for $\tau < 0.4$ which indicates building up of correlations. This build up eventually leads to breakdown of Galilean invariance.*

In addition, measured kinematic viscosity with δt is plotted in Fig.(3.9) against the analytical result. We see that the numerical data starts departing form the analytical curve for $\tau < 0.4$. This indicates building up of correlations among the particles for smaller values of time step. These velocity correlations lead to the break down of Galilean invariance. As a result, anomalous behaviour is observed. It is observed that Galilean invariance can be resorted by applying the grid-shift (Ihle & Kroll 2001). However including grid-shift into MPCD algorithm is non-trivial, specially for the flow domain with walls. In the next chapter, a simplified algorithm is presented which reduces the correlation effects.

We have also studied velocity profiles for Kn $\in (0.01, 0.05)$. In Fig.(3.10), the velocity profiles obtained from MPCD simulations at different Knudsen numbers are plotted along with the analytical solution (Eq.(3.11)) and DSMC simulation data. In order to make the comparison possible, velocity is scaled with $U = \rho F_x L^2/2\eta$ (the prefactor in the Eq.(3.11)), and the distance from the bottom plate is scaled with L. From Fig.(3.10), it can be seen that numerical velocity profiles show a small deviation form the second order velocity slip profile. A possible reason for this deviation is that the theoretical prediction of viscosity does not exactly match with the measured viscosity in the simulation ($3-5\%$ error), i.e. the MPCD velocity profiles plotted here correspond to a fluid whose viscosity is slightly different from the value set for the simulation. Same is true for the DSMC data plotted here.

In gravity driven flow, another quantity of interest is the non-dimensional mass flow rate, defined as:

$$\bar{Q} = \frac{\tilde{u}_x}{L^2(\rho F_x)}\sqrt{\frac{2k_B T}{m}}, \tag{3.17}$$

where $\tilde{u}_x = \frac{1}{L}\int_0^L \rho u_x(y)dy$ is the average velocity in the channel. The second order velocity slip

model with correction due to Knudsen layer (Hadjiconstantinou 2003) predicts that

$$\tilde{u}_x = \frac{\rho F_x L^2}{2\eta}\left(\frac{1}{6} + \delta_1 \mathrm{Kn} + 2\beta \mathrm{Kn}^2\right), \tag{3.18}$$

where $\beta \approx 0.31$ is second order slip coefficient, modified due to the contribution from Knudsen layer. In Fig.(3.11), the non-dimensionalized mass flow rate as a function of Knudsen number obtained from the MPCD simulations is contrasted with mass flow rate curve obtained from the second order velocity slip model and the DSMC prediction. We see that the results are in good agreement.

Finally, It can be pointed out that, unlike MPCD simulations using bounce back, simulations using diffusive boundary condition can also predict temperature dynamics. As first check, temperature dynamics in gravity driven flows is investigated. The external force (per unit mass) is selected such that the flows remain subsonic. In particular, temperature profiles from MPCD simulations were investigated at different Knudsen numbers for two different Mach numbers-0.3, and 0.5. In these cases, the temperature profiles obtained from MPCD were contrasted with those obtained from DSMC simulations. It is evident from Fig.(3.12) that the temperature profile from MPCD is only qualitatively correct. We also observe that the agreement is usually better for the smaller Mach number (Ma = 0.3).

Lastly, we consider the pressure driven flows. In this set-up, the flow is driven by maintaining a pressure gradient between the inlet and the outlet. In experiments, the outlet is often kept at the atmospheric pressure while the flow is driven by maintaining a higher pressure at the inlet. In the continuum flow regime, the pressure is expected to vary linearly along the length of the channel for a subsonic (incompressible) flow. However, in microchannels the effects of compressibility and rarefaction both become important (Arkilic *et al.* 1997; Beskok *et al.* 1996). Moreover, it has been shown that rarefaction causes opposite effect than compressibility (Beskok *et al.* 1996).

Arkilic et al. (Ref. Arkilic *et al.* (1997)) have systematically studied 2D Navier-Stokes equations with first order velocity-slip boundary condition. The study is done for isothermal gas flows with slight rarefaction through long microchannels. They used perturbation expansion in smallness parameter ϵ, height-to-length ratio of the channel, and showed that at zeroth order we get following expression for the pressure along the channel:

$$\bar{p}_0(\bar{x}) = -6\delta_1 K + \sqrt{(6\delta_1 K)^2 + (1 + 12\delta_1 K)\bar{x} + (\mathscr{P}^2) + 12\delta_1 K \mathscr{P})(1 - \bar{x})} \tag{3.19}$$

where δ_1 is the first order velocity-slip coefficient, K is the Knudsen number at the exit of the channel, $\mathscr{P}$ is the inlet to outlet pressure ratio, $\bar{x}$ is the distance measure from inlet down the channel and is non-dimensionalized using length of the channel, and $\bar{p}_0(\bar{x})$ is the pressure at a point which is rescaled with pressure at the outlet. This non-linear pressure profile is shown to match well with the experimental data. Here, we have used this profile to compare the pressure data obtained from MPCD simulations.

The set-up used for simulating pressure driven flows is shown in Fig.(3.13). We have applied reservoir boundary conditions at the inlet and outlet in order to maintain constant pressures at the two ends of the channel. The reservoirs are created by extending the length of the channel

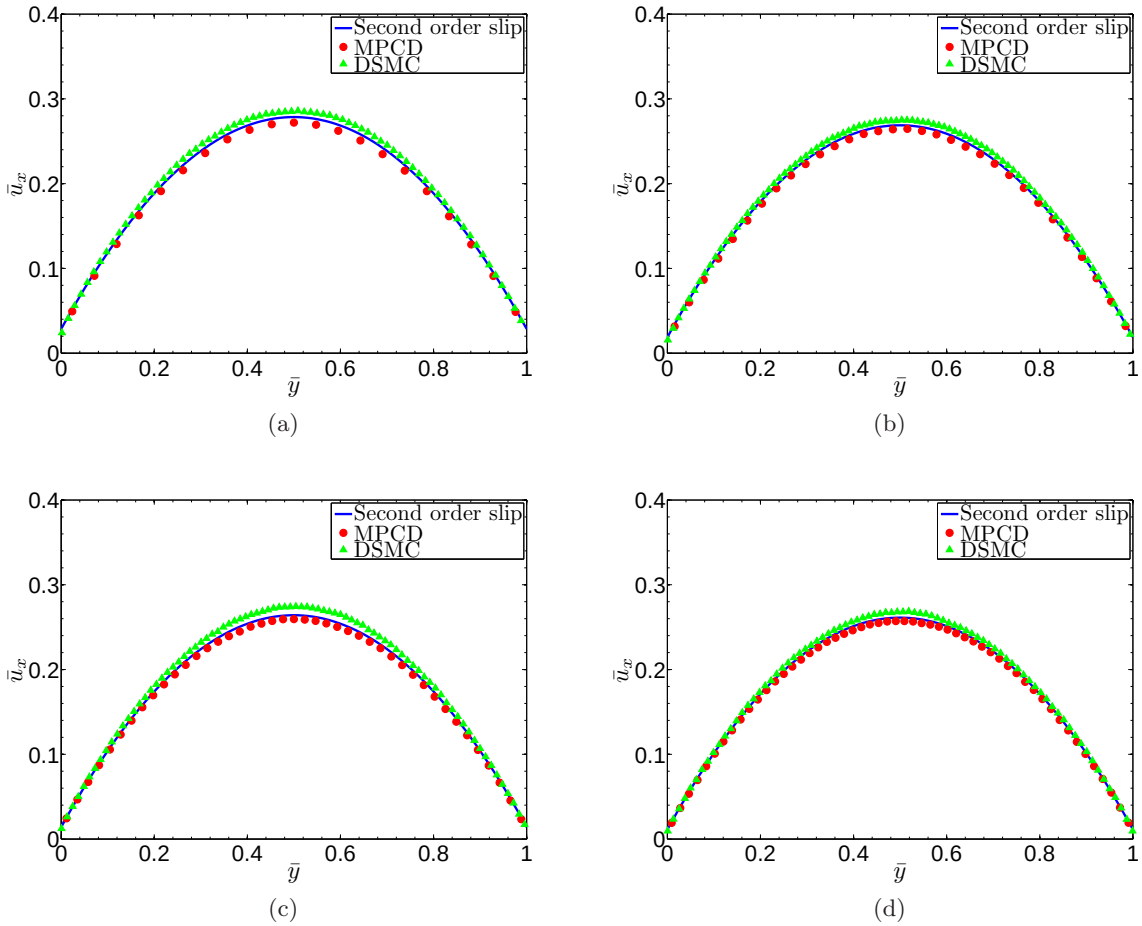

Figure 3.10: *Force driven flow velocity profiles at different Knudsen numbers (a)* Kn = 0.025 *(b)* Kn = 0.0167 *(c)* Kn = 0.0125 *(d)* Kn = 0.01.

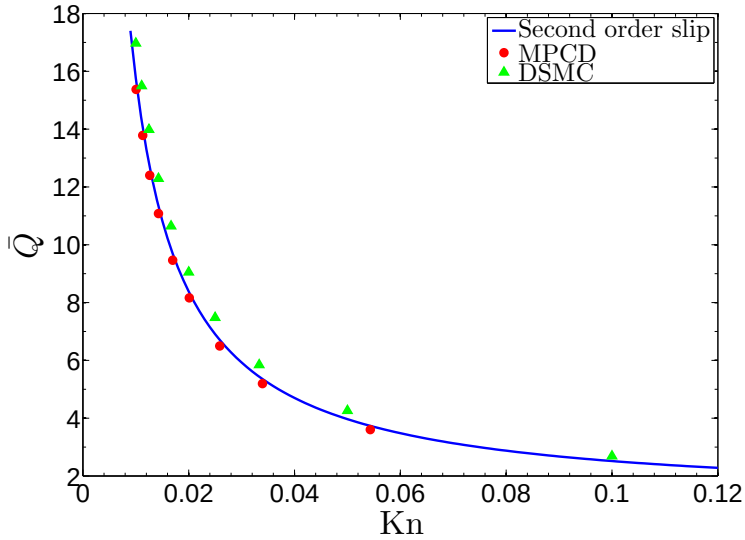

Figure 3.11: *Plot of mass low rate with Knudsen number,* Ma = 0.3.

in both directions. Before streaming, all the particles in the inlet reservoir are refreshed and temperature (T_{in}), pressure (p_{in}), and density (ρ_{in}) are set to that of the fluid entering the

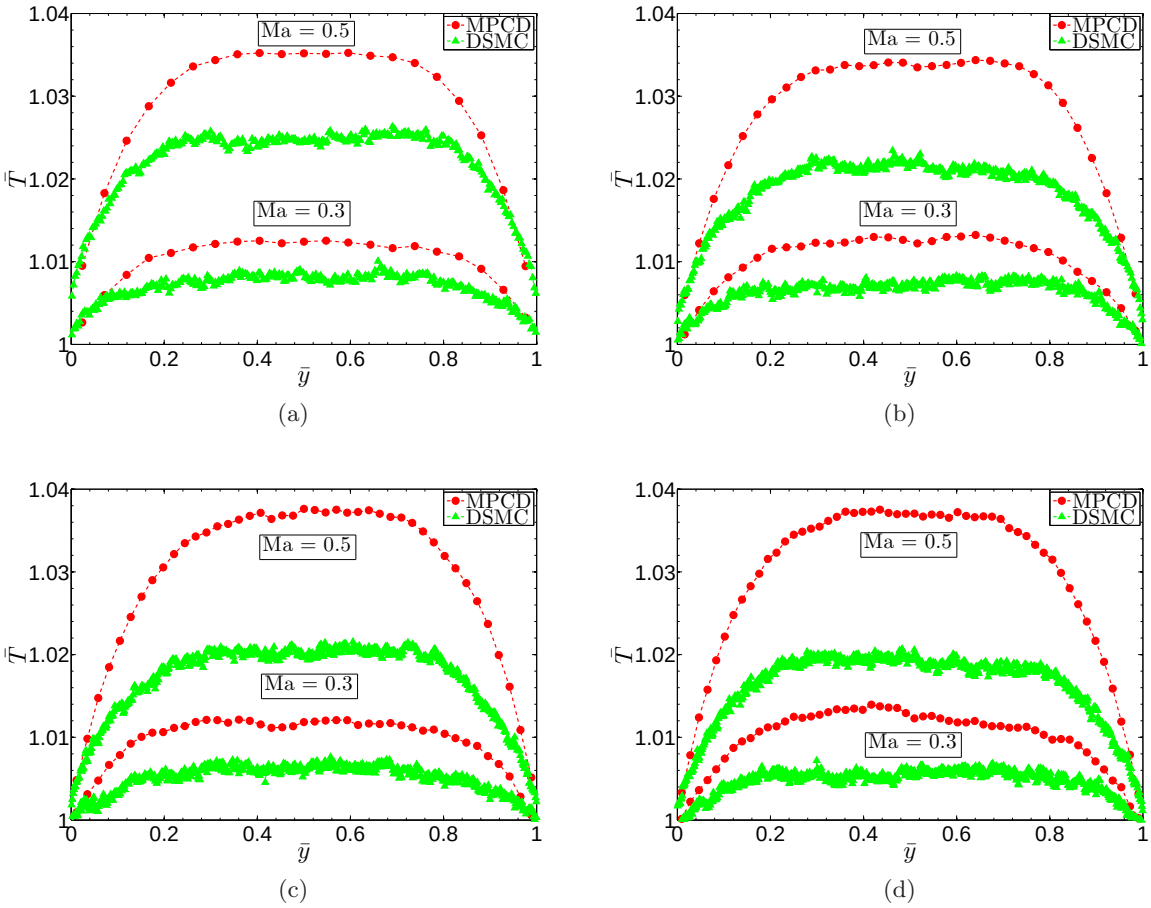

Figure 3.12: *Force driven flow temperature profiles at different Knudsen numbers (a)* Kn = 0.025 *(b)* Kn = 0.0167 *(c)* Kn = 0.0125 *(d)* Kn = 0.01.

channel which are known a priori. Thus total number of particles and temperature are always fixed in the inlet reservoir. In addition, average velocity is assigned to each particles such that, $\partial \mathbf{v}/\partial x = 0$, can be set at the inlet. This has been accomplished by imposing

$$\mathbf{v}_{in} = \mathbf{v}_{in+1}, \tag{3.20}$$

where $\mathbf{v}_{in}$ is the mean velocity in the reservoir which is set to be equal to $\mathbf{v}_{in+1}$, the velocity in cells adjacent to inlet boundary. Similarly pressure in the outlet reservoir is set to the outlet pressure (p_{-}). However, density, and the mean velocity are taken from the cells adjacent to the outflow boundary. Thus at the outlet we have:

$$\rho_{out} = \rho_{out-1}, \quad \mathbf{v}_{out} = \mathbf{v}_{out-1}, \quad p_{out} = p_{-}. \tag{3.21}$$

The subscript *out* corresponds to fluid properties in the outlet reservoir and *out-1* to the cells adjacent to the outflow boundary inside the channel. Moreover, the temperature (T_{out}) in the reservoir is imposed using p_{out} and ρ_{out}, and considering the gas to be ideal.

Selecting an appropriate length for the reservoirs is also important. If the length is small compared to the length of the channel then the calculated flow quantities can be incorrect. And

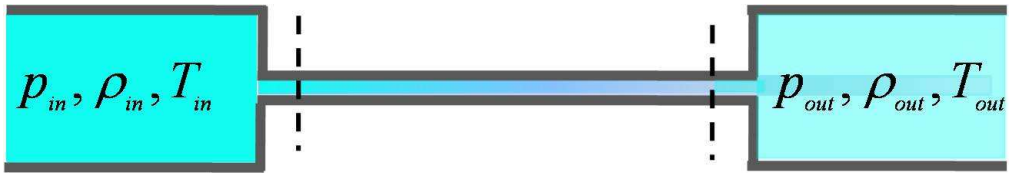

Figure 3.13: *Schematic of the set-up used for simulating pressure driven flows.*

if the length is too large compared to length of the channel then it might affect the flow properties in the bulk; the values appear to shift by an additive constant. However, for a sufficiently large channel changing the length of the reservoirs by small magnitudes does not change the flow properties. In present simulations length of the reservoirs, $L_r = 10 \times a$.

In pressure driven flows presented here, length to height ratio of the channel is 20; and a pressure ratio $\mathscr{P} = 1.9$ (few cell at the inlet and outlet are ignored in order to minimize boundary effects. For the complete length of channel $\mathscr{P} = 2.0$) is maintained for driving the flow. It is worth mentioning here that simulation of such a flow with DSMC is much more expensive.

In Fig.(3.14), pressure ($\bar{p}(x)$) is plotted with distance ($\bar{x}$) measured from the the inlet. The pressure has been non-dimensionalized with respect to exit pressure and the distance is non-dimensionalized with channel length. In this figure we observe that the measured pressure profile is basically linear. Note that MPCD can be used to simulate hydrodynamics for Re $\in (1 - 10)$ (Gompper *et al.* 2008). However, for Eq.(3.19) to remain valid, we need, Re $\sim$ O(ϵ), and Ma $\sim$ O(ϵ), at the exit. In the simulations presented here, at the exit, Re = 13.6, and Ma = 0.3.

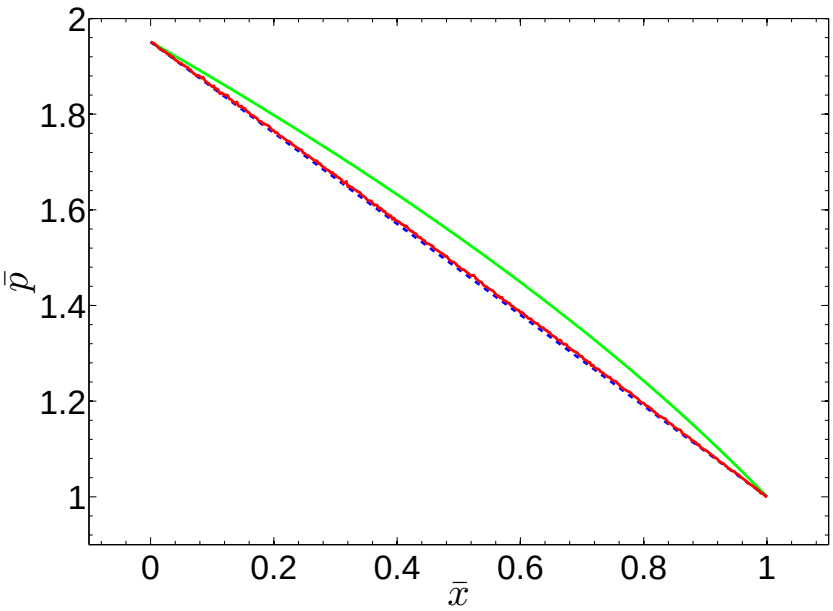

Figure 3.14: *Plot of pressure with distance from the inlet of the channel. The pressure is non-dimensionalized with the exit pressure whereas the length down the channel is non-dimensionalized with respect to the channel length. The simulation data is plotted in red dots, the analytical curve (Eq.(3.19)) and the linear pressure distribution curve are shown by the green solid line, and the blue dashed line, respectively.*

3.7 Outlook

Here we have shown that MPCD with diffuse wall boundary can predict velocity slip and temperature jump at the wall for finite Knudsen flows. However, there is a limit on Kn which can be simulated using MPCD (we have, Kn < 0.1). Moreover, there is a limit on Re as well, the preferred range for Re lies from 1 to 10. This makes MPCD not very suitable for simulating pressure driven flows, where Re is smaller than one. So far, with MPCD we have not been able to capture non-linear pressure distribution along the length of the channel which are linear in our simulations. We also find that quantitative agreement can be found for the velocity profile in shear and gravity flows. However, the obtained temperature profiles (gravity driven flows) are only qualitatively correct.

Chapter 4

Pseudo Binary Collision Model

4.1 Introduction

The multiparticle collision dynamics model is perhaps one of the simplest microscopic model of hydrodynamics. Due to the simplicity of the collision rule, the computational efficiency of the model is quite good. For example, compared to DSMC, only one random axis (two random numbers) per collision cell is required during the collision step, which makes the model quite efficient. Here, it should be reminded that in DSMC one needs to generate two random numbers for every selected pair of particles for collision. Furthermore, in MPCD the dynamics of every particle is coupled to other particles only via average velocity, which increases the inherent parallelism in the algorithm. However, as discussed in the last chapter, the method has a number of shortcomings too. For example, when time step (δt) is small, fluid properties predicted by the analytical expressions do not match with the simulation results. The reason is that for small δt many particles in a given collision cell undergo collisions for multiple time steps which leads to building up of correlations among them. Because of these correlations, the Galilean invariance of the system breaks down, and the system shows unphysical behaviour. Thus, for this numerical algorithm $\delta t \to 0$ limit does not exist. Though, the random grid-shift method partially resolves the issue, we find the absence of consistency in the continuum limit unsatisfactory.

Here, a simple solution to this problem of ensuring Galilean invariance at small time steps is suggested by modifying the collision rule of the MPCD algorithm. The new collision model (pseudo binary collision) presented in this chapter is motivated by the Monte Carlo binary collision model for plasma dynamics (Wang *et al.* 2008). In pseudo binary collision model, the multipartile collisions in MPCD algorithm are replaced by two particle collisions between randomly chosen particle pairs. It is clear that selecting same pair of particles for collisions over multiple time steps is quite unlikely, considering that the time step is short enough, and the particles remain in the same collision cell. Consequently, the velocity correlations among particles do not build up. The present method, can also be viewed as an hybrid between DSMC and MPCD, where MPCD rotation procedure is applied to carry out binary collisions used in DSMC.

The chapter is organized as follows: in section 4.2, collision rules are explained for the pseudo binary collision model. In section 4.3, relaxation of the MPCD system with pseudo binary collision model to an equilibrium configuration is investigated, and the result shows that, as in MPCD with multiparticle collisions, the velocity distribution is Maxwellian. Expressions

for predicting kinetic and collisional viscosities are derived in section 4.4. The kinetic theory approach (Kikuchi *et al.* 2003) is again followed for deriving the expressions. In section 4.5, subcell structure is proposed for a collision cell with the aim of reducing the contribution to collisional viscosity by making collisions relatively local. In section 4.6, gaseous microflows are studied with this model in order to access its kinetic nature, and we find that it behaves very similar to the standard MPCD algorithm. Here, we also show that with this collision model Galilean invariance is ensured for small time steps. Finally, in section 4.7, some remarks are made based on the results obtained.

4.2 Pseudo Binary Collision Model (PBCM)

In this section, a modified collision rule is proposed where the key new idea is to replace the multiparticle collisions in MPCD (standard MPCD) with binary collisions, while keeping the concept of velocity rotation for carrying out the collisions intact. In order to perform collisions all particles in a collision cell are listed randomly and $M/2$ particle pairs (for even M) are formed. The velocity of each particle is then rotated by a constant angle α (rotation angle) in a reference frame moving with the centre of mass velocity of the two particles about an axis (rotation axis) chosen randomly. Thus for a pair of particles $\mathbf{v}_i^I(t)$, and $\mathbf{v}_j^I(t)$ chosen randomly in the I^{th} cell, the collision routine modifies to

$$\begin{aligned}\mathbf{v}_i^{(I)}(t+\delta t) &= \frac{\mathbf{v}_i^I(t)+\mathbf{v}_j^I(t)}{2} + \mathbf{R}(\alpha)\frac{\mathbf{v}_i^I(t)-\mathbf{v}_j^I(t)}{2},\\ \mathbf{v}_j^{(I)}(t+\delta t) &= \frac{\mathbf{v}_i^I(t)+\mathbf{v}_j^I(t)}{2} - \mathbf{R}(\alpha)\frac{\mathbf{v}_i^I(t)-\mathbf{v}_j^I(t)}{2},\end{aligned} \tag{4.1}$$

where $\mathbf{R}(\alpha)$ is a rotation matrix and α is the angle of rotation. Here it is emphasized that same rotation axis is used for all the collisions inside a collision cell. Moreover, rotation axes are stochastically independent for different cells at a given time and also for a given cell at different times. Also, note that a small modification in the collision rule is required when there are odd number of particles in the cell. In such cases, last three particles are grouped together after all the particles in the cell are listed randomly. On this group of three particles, three pseudo binary collisions are performed on pairs with particles taken two at a time (preferred choice), or a three particle MPCD collision is performed.

It is evident that similar to standard MPCD, current algorithm has correct collisional invariants. Furthermore, the detailed balance is intact and thus connection with Boltzmann dynamics is evident. As the collisions have correct invariants and detailed balance is not violated, it is reasonable to expect that the equilibrium for current model is Maxwell-Boltzmann distribution. The qualitative motivation behind the current model is that due to binary nature of collisions, one would expect that even for relatively small time steps used in simulations, a given particle will not collide with the same partner in the subsequent time-steps. Thus, unphysical correlations are expected to be less severe in this model.

Finally, it should be pointed out that the pseudo-binary algorithm proposed here is quite similar to the algorithm of plasma dynamics developed by Takizuka & Abe and Nanbu (Takizuka & Abe 1977; Nanbu 1997) in the way particles are considered for collisions. However, the

methods differ in details for calculating the post collisional velocities. Furthermore, three particle collisions proposed here is again a peculiarity of MPCD.

4.3 Relaxation to Equilibrium

Similar to MPCD, the pseudo-binary collision model described in last section conserves mass, momentum and energy. In case of MPCD, it is argued that, if ergodicity condition holds, the stationary distribution for the MPCD system is microcanonical, and the single particle distribution is Maxwell-Boltzmann distribution

$$f^{MB}(\mathbf{v}) = \frac{N}{V}\left(\frac{m}{2\pi k_{\mathrm{B}}T}\right)^{\frac{3}{2}} e^{-\frac{mv^2}{2k_{\mathrm{B}}T}}, \tag{4.2}$$

in the limit of large system size (Malevanets & Kapral 1999). Here, N is total number of particles in the system and V is the volume of the simulation domain. Using numerical simulations it has been shown that standard MPCD system indeed relaxes to Maxwell-Boltzmann distribution. As the current collision model has correct invariants, and satisfies detail balance conditions on collision (Liboff 1983), one would expect that the equilibrium is Maxwell-Boltzmann for this model too.

In Fig.(4.1), relaxation of MPCD with pseudo binary collision model to equilibrium is shown. Here, a subtle difference can be observed between MPCD with multiparticle collisions and pseudo binary collisions. Note that in the simulation only one collision cell is used and yet the system relaxes to Maxwell-Boltzmann distribution. However, the same is not possible for standard MPCD. It has been observed that for standard MPCD, fluctuation in $\mathbf{u}$ is required for the system to relax. Therefore, in a system with only one collision cell no appreciable relaxation to Maxwell-Boltzmann-distribution can be observed. MPCD with pseudo binary collisions does not suffer from this limitation, i.e. the system relaxes to Maxwell-Boltzmann distribution even with a single collision cell. We also note that the scenario presented here is only hypothetical, no practical simulation would involve just one cell, as with just one point we can not hope to approximate a flow domain.

4.4 Viscosity

In this section, the procedure used in standard MPCD for viscosity evaluation (see Kikuchi *et al.* (2003), or Chapter 2 for a detailed derivation) is repeated for the PBCM. For the sake of completeness all the relevant steps are listed gain in this section. Similar to standard MPCD, the fluid modeled by PBCM has two distinct contributions to the viscosity. The first contribution is due to transport of momentum by the movement of particles and is termed as kinetic contribution. The second contribution, termed as collisional viscosity, is due to non-local collisions.

4.4.1 Kinetic Viscosity

In order to calculate the kinetic part of the viscosity, as described in Chapter 2, a system undergoing shear in x-direction, with shear rate $\dot{\gamma} = \partial u_x(y)/\partial y$, is considered. As it is derived

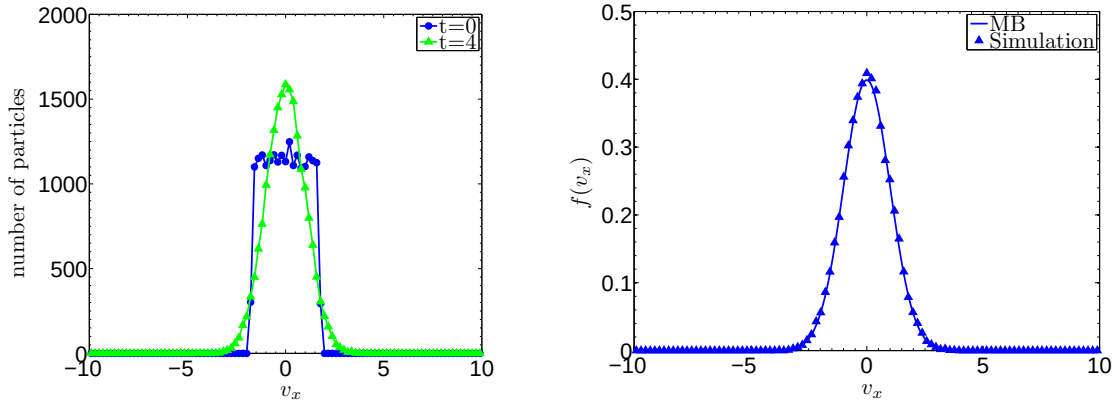

(a) (b)

Figure 4.1: *(a) Distribution of x-velocity component is plotted at initial time ($t = 0$) and after four time iterations ($t = 4$). (b)The velocity distribution (triangles) is rescaled to match the Maxwell-Boltzmann distribution at system temperature (solid line). These two figures clearly indicate that the system relaxes quite fast and the steady state distribution is Maxwell-Boltzmann (When the simulation is run for longer times, it does not show any significant changes in the distribution function). This simulation is run with 20000 particles at $k_BT = 1.0$. Only one cell (with periodic boundary condition in all three directions) is considered for the simulation.*

there (see subsection 2.3.1), $\langle v_x v_y \rangle$ after advection can be related to before advection value as:

$$\langle v_x v_y \rangle^{after} = \langle v_x v_y \rangle - \dot{\gamma} \langle v_y^2 \rangle \delta t, \tag{4.3}$$

As compared to standard MPCD, collision step is different in PBCM, so $\langle v_x v_y \rangle$ after collision needs to be estimated for this model. Similar to the calculation done for the standard MPCD, the Ith collision cell with n particles is considered, where in a collision step the velocities of a pair of particles get updated according to Eq.(4.1).

Firstly, for any pair of particle denoted by index i and j, due to the molecular chaos approximation, we have:

$$\langle (v_{ix} + v_{jx})(v_{iy} + v_{jy}) \rangle = \langle v_{ix} v_{iy} + v_{jx} v_{jy} \rangle = 2 \langle v_{ix} v_{iy} \rangle \tag{4.4}$$

Similarly,

$$\langle (v_{ix} - v_{jx})(v_{iy} - v_{jy}) \rangle = \langle v_{ix} v_{iy} + v_{jx} v_{jy} \rangle = 2 \langle v_{ix} v_{iy} \rangle . \tag{4.5}$$

We intend to calculate the velocity correlation after collision, $\langle v_x(t + \delta t) v_y(t + \delta t) \rangle$, with i^{th} particle in the collision cell taken as the test particle. The velocity correlation can be expressed as

$$\langle v_{ix}(t + \delta t) v_{iy}(t + \delta t) \rangle = \frac{1}{4} \cos(2\alpha) \langle (v_{ix} - v_{jx})(v_{iy} - v_{jy}) \rangle + \frac{1}{4} \langle (v_{ix} + v_{jx})(v_{iy} + v_{jy}) \rangle . \tag{4.6}$$

Finally, substituting the expressions for $\langle (v_{ix} - v_{jx})(v_{iy} - v_{jy}) \rangle$ and $\langle (v_{ix} + v_{jx})(v_{iy} + v_{jy}) \rangle$ from Eq.(4.4), and Eq.(4.5), respectively into Eq.(4.6), we get

$$\langle v_x(t+\delta t)v_y(t+\delta t)\rangle = \frac{1}{2}(1+\cos 2\alpha)\langle v_x(t)v_y(t)\rangle = f(\alpha, M)\langle v_x(t)v_y(t)\rangle. \tag{4.7}$$

In the above equation we have dropped the index i, as all the particle are identical.

Hence we see that the velocity correlation $\langle v_x(t)v_y(t)\rangle$ first decreases due to streaming and then gets multiplied by a factor $f(\alpha, M)$ after the collision. Thus, in steady state following self-consistency condition must hold:

$$\langle v_x v_y\rangle = -\frac{\dot{\gamma}\delta t f}{1-f}\langle v_y^2\rangle. \tag{4.8}$$

As a result, we get following expression for the shear stress:

$$\sigma_{xy} = \rho\dot{\gamma}\delta t\langle v_y^2\rangle\left(\frac{1}{2}+\frac{f}{1-f}\right), \tag{4.9}$$

From the above equation, the expression for the kinetic viscosity can be extracted, and by using the equipartition argument, $\langle v_y^2\rangle = k_{\mathrm{B}}T/m$, we get

$$\eta_{kin}^{2D} = \frac{\rho k_{\mathrm{B}}T\delta t}{2m}\left[\frac{4}{(1-\cos 2\alpha)}-1\right]. \tag{4.10}$$

It is evident that transport coefficient in present model is same as MPCD with $M = 2$. Using this argument, in 3D we have:

$$\eta_{kin}^{3D} = \frac{\rho k_{\mathrm{B}}T\delta t}{2m}\left[\frac{10}{(2-\cos\alpha-\cos 2\alpha)}-1\right]. \tag{4.11}$$

4.4.2 Collisional Viscosity

In order to get an estimates for the collisional contribution to viscosity (Kikuchi *et al.* (2003)), the momentum transfer across a plane (y_0), which divides the collision cell into two subcells (upper and lower), is calculated during a collision step. Here n is the total number of particles in a cell, and n_1 and n_2 are number of particles in the upper and the lower subcells, respectively (see Chapter 2 for details).

In pseudo binary collisions, momentum exchange between the two subcells takes place only when the the two particles in a collision pair lie in different subcells. In general, there are $n(n-1)/2$ different collisions possible during a collision step. Among all the collisions, only $n_1 n_2$ collisions will result in the momentum exchange. Therefore, the probability that a collision results in momentum exchange between the two subcells is $2n_1n_2/n(n-1)$, and there are total $n/2$ collisions in a given time step; this results in the total momentum exchange between subcells to be proportional to $n_1n_2/(n-1)$. Thus, the shear stress can be given by

$$\sigma_{xy} = \frac{m}{a^{D-1}\delta t}\left[\frac{2}{D}\frac{n_1n_2}{n-1}(1-\cos\alpha)\frac{(u_{1x}-u_{2x})}{2}\right] \tag{4.12}$$

Considering the average velocities in the two subcells, the above equation can be written as

$$\sigma_{xy} = \frac{m}{2a^{D-2}\delta t}\left[\frac{1}{D}\frac{n_1 n_2}{n-1}(1-\cos\alpha)\right] \tag{4.13}$$

We assume that the probability of finding a particle in a subcell is proportional to the subcell area. This implies that the number of particles in the upper subcell, n_1, follows binomial distribution with $p = (1 - y_0/a)$, and $q = y_0/a$. When we take the average over all possible n_1, the equation reduces to

$$\eta_{col} = \frac{m(1-\cos\alpha)}{a^{D-2}D\delta t} n \frac{y_0}{a}\left(1-\frac{y_0}{a}\right) \tag{4.14}$$

where we have used the fact that for a binomially distributed random variable, n_1, $\langle n_1\rangle = np$ and $\langle n_1^2\rangle = npq + n^2p^2$, where n is maximum number of particles that the subcell can accommodate. Furthermore, ignoring any fluctuations in n (i.e. $n = M$, where M is average number of particles in a collision cell), and averaging for $0 < y_0 < a$, we obtain the final expression for the collisional viscosity. This is given by

$$\eta_{col} = \frac{m(1-\cos\alpha)}{12a^{D-2}D\delta t} M \tag{4.15}$$

In 2D and 3D, collisional contributions are thus given by

$$\eta_{col}^{2D} = \frac{m(1-\cos\alpha)}{24\delta t} M, \quad \eta_{col}^{3D} = \frac{m(1-\cos\alpha)}{36a\delta t} M. \tag{4.16}$$

As we mentioned before total viscosity, η^{2D}, of an MPCD fluid is a sum of kinetic and collisional viscosities. Using Eqs. ((4.10)) and ((4.15)), it can be expressed as

$$\eta^{2D} = \frac{\rho k_B T \delta t}{2m}\left[\frac{4}{(1-\cos 2\alpha)} - 1\right] + \frac{m(1-\cos\alpha)}{24\delta t} M. \tag{4.17}$$

Following the steps outlined in this section for a 3D system, we can arrive at a similar expression for the viscosity, given as

$$\eta^{3D} = \frac{\rho k_B T \delta t}{2m}\left[\frac{10}{(2-\cos\alpha-\cos 2\alpha)} - 1\right] + \frac{m(1-\cos\alpha)}{36a\delta t} M, \tag{4.18}$$

where the first term on the right hand side corresponds to the kinetic contribution to the viscosity, and the second term that of the collisional contribution.

Here we point out that the viscosity expressions have not be confirmed by numerical simulations. Each contribution to the viscosity can be obtained in a simulation following the methodology used in Kikuchi *et al.* (2003). However, with the expressions derived in this section, we hope to capture the right qualitative behaviour of the viscosity dependence on different parameters (e.g. δt, M). These expressions seem to give a reasonably good prediction for the overall viscosity (Fig. 4.3) for $\alpha > 90^0$.

4.5 PBCM with Subcell

From Eq.(4.15), it can observed that the collisional contribution is approximately half of what we get for standard MPCD. Here, we again emphasize that collisional contribution to viscosity is

an artifact of non-local discrete collisions in MPCD, and there is no counterpart to this viscosity contribution in the kinetic theory. This viscosity contribution can be reduced further by making collisions relatively local by dividing collision cells into subcells. Thus, collisions are performed considering only those particles inside a subcell. We refer to this pseudo binary collision model with subcell structure as PBCM-Subcell. We see that this procedure is very similar to DSMC for choosing collision pairs, which is done for ensuring that particle pairs in close proximities undergo collisions.

It is evident that the kinetic contribution to the viscosity remains unchanged for pseudo binary collision model with subcell structure (Eq.(4.10) and Eq.(4.11)), but the collisional contribution reduces substantially. The collisional viscosity for the subcell model (PBCM-Subcell) can be given as

$$\eta_{col} = \frac{m(1-\cos\alpha)}{12.0 a_s^{d-2} d\delta t} M_s, \tag{4.19}$$

where a_s is length of the subcell and M_s is the average number of particle per subcell. If there are n_s divisions ($n_s = 2$ is chosen in this work) made in each coordinate directions for constructing subcells, we get $a_s = a/n_s$ and $M_s = M/(n_s^D)$, where D is the dimensionality of the problem. In calculating M_s we assume that particles are uniformly distributed in each cell.

4.6 Gaseous Microflows

It was shown in the last chapter that, with standard MPCD, the simulations were reliable when the rotation angles (α) were greater than 90^0. It was also shown that simulations of finite Knudsen flows, Kn < 0.1, were feasible. In this section, the objective is to use the same canonical set-ups for PBCM-Subcell in order to establish its range of applicability in terms of Knudsen number. As with standard MPCD (Chapter 3), three different flow setups - shear driven flows, gravity driven flows, and pressure driven flows are analyzed. Furthermore, the obtained results are compared with those from the second order velocity-slip model, and DSMC simulations of hard sphere gas molecules. The results are also compared with that of standard MPCD, if possible.

In all the simulations the mass of each particle, $m = 1$, the particle diameter, $\sigma = 1$, and the energy was measured in the units of $k_{\mathrm{B}}T/m$. Here also, the mean free path (λ) is defined based on the viscosity, pressure (p), and temperature (T) of the system as

$$\lambda = \frac{\eta}{p}\sqrt{\frac{\pi RT}{2}} \tag{4.20}$$

where η is the viscosity and $R = k_{\mathrm{B}}T/m$ is the gas constant. Based on the mean free path define above (Eq.(4.20)), an estimate for the Knudsen number can be obtained, which is

$$\mathrm{Kn} = \frac{\lambda}{\mathrm{L}}, \tag{4.21}$$

where L is the separation between the confining walls. In simulations Knudsen number was changed by varying L. In addition, the values of temperature and Boltzmann constants were set as: $T = 1$, and $k_{\mathrm{B}} = 1$, except in pressure driven flow scenario where $k_{\mathrm{B}} = 0.5$ was chosen. The

density of the gas, $\rho = 1.21 \times 10^{-03}$, was set and the average number of particles per collision cell, M, was fixed to 80 (i.e. 10 per subcell). The cell size (a) obtained form this value of M and the gas density is 40.436. Similar to MPCD simulations (see Chapter 3) the time factor, τ, defined as

$$\tau = \frac{\delta t \sqrt{\frac{k_B T}{m}}}{a}, \tag{4.22}$$

was chosen to be 0.6. For the DSMC simulations (the code was developed following Alexander & Garcia (1997)) for the same density and temperature, the mean free path value is $\lambda \approx 182.04$ (Eq.(4.20)). In order to get an estimate of viscosity, $\eta = 5m\pi^{1/2}(RT)^{1/2}/(16\sigma)$, is used. In DSMC simulations number of particles per collision cell (M) was taken as 20. Furthermore, time step used for streaming was roughly $0.1 \times \tau_c$, where $\tau_c = \lambda/\sqrt{k_B T/m}$, is a measure of the mean free time.

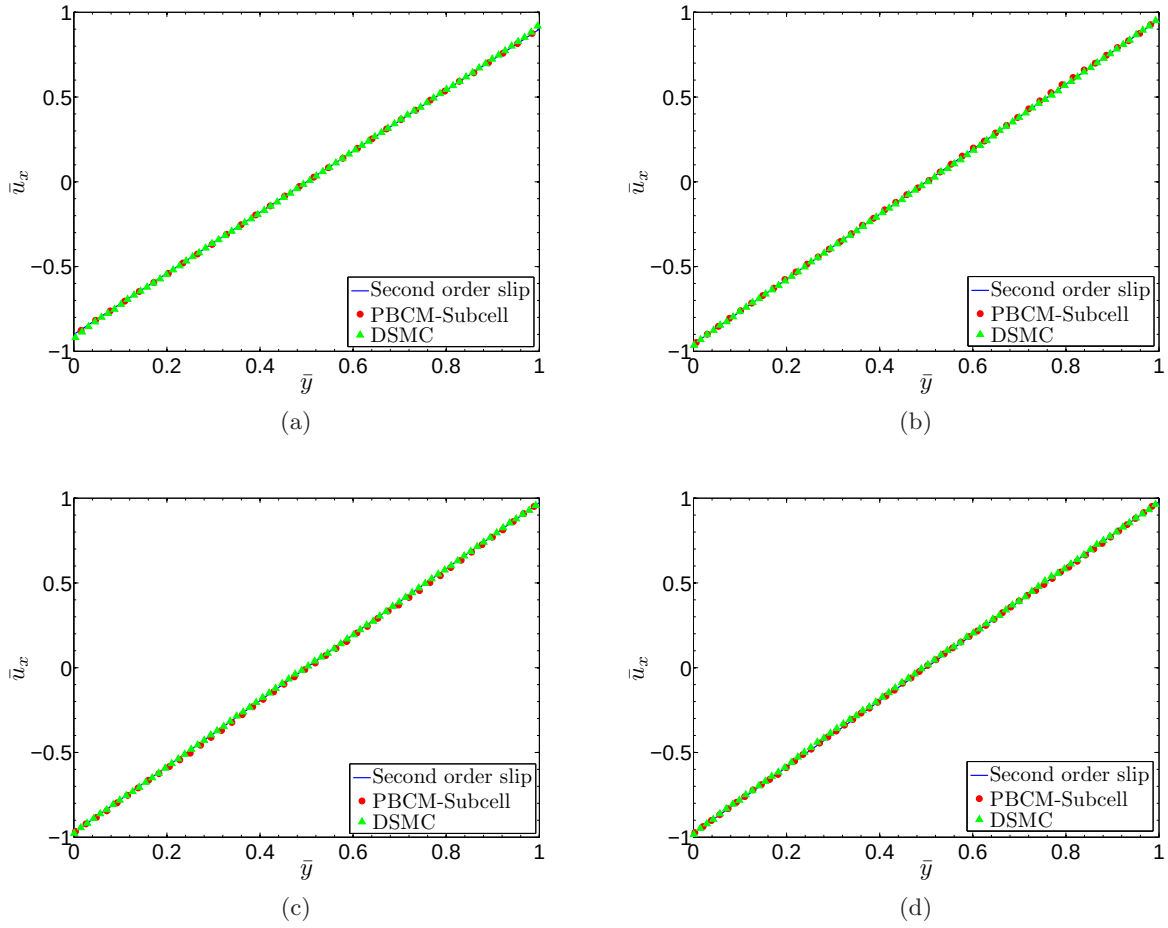

Figure 4.2: *Couette flow velocity profiles at different Knudsen numbers (a)* Kn = 0.05 *(b)* Kn = 0.02 *(c)* Kn = 0.0125 *(c)* Kn = 0.01.

As the first test, shear driven flows was considered for Kn $\in (0.01, 0.1)$. Similar to standard MPCD, $U_1 = -U_W = -0.2$, and $U_2 = U_W = 0.2$ were chosen, where U_w is the magnitude of the wall velocities. In Fig.(4.2), dimensionless velocity (scaled with U_w) is plotted as a function of distance for various values of the Knudsen number. These plots show good agreement with the DSMC and the second order velocity-slip model results. Also, due to insufficient time averaging,

at lower Knudsen numbers, wave like structures around mean straight-line profiles is visible upon zooming.

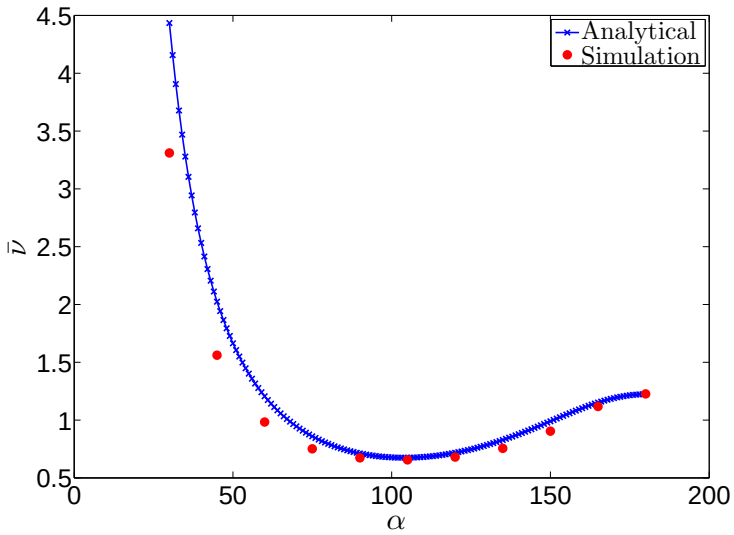

Figure 4.3: *Plot of kinematic viscosity,* $\bar{\nu} = \nu/(a\sqrt{\frac{k_B T}{m}})$*, with* α*. A good match between analytical curve and numerical data can be observe for* $\alpha > 90^0$

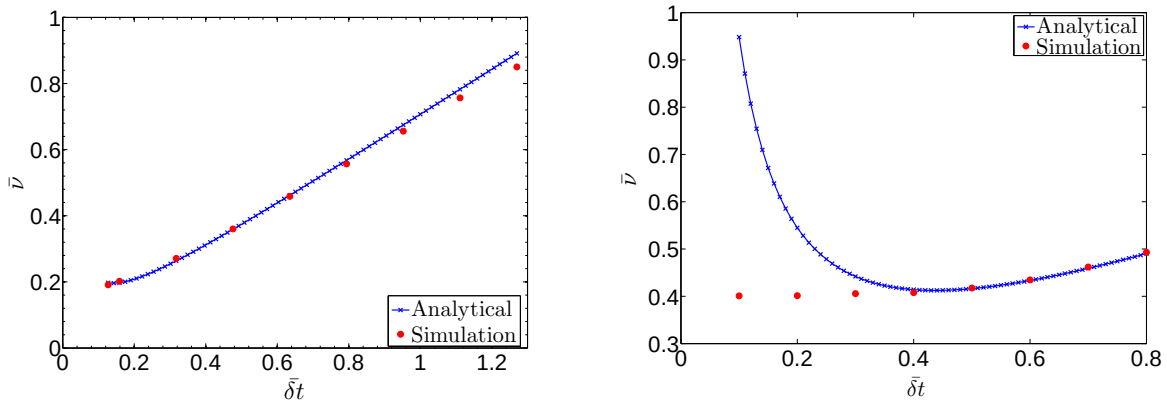

Figure 4.4: *Plot of kinematic viscosity,* $\bar{\nu} = \nu/(a\sqrt{\frac{k_B T}{m}})$*, with* $\bar{\delta t} = \delta t/\left(\hat{a}/\sqrt{\frac{k_B T}{m}}\right)$*, where* $\hat{a}$ *corresponds to a cell size with* 20 *particles. (a) PBCM-Subcell (b) standard MPCD. It is clear from this figure that for* $\bar{\delta t}$ *as small as 0.15 agreement between numerical data and analytical predictions is quite well which implies velocity correlations do not build at these time steps with PBCM-Subcell. However, with standard MPCD the numerical estimate deviates considerably for* $\bar{\delta t} < 0.4$*.*

As the second test, gravity driven flows were considered. The viscosity of the fluid was measured for different values of α. Fig.(4.3) shows that the measured viscosity match well with the analytical curve for $\alpha > 90^0$. In Fig.(4.4), the kinematic viscosity as a function of time step is plotted. In contrast to standard MPCD, the numerical results are in good agreement with the theoretical result even for small time steps. As shown in Fig.(4.4b), for MPCD simulations the

measured viscosity does not match with the analytical prediction for $\bar{\delta}t < 0.4$, because of the velocity correlations among the particle. This result clearly indicates that with PBCM-Subcell the problem of velocity correlations among the particles is reduced substantially.

Furthermore, in Fig.(4.6), the mass flow rate is plotted, and good agreement with the DSMC and the second order velocity-slip predictions is visible. Thus, for Kn < 0.1, (or may be slightly larger value for Kn) PBCM-Subcell shows a good representation of hydrodynamics. To have more quantitative comparisons, in Fig.(4.5), the dimensionless velocity profiles for gravity driven flows are contrasted with the DSMC data and the second order velocity-slip solutions. We observe that near the wall slip is captured well with PBCM-Subcell, and there is a good match with the DSMC data. However, near the center line of the channel the velocity profiles for PBCM-Subcell and DSMC show small deviations from the second order velocity-slip profile. The reason is that the viscosities estimated for DSMC and PBCM-Subcell fluids do not match exactly with the measured viscosities in the simulations; for DSMC it is overestimated while for PBCM-Subcell it is underestimated. We also note that the difference between the two viscosities (analytical and numerically measured) remains smaller than 5% for both the methods.

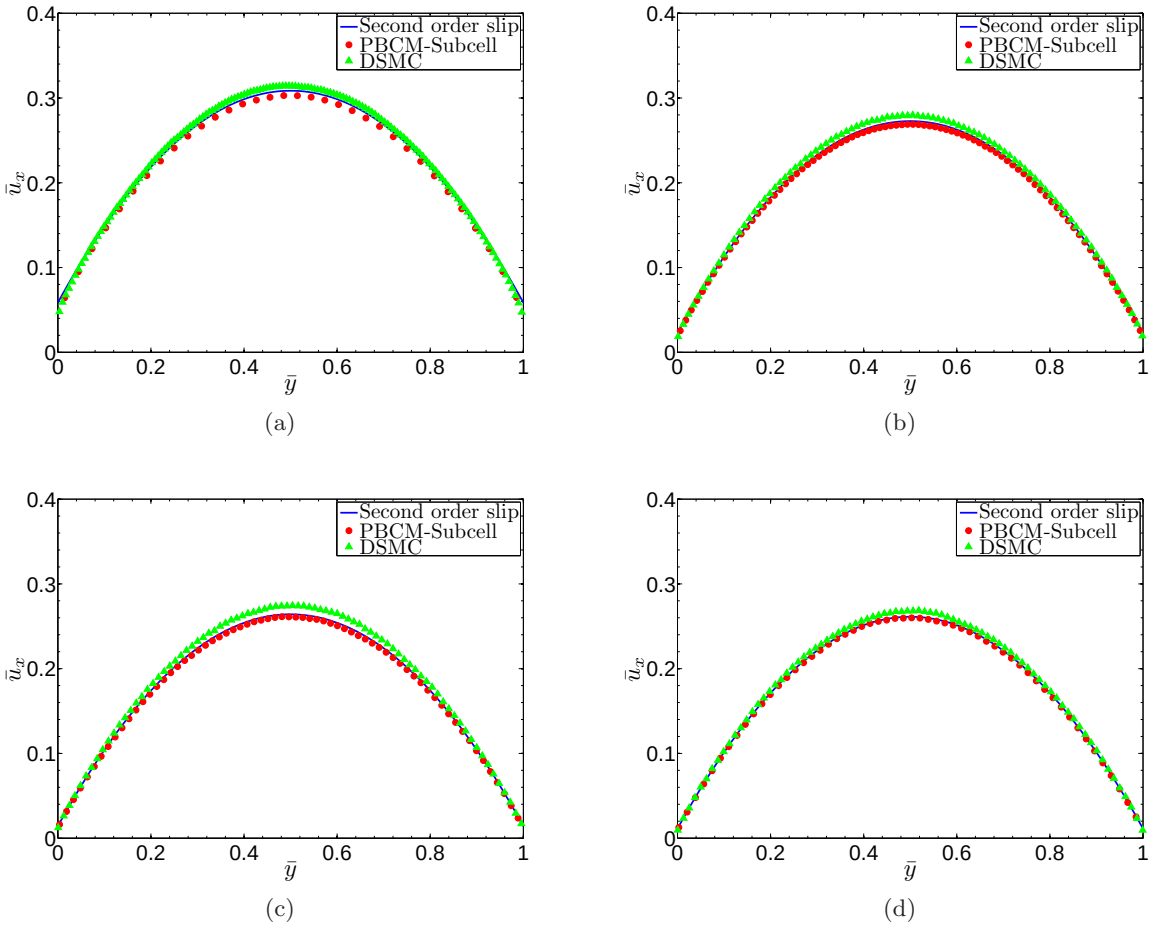

Figure 4.5: *Gravity driven flow velocity profiles at different Knudsen numbers (a)* Kn $= 0.05$ *(b)* Kn $= 0.02$ *(c)* Kn $= 0.0125$ *(c)* Kn $= 0.01$.

Finally, for the gravity driven flow set-up, the temperature profile obtained from PBCM-Subcell are contrasted with the corresponding DSMC data in Fig.(4.7). Though, the agreement

is only qualitative, it is better at Ma = 0.3 than at Ma = 0.5. Furthermore, the temperature profiles from PBCM-Subcell are always over-predicted compared to the DSMC data.

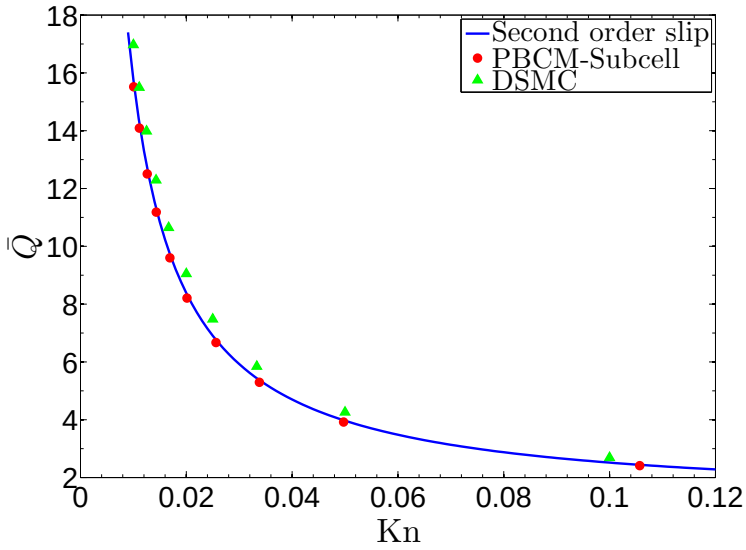

Figure 4.6: *Plot of non-dimensional mass flow rate with* Kn*;* Ma = 0.3.

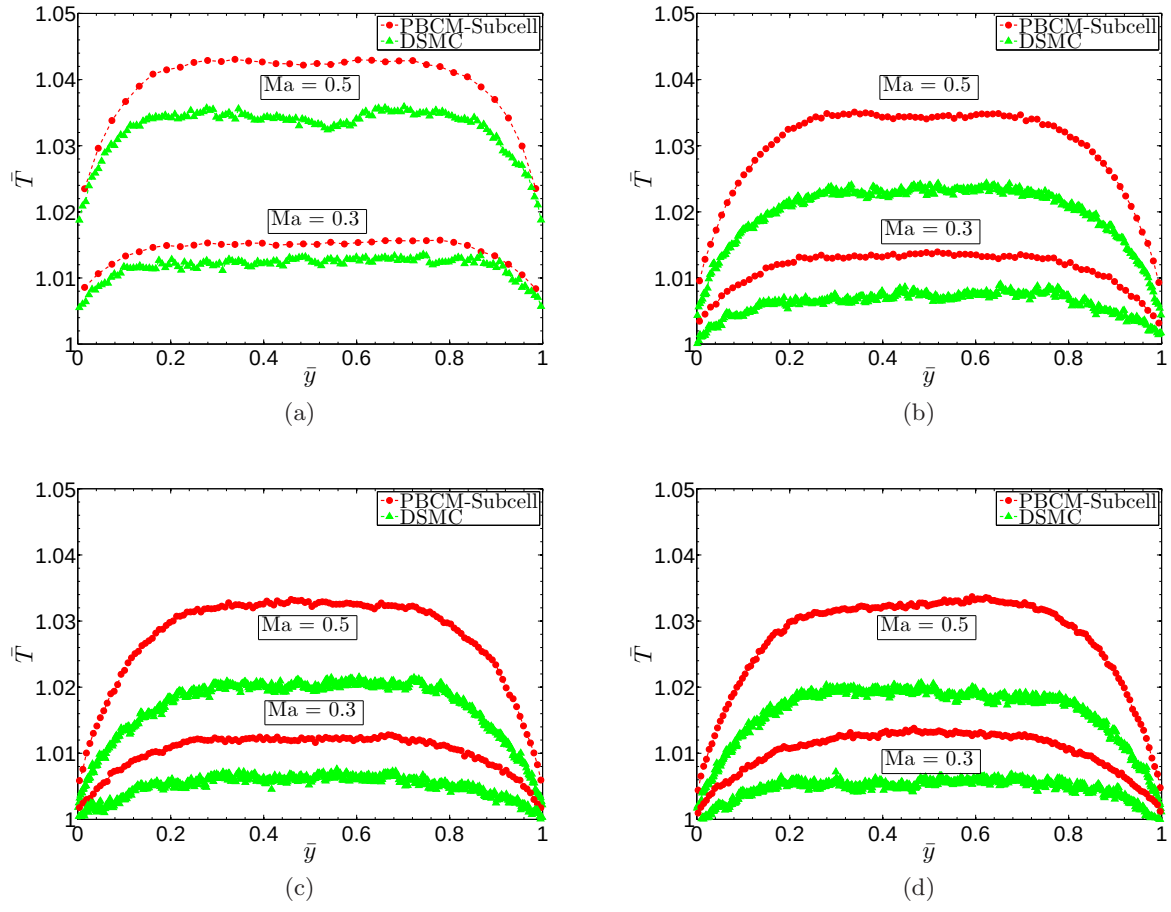

Figure 4.7: *Gravity driven flow temperature profiles at different Knudsen numbers (a)* Kn = 0.05 *(b)* Kn = 0.02 *(c)* Kn = 0.0125 *(c)* Kn = 0.01.

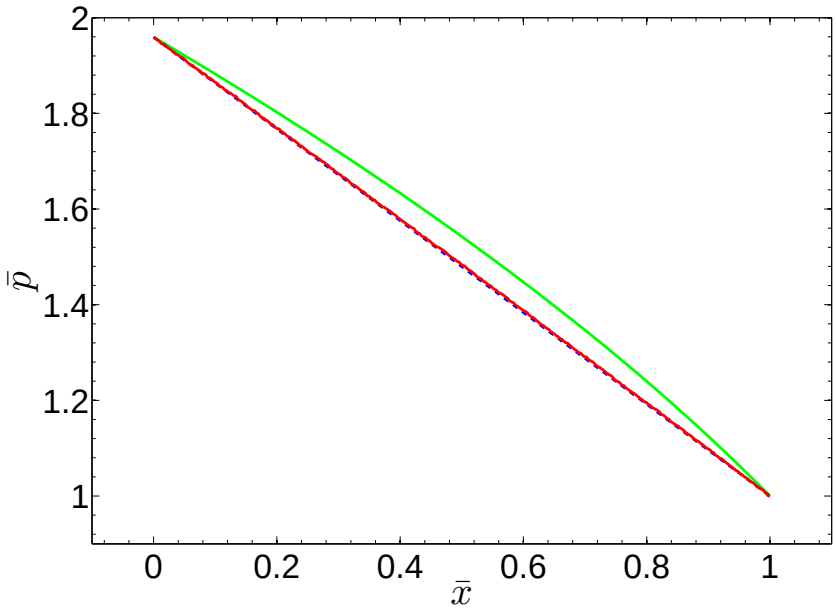

Figure 4.8: *Plot of pressure with distance along the channel measured from the inlet. Pressure is non-dimensionalized with the exit pressure whereas length down the channel is non-dimensionalized with respect to channel length. The simulation data is plotted in red dots, the analytical curve and the linear pressure distribution curve are shown by the green solid line, and the blue dashed line, respectively.*

In the pressure driven flow set-up, we have compared the centre line pressure profile obtained from simulation with the analytical result presented in Arkilic *et al.* (1997). In the pressure driven flows presented here, length to height ratio of the channel is 20; and a pressure ratio $\mathscr{P} = 2$ is maintained for driving the flow. In Fig.(4.8), pressure ($\bar{p}(x)$) is plotted with distance ($\bar{x}$) measured from the the inlet. The pressure has been non-dimensionalized with respect to the exit pressure and the distance is non-dimensionalized with the channel length. In this figure, we observe that the measured pressure profile is almost linear. This suggests that compressibility effects are not captured appropriately in the PBCM-Subcell simulation. Here, we remind that similar trend for centre line pressure was obtained from the standard MPCD simulations. Thus, further investigations are required in which Re and Ma are set properly corresponding to a microflow (see Chapter 3).

4.7 Outlook

A new collision model (pseudo binary collision model) is proposed in order to remove the restriction in the standard MPCD simulations with smaller δt, which is caused by the building up of velocity correlations among the particles. Here, it is shown that the new collisional model, same as the MPCD multiparticle collisions, conserves mass, moment, and energy and the local equilibrium distribution is same as the Maxwell-Boltzmann distribution. Further, different microflow set-ups are used to benchmark the kinetic nature of the algorithm, and we find that MPCD with the new collision model behaves very similar to standard MPCD. Here, we also show by measuring viscosity for different δt, in a gravity driven case, that the system behaviour

remains consistent for small δt, where for standard MPCD anomalous viscosity prediction can be observed. This in turn suggests that the building up of velocity correlations in not as severely restricted by δt in this new collision model as in standard MPCD.

Chapter 5

Non-ideal Equation of State for Particle Algorithms

5.1 Introduction

Even though most of the applications of MPCD is for modeling solvent dynamics in complex fluids, the equation of state of an MPCD fluid is that of an ideal gas (Gompper *et al.* 2008). Modeling liquid state via an ideal gas equation of state is unsatisfactory not only from physical but also from numerical point of view. Numerical disadvantages are due to the fact that for the same flow velocity and temperature, the Mach number is smaller in case of a non-ideal equation of state due to increased value of the speed of sound. Thus, having non-ideal equation of state should allow one to reduce undesirable compressible effects in the method. Physically, one would also like to model non-ideal equation of state in MPCD framework so that phase transitions such as vapour-liquid transition can be modeled with this method. It should be reminded here that unlike MPCD other mesoscale methods such as LBM (Shan & Chen 1993, 1994; He & Doolen 2002; Kikkinides *et al.* 2008; Suryanarayanan *et al.* 2013), and DPD (Liu *et al.* 2006) do manage to mimic this phenomena.

Very few works have attempted to model non-ideal equation of state in MPCD framework. One of the most successful work in this regard is Ref. Ihle *et al.* (2006), where a biased multiparticle collision for modeling excluded volume effect, in a thermodynamically consistent manner, is presented. It has been shown that a consistent non-ideal pressure, which is linear in temperature and quadratic in local density contribution, can be obtained via this model (Ihle *et al.* 2006). In addition, this contribution is inversely dependent on the time step, and for smaller values significantly large contribution to non-ideal pressure can be obtained. However, to the best of our knowledge this model is not widely used and so far remains qualitative at best.

In this thesis, an alternate framework for incorporating excluded volume effect in MPCD systems is presented. This framework is based on kinetic model of Ansumali (Ansumali 2011), where excluded volume effect is modeled as mean field shift in the trajectory of a particle during the free propagation step. An attractive feature of the model is that it can be easily incorporated in a particle based algorithm such as MPCD. The effectiveness of this approach is investigated by evaluating a few thermodynamic properties and transport coefficients. Further, we extend the model by adding the effect of long range attractive forces between molecules as Vlasov type force (He & Doolen 2002; Liboff 1983). Finally, we present liquid-gas coexistence curve using this model.

This chapter is organized as follows: in section 5.2, Van der Waals and Carnahan-Starling equations of state are presented. A phenomenological mean field model for including excluded volume effect is reviewed in section 5.3, and in section 5.4 a systematic approach for modeling long range attraction between molecules is elucidated which appears as a Vlasov type force in the system. Numerical implementation of the dense gas model is presented in section 5.5 and a few studies, such as changes in pressure, viscosity, and sound speed with density, are done in section 5.6 for the dense gas system. Finally, in section 5.7 condensation of a gas into liquid is studied by including the effect of molecular attraction into the system.

5.2 Equation of State for a Non-ideal Fluid

If the gas is dilute, the total volume occupied by particles (note that terms *particle* and *molecule* are used in the same sense) is negligible. In such a scenario, ideal gas is a good approximation, which gives the equation of state in terms of pressure p^{ID} and temperature T as:

$$p^{\mathrm{ID}}V = Nk_{\mathrm{B}}T, \tag{5.1}$$

where k_{B} is the Boltzmann constant, V is the volume of the container and N is the number of gas molecules. A more fundamental representation of this equation of state is given in terms of internal energy (e) and entropy (s^{ID}) of the system (per unit volume) as (Callen (2006)):

$$s^{\mathrm{ID}} = \rho R \ln\left[\frac{V}{N}\left(\frac{2\pi m k_{\mathrm{B}}T}{h^2}\right)^{3/2}\right] + \frac{5}{2}\rho R, \tag{5.2}$$

where the mass density $\rho = Nm/V$ and $R = k_{\mathrm{B}}/m$ is the specific gas constant.

Van der Waals argued that the volume of the container may not correspond to the free volume when the gas is not dilute, i.e. a considerable portion of the container volume V is excluded due to the presence of other gas molecules. In order to quantify excluded volume, he argued that any given molecule with diameter σ hinders the free volume by $4\pi\sigma^3/3$ (see Fig.(5.1a)). Since this volume is shared between two molecules, per molecule contribution to excluded volume is $b = 2\pi\sigma^3/3$. Thus for N particles, total excluded volume is $N2\pi\sigma^3/3$, and the equation of state for hard-sphere with volume correction due to finite size of the gas molecules in terms of pressure p^{h} is

$$p^{\mathrm{h}}(V - Nb) = Nk_{\mathrm{B}}T. \tag{5.3}$$

This equation of state also implies that entropy (per unit volume) of the hard-sphere should be

$$s = s^{\mathrm{ID}} + \rho R \ln\left(1 - b'\rho\right), \tag{5.4}$$

where $b' = b/m$, m is the mass of a molecule.

For hard-sphere systems, a quantitatively accurate model was provided by Carnahan and Starling (CS) (Carnahan & Starling 1969) as

$$p^{\mathrm{h}} = \rho RT\left(1 + \frac{y(4-2y)}{(1-y)^3}\right), \tag{5.5}$$

where reduced density $y = \rho b/4$, and Pade-approximation to the original virial series was used to arrive at this expression. Such departures from ideal gas behavior is often quantified in terms of compressibility factor χ defined as

$$\chi = \frac{p}{\rho RT} - 1 \equiv \frac{1}{\rho R}\left(s - \rho\frac{\partial s}{\partial \rho}\right). \tag{5.6}$$

Thus, corresponding to Van der Waals' equation of state of hard-sphere, we get χ as

$$\chi^{\mathrm{VDW}} = \frac{\rho b'}{(1-\rho b')}, \tag{5.7}$$

while for Carnahan-Starling equation of state of hard-sphere it is:

$$\chi^{\mathrm{CS}} = \frac{y(4-2y)}{(1-y)^3}. \tag{5.8}$$

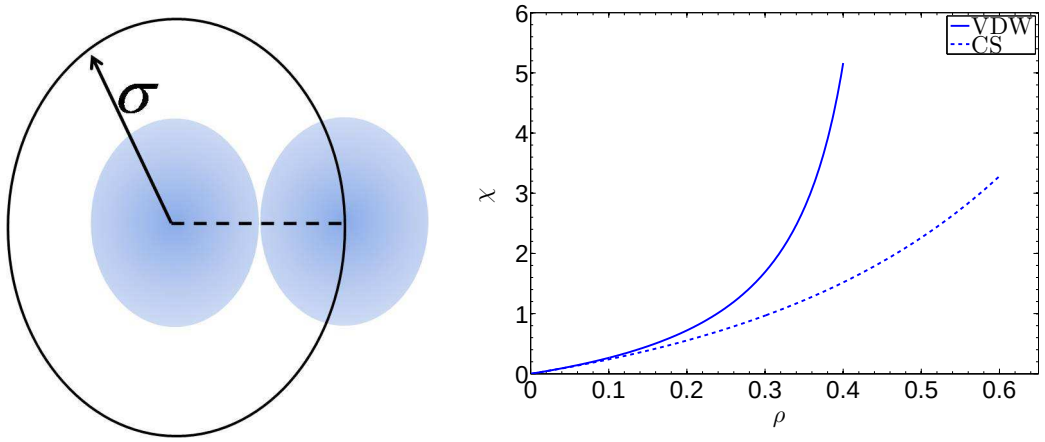

(a) (b)

Figure 5.1: *(a) Depicting excluded volume; per-particle contribution is* $2\pi\sigma^3/3$. *(b) Plot of* χ^{VDW} *and* χ^{CS} *as a function of density* (ρ).

In Fig.(5.1b), hard-sphere compressibility factor is plotted for Carnahan-Starling and Van der Walls equations of state. It can be seen that for small departures from ideality, both are identical, but they are quite different at high densities. A direct comparison with molecular dynamics data suggest that CS equation of state is practically indistinguishable from the predictions of molecular dynamics simulations for $y < 0.5$ (see Carnahan & Starling (1969)).

Van der Waals also included the effect of attractive forces in the system by arguing that the role of attractive part is to reduce the pressure, and the correction should be quadratic in density. Essential argument is that each particle experiences an attractive force proportional to the number density of the gas molecules, (N/V), and the number of particles interacting with a surface is again proportional to the local number density. Thus, due to presence of N particles in a volume V total reduction in the pressure should be $\tilde{a}(N/V)^2$, or equivalently $a'\rho^2$, where $\tilde{a}$ is a measure of the strength of attractive force between gas molecules and $a' = \tilde{a}/m^2$. Thus the

pressure is given by

$$p = \frac{\rho RT}{(1 - b'\rho)} - a'\rho^2. \tag{5.9}$$

It should be noted that the Van der Waals equation of state is one of the simplest model which is capable of predicting phase separation. From Fig.(5.2a), it is evident that, similar to an ideal gas law, Van der Waals equation for hard-sphere predicts a monotonic dependence of pressure on specific volume, $v = 1/\rho$. However, a phase change can be observed when contribution due to long range attractive forces between molecules is also included. It is apparent from Fig.(5.2b) that $p-v$ isotherm becomes unstable for a range of v (in Fig.(5.2b) line OPQ), and in this region both phases co-exist together. The line OPQ is selected such that the area OBPO is equal to the area PQCP. This equal area construction is called Maxwell construction.

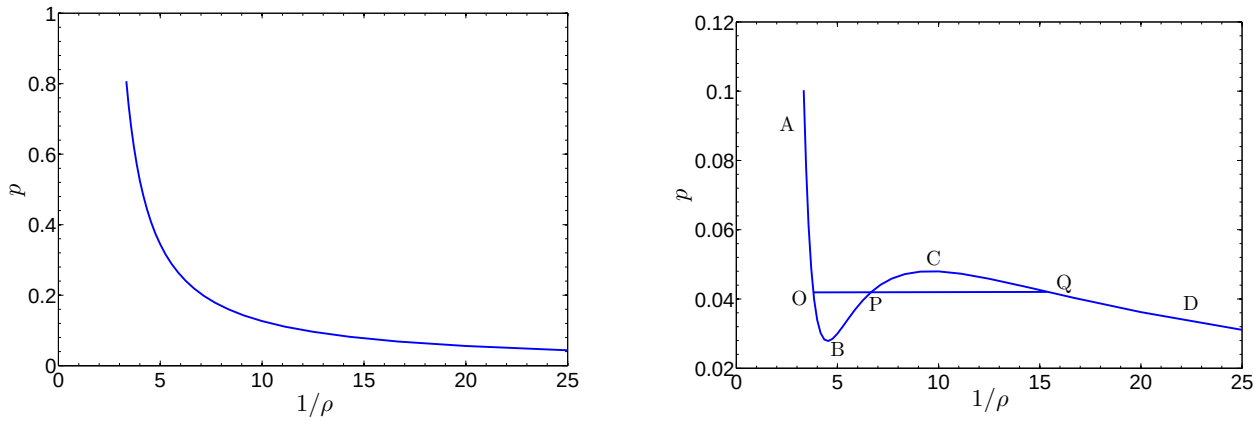

(a) (b)

Figure 5.2: *Plot of pressure with volume for the Van der Waals equation of state. (a) correction due to the volume effect of the molecules is considered, Eq.(5.9). (b) both volume effects and long range attractive forces between molecules are considered,* $p = \frac{\rho RT}{(1-\rho b')} - a'\rho^2$

The phenomena of phase separation is observed only below a critical point in the $p - v$ diagram, which is defined as the point on a given isotherm where the first and second derivatives of pressure with respect to density vanish. For the Van der Waals equation of state, properties (p_c, T_c, ρ_c) at the critical point are

$$\rho_c = \frac{1}{3b'}, \quad p_c = \frac{a'}{27b'^2}, \quad T_c = \frac{8a'}{27Rb'}. \tag{5.10}$$

Finally, the free energy per molecule, in non-dimensional unit, can be written as:

$$f = f_{\mathrm{ID}} - \rho RT \ln\left(1 - b'\rho\right) - a'\rho^2, \tag{5.11}$$

where

$$f_{\mathrm{ID}} = -\rho RT \ln\left[\frac{V}{N}\left(\frac{2\pi mT}{h^2}\right)^{3/2}\right] - \rho RT \tag{5.12}$$

The critical value of the ratio $(p_c/(\rho_c RT_c)$ obtained by Van der Waals equation of state is

0.375, while that obtained in experiments are in the range $0.28 - 0.33$. The equation of state can be made more accurate by using Carnahan and Starling model for the repulsive part. This modified model suggests that the pressure expression is:

$$p = \rho RT \left(1 + \frac{y(4-2y)}{(1-y)^3}\right) - a'\rho^2. \tag{5.13}$$

The critical properties for the Carnahan-Starling equation of state is given by

$$\rho_c = \frac{0.52170}{b}, \quad p_c = \frac{0.07066a'}{b^2}, \quad T_c = \frac{0.37733a'}{bR}. \tag{5.14}$$

5.2.1 Sound Speed

As discussed in the introduction, an important thermodynamic quantity from fluid dynamics point of view is the speed of sound. The sound propagation process is adiabatic and the sound speed can be calculated using the thermodynamic relation $c_s^2 = (\partial p/\partial \rho)_s$, where the partial differential of pressure (p) with density (ρ) is calculated for an isentropic process. Equivalently, the speed of sound can be calculated using following expression:

$$c_s^2 = \left(\frac{\partial p}{\partial \rho}\right)_T + \frac{T}{\rho^2 C_v}\left(\frac{\partial p}{\partial T}\right)_\rho^2, \tag{5.15}$$

where T is temperature, $C_v = 3R/2$ is specific heat capacity at constant volume. Thus, for Van der Waals' equation of state (Eq.(5.9)) speed of sound is:

$$c_s^{\mathrm{VDW}} = \sqrt{\frac{5}{3}RT}\left(\sqrt{\frac{1}{(1-\rho b)^2} - \frac{6}{5}\frac{a}{RT}\rho}\right), \tag{5.16}$$

and similarly for Carnahan and Starling equation of state, speed of sound is:

$$c_s^{\mathrm{CS}} = \sqrt{\frac{5}{3}RT}\left(\sqrt{1 + \frac{3}{5}\left[\frac{8y-2y^2}{(1-y)^4} + \frac{2}{3}\left\{\frac{8y-4y^2}{(1-y)^3} + \frac{16y^2-16y^3+4y^4}{(1-y)^6}\right\}\right] - \frac{6}{5}\frac{a}{RT}\rho}\right). \tag{5.17}$$

These expressions will be used in subsequent sections to evaluate effectiveness of the numerical implementations.

5.3 Mean Field Model for Non-ideality due to Molecular Replusion

Enskog kinetic model was the first successful model of molecular repulsion in the context of kinetic theory (Chapman *et al.* 1970). In this description, one starts with Van der Waals' picture where molecular repulsion is modeled as finite size of the molecule. Enskog suggested that finite size of the molecules should reflect as non-local collisions in the Boltzmann kinetic theory. This theory was later refined by van Beijeren and Ernst (known as the revised Enskog theory (RET)) (Van Beijeren & Ernst 1973). The revised Enskog theory is quite successful in describing corrections to the viscosity due to non-ideality and provides the basic framework for

modeling non-ideal gas effect in kinetic theory (Chapman *et al.* 1970; McQuarrie 1976). However, very limited success has been achieved in successful extensions of particle based simulation tool such as DSMC for Enskog equation (Alexander *et al.* 1995). The non-local collision is difficult to handle both for methods such as DSMC as well as for kinetic modeling via simplified phenomenological theories of BGK type (Alexander *et al.* 1995; Ansumali 2011).

Recently, a new framework for incorporating non-ideal effects due to repulsion in kinetic equations has been developed in Ref. Ansumali (2011). In this section, we briefly review this approach of introducing non-ideal equation of state. The key new idea in this work was that molecular repulsion need not be modeled via non-local collisions only. A simple way to build excluded volume is to change the free propagation step by introducing mean field shift in the trajectory of a particle reflecting molecular repulsion. This work suggested that in streaming step, which happens in mean free time τ_s, the shift in trajectory $\Delta x_{i\alpha}$ for ith molecule with velocity $v_{i\alpha}$ should be

$$\Delta x_{i\alpha} = v_{i\alpha}\tau_s + \tau_s\chi(\rho)(v_{i\alpha} - u_\alpha) \equiv \tau_s \hat{v}_\alpha, \tag{5.18}$$

with $\chi(\rho)$ being compressibility factor and is expected to be a positive quantity which is a monotonically increasing function of the density. In the above equation $\hat{v}_\alpha$ is the modified streaming velocity. Following form has been suggested for $\hat{v}_\alpha$ (Ansumali 2011):

$$\hat{v}_\alpha = v_\alpha + \chi(\rho)(v_\alpha - u_\alpha), \tag{5.19}$$

where u_α is the local bulk velocity.

The physical rationale behind this model can be understood by considering the motion of a tagged particle. According to Eq.(5.19), when a tagged particle is moving faster than the local average velocity, it gets more displacement. Thus, the tagged particle can avoid joining the locally dense region. Conversely, if a particle in moving slower than the local velocity its speed reduces and thus cluster formation is avoided once again. Thus, on an average, this modification captures the effect of strong repulsive cores of molecules which does not allow them to come very close to each other, or to form a cluster.

This change in free propagation step leads to change into evolution equation for one particle distribution function $f(\mathbf{x}, \mathbf{v}, t)$ as

$$\partial_t f(\mathbf{z}, t) + \partial_\alpha \left[\hat{v}_\alpha f(\mathbf{z}, t)\right] = \mathscr{C}, \tag{5.20}$$

where $\mathscr{C}$ is the appropriate collision operator (for example Boltzmann collision operator or BGK) which conserves mass, momentum, and energy.

It is evident that, similar to Boltzmann equation, this modified equation also leads to evolution equations for density (ρ), momentum density (j_α), and energy density (E) in the conservation form:

$$\begin{aligned} \partial_t \rho + \partial_\alpha j_\alpha &= 0, \\ \partial_t j_\gamma + \partial_\alpha(u_\alpha u_\gamma + p\delta_{\alpha\gamma} + \sigma_{\alpha\gamma}) &= 0, \\ \partial_t E + \partial_\alpha\left((E+p)u_\alpha + \sigma_{\alpha\gamma}u_\gamma + q_\alpha\right) &= 0, \end{aligned} \tag{5.21}$$

where pressure is that of a real gas, $p = (1+\chi)\rho k_{\mathrm{B}}T/m$, and the shear stress, and heat flux are:

$$\sigma_{\alpha\gamma} = (1+\chi)\sigma^K_{\alpha\gamma}, \quad q_\alpha = (1+\chi)q^K_\alpha. \tag{5.22}$$

Here $\sigma^K_{\alpha\gamma}$, and q^K_α are kinetic part of the stress tensor, and heat flux, respectively. These quantities are defined in terms of peculiar velocity $\xi_\alpha = v_\alpha - u_\alpha$ as:

$$\sigma^K_{\alpha\gamma} = \int d\xi f \xi_\alpha \xi_\beta, \quad q^K_\alpha = \int d\xi f \xi_\alpha \frac{\xi^2}{2}. \tag{5.23}$$

Thus, we see that the conservation laws are consistent with dense gas models such as Enskog equation. Furthermore, The H-function for this model is:

$$H = \underbrace{\int f\,(\ln f - 1)}_{H^{\mathrm{ID}}} - \frac{s(\rho)}{k_{\mathrm{B}}} \tag{5.24}$$

It can be noted that the non-ideal part of entropy is a function of density only. Also, from continuity equation, we get

$$\partial_t\left(\frac{s}{R}\right) + \frac{1}{R}\frac{\partial s}{\partial \rho}\partial_\alpha j_\alpha = 0. \tag{5.25}$$

The evolution equation for H can be obtained by multiplying Eq.(5.20) with $\ln f - 1$ and integrating with respect to $\mathbf{v}$, this results

$$\partial_t H^{\mathrm{ID}} + \partial_\alpha \int [\hat{v}_\alpha f(\ln f - 1)]d\mathbf{v} - \underbrace{\int \hat{v}_\alpha f \partial_\alpha \ln f d\mathbf{v}}_{\mathscr{I}} = \int \mathscr{C} \ln f d\mathbf{v}, \tag{5.26}$$

where the right hand side in the above equation gets simplified because $\int \mathscr{C} d\mathbf{v} = 0$. In the above equation the integral $\mathscr{I}$ can be further simplified to

$$\mathscr{I} = \int v_\alpha f \partial_\alpha \ln f d\mathbf{v} + \int \chi(v_\alpha - u_\alpha) f \partial_\alpha \ln f d\mathbf{v}. \tag{5.27}$$

The second term on the right hand side of the above equation can be integrated in $\mathbf{v}$, and by using Eqs. (5.6) the integral $\mathscr{I}$ becomes

$$\mathscr{I} = \int v_\alpha \partial_\alpha f d\mathbf{v} - \partial_\alpha\left(\frac{s}{R}u_\alpha\right) + \frac{1}{R}\frac{\partial s}{\partial \rho}\partial_\alpha j_\alpha. \tag{5.28}$$

Substituting for $\mathscr{I}$ from above equation into Eq.(5.26), and using Eq.(5.25), we get following evolution equation for H:

$$\partial_t H + \partial_\alpha j^H_\alpha = \int \mathscr{C} \ln f d\mathbf{v}, \tag{5.29}$$

where

$$j^H_\alpha = -(s u_\alpha/R) + \int \hat{v}_\alpha f(\ln f - 1)d\mathbf{v}. \tag{5.30}$$

From this equation it becomes obvious that only flux term gets affected due to the modified streaming velocity, and there is no extra source term for non-ideal entropy. This feature that non-ideality due to repulsion does not change entropy production is consistent with Enskog

equation (Van Beijeren & Ernst 1973).

As expected from a model of repulsive core, current model does not change entropy production but only changes the entropy flux. Thus, the equilibrium distribution remains as Maxwell-Boltzmann distribution because collision term is same as that of Boltzmann.

5.4 Multiphase System: Vlasov Model

In the previous section, current approach for incorporating repulsive part of the potential, a mean field theory for dense gases, was described. In this section, an extension of the dense gas model (Ansumali 2011) for multiphase flow is presented by adding attractive part of the molecular potential. Here, it should be reminded that for simulating phase separation problem, one needs to capture both the effects due to short range repulsion as well as long range attraction between molecules (see section 5.2).

Following Ref. He & Doolen (2002), the attractive part of the potential is added as mean Vlasov force. The final kinetic model, which includes both effects that of repulsive core and of long range attractive force between particles, is:

$$\partial_t f + \partial_\alpha \left[\hat{v}_\alpha f\right] - \boldsymbol{\Delta} V_m \cdot \boldsymbol{\Delta}_{\mathbf{v}_1} f = \mathscr{C}, \tag{5.31}$$

where V_m is defined in terms of local density as:

$$V_m = -2a\rho - \kappa \boldsymbol{\Delta}^2 \rho \tag{5.32}$$

with a and κ defined in terms of attractive part of intermolecular potential $V(\mathbf{r})$ as:

$$a = -\frac{1}{2}\int_{r>\sigma} V(\mathbf{r}) d\mathbf{r}, \quad \kappa = -\frac{1}{6}\int_{r>\sigma} r^2 V(\mathbf{r}) d\mathbf{r}. \tag{5.33}$$

As for example a and κ value for attractive part of Lennard-Jones molecular potential ($V(\mathbf{r}) = -4\pi\epsilon(\sigma/r)^6)$) is (Kikkinides *et al.* 2008):

$$a = \frac{8\pi\sigma^3\epsilon}{3}, \quad \kappa = \frac{8\pi\sigma^5\epsilon}{3}, \tag{5.34}$$

This relationship suggest that for Lennard-Jones molecular potential

$$\kappa = a\,\sigma^2. \tag{5.35}$$

However, in general one may expect $\kappa = a'\sigma^2\hat{\kappa}$, where κ is a constant of order 1.

In Ref. He & Doolen (2002), modeling attractive term as Vlasov force was motivated using BBGKY hierarchy. For detailed derivation, we refer the readers to He & Doolen (2002). A qualitative understanding of the current approach can be achieved by writing the conservation

laws based on Eq.((5.31)), they are

$$\begin{aligned}
\partial_t \rho + \partial_\alpha j_\alpha &= 0, \\
\partial_t j_\gamma + \partial_\alpha (u_\alpha u_\gamma + p\delta_{\alpha\gamma} + \sigma_{\alpha\gamma}) + \partial_\alpha \underbrace{(\kappa \partial_\gamma \rho \partial_\alpha \rho)}_{VdW-Stress} &= 0, \\
\partial_t E + \partial_\alpha \left((E+p)u_\alpha + \sigma_{\alpha\gamma}u_\gamma + q_\alpha\right) - \left[a\rho^2 + \kappa\left(\rho\partial_\alpha^2\rho + \frac{1}{2}(\partial_\alpha\rho)^2\right)\right]\partial_\alpha u_\alpha + u_\gamma \partial_\alpha\left(\kappa\partial_\gamma\rho\partial_\alpha\rho\right) &= 0,
\end{aligned} \tag{5.36}$$

where the thermodynamic pressure of the system is:

$$p = \rho RT(1+\chi(\rho)) - a\rho^2 - \kappa\left(\rho\partial_\alpha^2\rho + \frac{1}{2}(\partial_\alpha\rho)^2\right), \tag{5.37}$$

which has the usual local Van der Waals type term and other than that an interfacial stress term needed to model phase transition (Suryanarayanan *et al.* 2013).

Thus, we see that in order to model multiphase flows with particle based methods, we can add attractive part as Vlasov's type force and repulsive part as shift in position during the free propagation step.

5.5 Particle Based Method for Non-ideal Equation of State

An attractive feature of the model proposed by Ansumali (Ansumali 2011) is that it can be easily implemented in any particle based simulation tool. Similarly, attractive part, which is represented as Vlasov type force, can be treated like acceleration term in particle simulations. As for example, numerical implementation of this model of dense gas in the context of original MPCD, or with pseudo-binary collision model is quite trivial. In particular, when there is an external force acting on the system, we use Verlet scheme (Rapaport 2004) for updating velocity and position. The streaming step changes to

$$\begin{aligned}
v_\alpha\left(t+\frac{\delta t}{2}\right) &= v_\alpha\left(t-\frac{\delta t}{2}\right) + a_\alpha\left(t+\frac{\delta t}{2}\right)\delta t + \Omega(t), \\
\tilde{v}_\alpha\left(t+\frac{\delta t}{2}\right) &= v_\alpha\left(t+\frac{\delta t}{2}\right) + \chi\left[v_\alpha\left(t+\frac{\delta t}{2}\right) - u_\alpha\left(t+\frac{\delta t}{2}\right)\right], \\
x_\alpha(t+\delta t) &= x_\alpha(t) + \tilde{v}_\alpha\left(t+\frac{\delta t}{2}\right)\delta t.
\end{aligned} \tag{5.38}$$

where a_α is the acceleration of a particle under the influence of external forces. It is apparent that numerically implementing the dense gas model requires only few changes in the streaming part of the code and rest of the code remain unchanged.

5.6 Verification of the Model

In this section, a few results related to the mean field model for dense gases are presented. Firstly, a homogeneous system with the mean field dense gas model is investigated for the changes in the observed pressure with density. This numerical evaluation of the pressure is done

to ensure that the non-ideality in equation of state is correctly implemented by the new scheme. Secondly, sound speed is numerically evaluated as a function of density for a given equation of state. Furthermore, viscosity as a function of density is evaluated to contrast with the theoretical prediction that the kinetic part of viscosity gets a factor $(1+\chi)^2$ (Ansumali 2011). Finally, phase diagram for a single component two phase system is reconstructed, numerically, to ensure that Maxwell construction (Callen 2006) is properly captured in the new framework.

5.6.1 Pressure in Homogenous System

As the first test, pressure values in a homogeneous system is contrasted with the expected theoretical values. Numerical simulations were set-up by considering $10 \times 10 \times 10$ number of boxes and periodic boundary condition in all three directions. In case of PBCM, average number of particles per collision cell was set to 80 (10 particle per subcell), the rotation angle used was 85^0, and as equation of state the Carnahan-Starling equation of state (Eq.(5.8)) was chosen. In order to show that the dense model works for all particle methods, provided the collision operator conserves mass, momentum, and energy; we have also run same set of simulations with standard MPCD.

Numerically, pressure was calculated by measuring the flux of normal momentum across a given surface (Chapman *et al.* (1970)). In Fig.(5.3), pressures as a function of density using MPCD and PBCM simulations are plotted, and contrasted with the Carnahan-Starling equation of state. This plot shows that both collision models show good agreement with the theoretical pressure profile. As mentioned before, this suggests that the working of the mean field model for dense gases is not dependent on collision operator as long as it conserves mass, momentum, and energy.

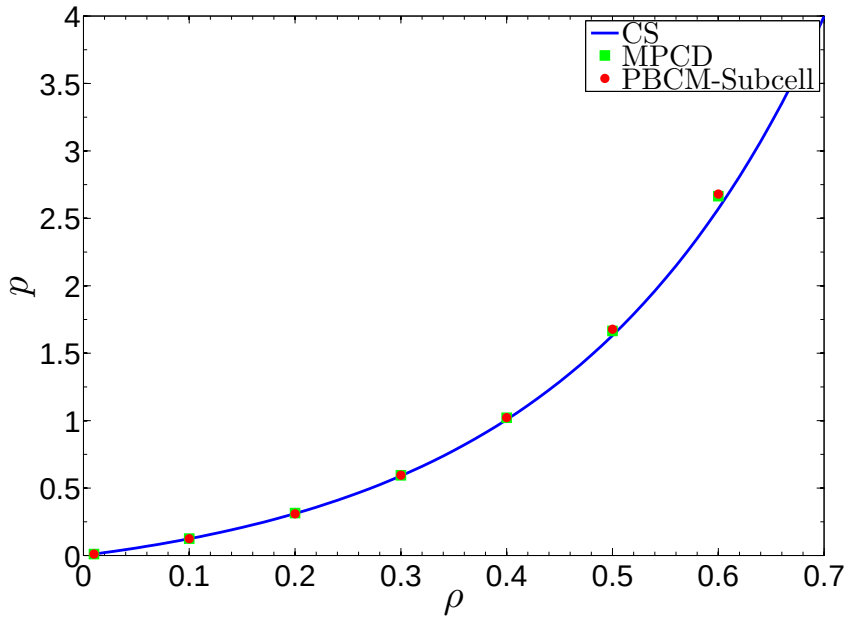

Figure 5.3: *Plot of pressure with density (ρ). In this figure pressure obtained from MPCD and PBCM-Subcell simulations are compared with the theoratical plot obtained via Carnahan-Starling equation of state. We have set temperature, $T = 1$.*

5.6.2 Sound Speed

Once the non-ideality in the equation of state is implemented, the speed of sound should also change. In section 5.2, sound-speeds corresponding to different equations of state were provided. In this section, speed of sound as a function of density is computed numerically, and contrasted with the analytical expression. For simplicity, we work with the Van der Waals equation of state.

In order to numerically compute speed of sound, a particle based simulation technique developed in Ref. (Hadjiconstantinou & Garcia 2001) is used. In this approach, as shown in Fig.(5.4), an air column of length L which is closed at one end with specularly reflecting wall is employed for generating a confined wave. The other end of the column, $x = 0$, is attached to a reservoir in which velocity of the fluid is excited sinusoidally as, $v = v_0 \sin(\omega t)$, where ω is angular frequency. As a result of periodically varying velocity in the reservoir a sound wave propagates into the column (v_{in}). This wave after reaching the other end of the channel ($x = L$), gets totally reflected by the wall, and travels back (v_{ref}). At any instance, the net velocity disturbance in the air column is sum of the velocity disturbances created by the two propagating waves, and is given by

$$\begin{aligned} v(x,t) &= v_1 \left[e^{-\tilde{m}x} \cos(kx) - e^{-\tilde{m}(2L-x)} \cos(k(x-2L)) \right] \sin(\omega t) \\ &\quad - v_1 \left[e^{-\tilde{m}x} \sin(kx) + e^{-\tilde{m}(2L-x)} \sin(k(x-2L)) \right] \cos(\omega t) \\ &= A(x) \sin(\omega t) + B(x) \cos(\omega t), \end{aligned} \tag{5.39}$$

where $\tilde{m}$ is attenuation coefficient, and k is wave number. In deriving Eq.(5.39), we have used following forms for v_{in} and v_{ref} (Landau & Lifshitz 2013):

$$v_{in} = v_1 e^{-\tilde{m}x} \sin(\omega t - kx), \tag{5.40}$$

$$v_{ref} = v_1 e^{-\tilde{m}(2L-x)} \sin(\omega t + k(x-2L) + \pi) \tag{5.41}$$

We also note that v_1 is used as the amplitude for the disturbances v_{in} and v_{ref}, and is different from v_0. This is done because only a part of the wave from the reservoir gets transmitted into the column, and it's amplitude is represented as v_1 here. In general we expect that $v_1 \approx v_0/2$. Furthermore, The parameters ω and k are related to the sound speed, $c_s = \omega/k$.

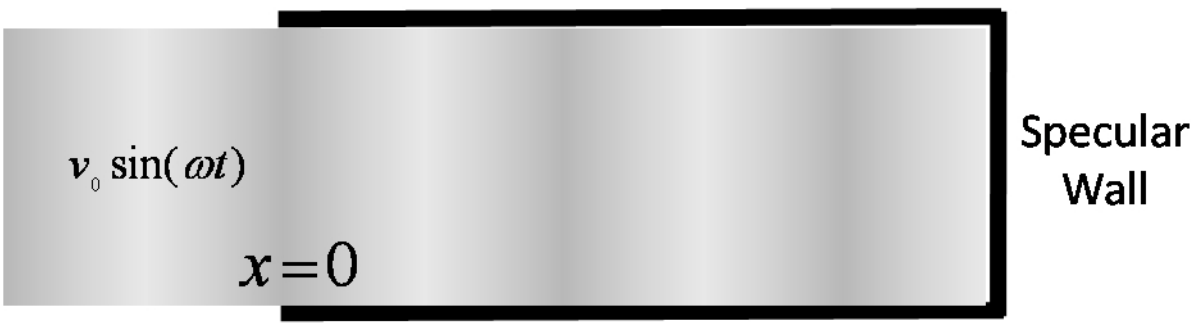

Figure 5.4: *Schematic diagram of the air column used to measure the speed of sound.*

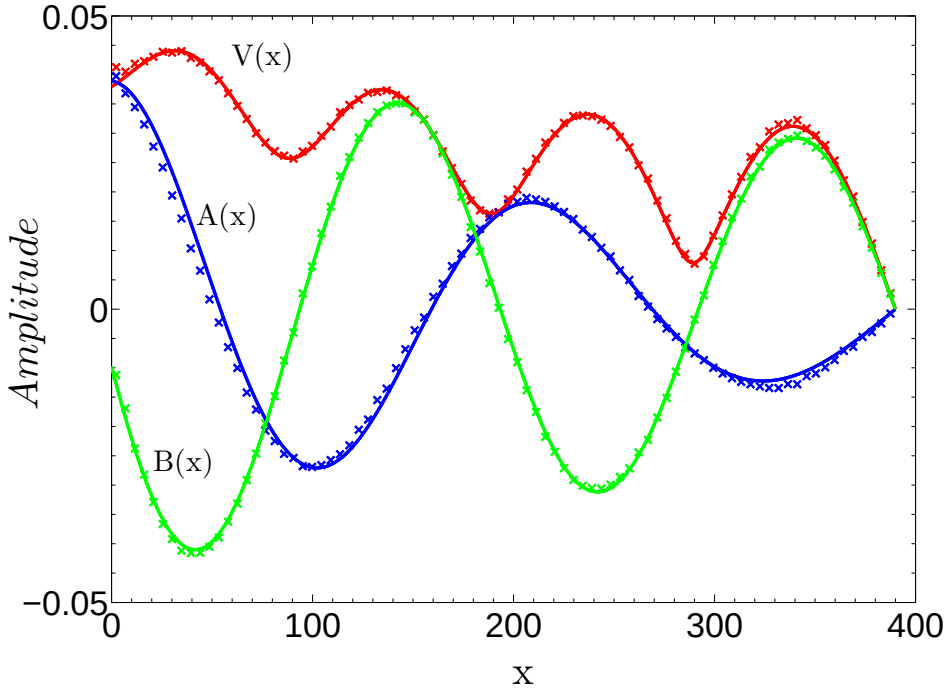

Figure 5.5: *Showing data fit to A(x), B(x), and V(x). In cross (×) the chi-square fit data is shown and in solid line (-) non-linear curve fits are shown. The data presented here corresponds to the case with* $\rho = 0.1$

Using the setup described above it is possible to compute speed of sound in a medium occupying the air column. Sound speeds are calculated at densities, $\rho = 0.01, 0.05, 0.1, 0.15$, and 0.2. In numerical simulations, $\omega = 0.05$, and the corresponding time period, $t_{rp} = 125.6$. We note that in these simulations, it is desirable to have t_{rp} much grater than the stream time δt. We have taken $\tau = 0.2$, and the largest stream time corresponds to the lowest density, $\rho = 0.01$, which is $\delta t = 4.0$. It is clear that in all the simulations $t_{rp}/\delta t > 30$; it insures that time variations in the velocity field is captured appropriately in the simulations. Also, Reynolds numbers based on the sound speed, $\mathrm{Re} = \rho c^2/(\eta\omega)$, range from 6 to 20. In order to minimize the effect of non-linearity in the flow, it is desired that $v_0 \ll c_s/\mathrm{Re}$. In simulations, $v_0 = 0.05c_s$, is set which in turn implies, $v_1 \approx 0.5v_0$. In addition, the length of the column is small enough so that the effect of non-linearity remains insignificant. In Ref. Hadjiconstantinou & Garcia (2001) these parameter settings are explained in more detail.

We start the simulation at $t = 0$ with fluid in the column at a temperature, $T = 1$, and zero mean velocity. After the initial transient dies out, we record the mean velocities at different points inside the air column at every time step. For sampling mean velocity, the column is divided into slices of equal thickness (subcell size) perpendicular to the x-axis and average velocity of the particles in these slices is computed and stored during each interval. The data is

recorded over N time cycles. The chi-square fit to this data results

$$A(x_j) = \frac{\sum c^2 \sum vs - \sum sc \sum vc}{\sum c^2 \sum s^2 - (\sum sc)^2}, \tag{5.42}$$

$$B(x_j) = \frac{\sum s^2 \sum vc - \sum sc \sum vs}{\sum c^2 \sum s^2 - (\sum sc)^2}, \tag{5.43}$$

where

$$\sum s^2 = \sum_i^N \sin^2(\omega t_i), \quad \sum c^2 = \sum_i^N \cos^2(\omega t_i), \tag{5.44}$$

$$\sum sc = \sum_i^N \sin(\omega t_i)\cos(\omega t_i), \quad \sum vs = \sum_i^N v(x_j, t_i)\sin(\omega t_i), \tag{5.45}$$

$$\sum vs = \sum_i^N v(x_j, t_i)\cos(\omega t_i). \tag{5.46}$$

Here x_j is the x-coordinate of the centre of j^{th} slice. The data extracted give the form of A(x), and B(x) at discrete points. Next, using non-linear curve fits through $A(x_j)$ and $B(x_j)$, the values of wave number (k) and attenuation coefficient (m) are extracted. Finally, sound speed is calculated using $c_s = \omega/k$. Note that we have also used velocity magnitude profile , $V(x) = \sqrt{A^2(x) + B^2(x)}$, for curve fitting. Typical curves for A(x), B(x), and V(x) obtained from a simulation are shown in Fig.(5.5). In Fig.(5.6), measured sound speeds are plotted with density. We observe that the numerical data show good agreement with the theory.

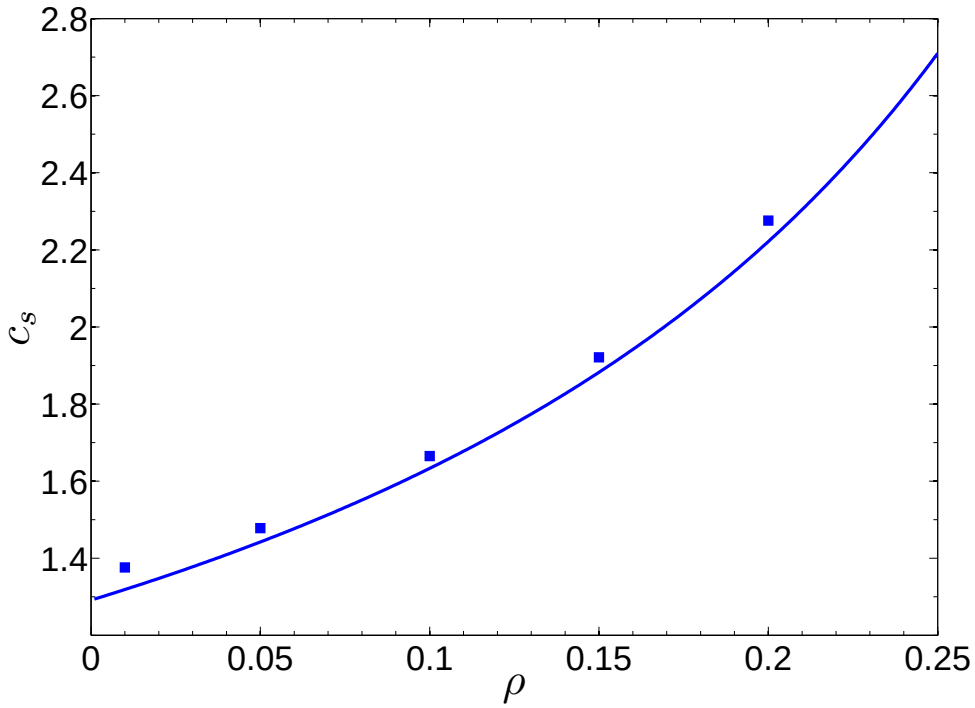

Figure 5.6: *Plot of sound speed with density for the Van der Waals equation of state.*

5.6.3 Viscosity of the Gas

In order to compute the viscosity of the modified system, we use the setup of Poiseuille flow. According to the dense gas model presented in section 5.3, we note that the viscosity of the modified system ($\eta^{(d)}$) should be $(1+\chi)^2$ times that of the original system (η). The same can be observed in numerical simulations (Fig.(5.7)).

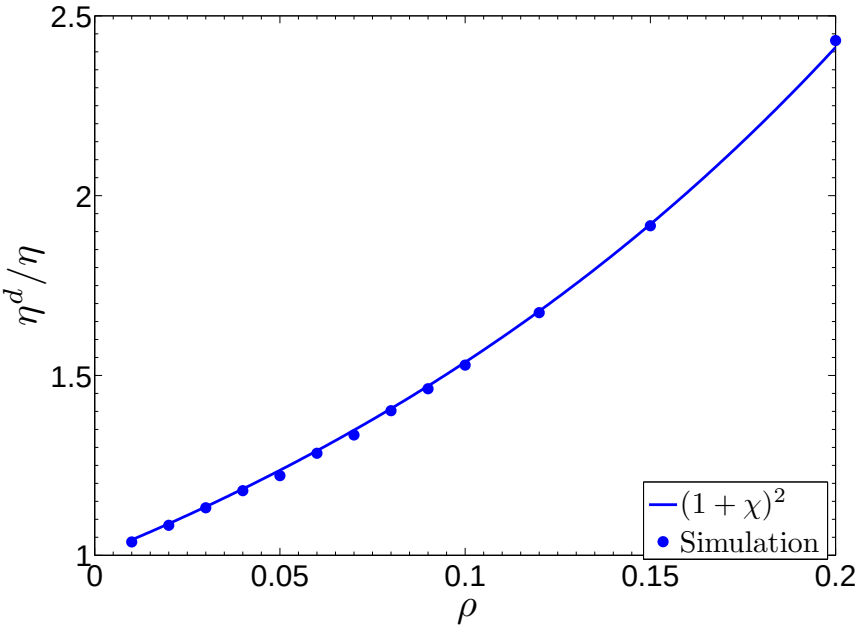

Figure 5.7: *Plot of viscosity ratio (dense gas to the original system) with density. From theory of the dense gas algorithm presented in section 5.3, this value is expected to be* $(1+\chi)^2$.

5.7 Condensation of a gas: single component two phase system

As discussed in section 5.4, Eq.(5.31) is the kinetic model for the multiphase system. In this section, phase coexistence curve is computed using this model. The Laplacian and the gradient of the potential term V_m in the Vlasov type force are calculated using second-order central differencing schemes. We can calculate a' using critical properties of Carnahan-Starling equation of state as, $a' = 2.560 T_c b$ (Eq.(5.14)). The value of κ can be predicted using a', $\kappa = \hat{\kappa} a'$, where $\hat{\kappa}$ is an order one quantity. In simulations the value of $\hat{\kappa}$ is set to 10.

In order to reduce density fluctuations, running time average was taken for the density over three time steps. Furthermore, smaller value for τ is used, $\tau = 0.1$. No phase separation was observed when τ is comparatively larger or smaller than 0.1. Simulations also showed large temperature variations in the system. In order to perform the simulation at fixed temperature, a simple thermostats was used (see Chapter 3). It was observed that the time step restrictions became less severe for simulations. Moreover, It was found that the the two density bounds, and their ratio became consistent with Maxwell construction. We have studied a single component two phase system for different values of T/T_c ranging from 0.98 to 0.60, and lower and higher densities in the system are reported. For $T/T_c < 0.6$, the two densities corresponding to liquid

and gas phases of the system start deviating from the theory. Thus we have been able to produce maximum of liquid to gas phase density ratio of about 140, corresponding to $T/T_c = 0.60$. In Fig.(5.8) obtained densities are plotted and is shown to be in excellent agreement with Maxwell construction for the Carnahan-Starling equation of state.

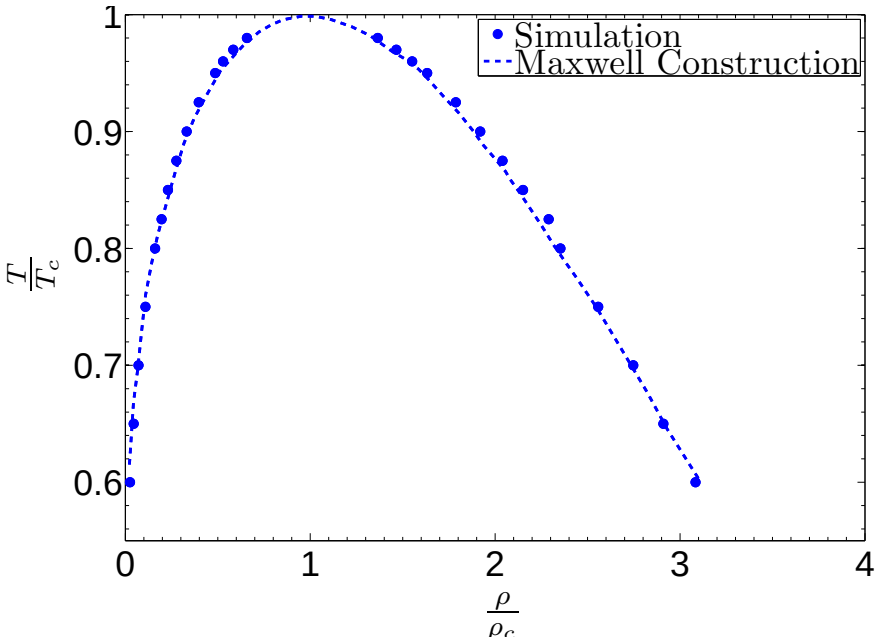

Figure 5.8: *Plot of* $\frac{\rho}{\rho_c}$ *with* $\frac{T}{T_c}$ *using PBCM-Subcell*

The shape of the separated phases is such that it tries to minimize the free energy. In present simulations (in $3D$) we observe shapes depend on ρ/ρ_c values. For smaller values of ρ (towards ρ_{min}), we do observe spherical bubbles, but for larger values of ρ (towards ρ_{max}) flat surfaces are found in the phase separated system. In the intermediate range of ρ cylindrical surfaces or combination of cylindrical surface with either flat or spherical surfaces can be observed. This behaviour can be explained based on the volume of the liquid phase in the separated state. A smaller value of ρ corresponds to a smaller volume for the liquid, and a spherical shape is possible which gives lowest energy for the system. As the density in the simulation increases, the volume corresponding to the liquid phase also increases. However, the spherical shape becomes infeasible cylindrical structure is formed. Similarly, at higher densities only flat surfaces are possible (Fig.(5.9)). In Fig.(5.10) contour plots have been shown at different sections (corresponding to Fig.(5.9c)) along z-axis which clearly shows 1D type of phase separation for large density values. We have also extracted density variations as we traverse from liquid region to gas region to liquid region in the domain along a given x-direction by keeping y and z coordinates fixed. Fig.(5.10b) shows the obtained density curve. From 1D phase separation problem, it is well understood that the density profile is tan-hyperbolic in x. We fit following curve to the density data

$$\rho(x) = \frac{\rho_L - \rho_G}{2} - \frac{\rho_L + \rho_G}{2} \tanh\left(\frac{x - x_0}{k}\right), \tag{5.47}$$

where ρ_L and ρ_G are liquid and gas phase densities, respectively; k and x_0 are unknown parameters dependent on the physical property of the system. Only one part of the curve (Fig.(5.10b))

with liquid to gas density variation is used for the fit (Fig.(5.11)), and a good fit is obtained with Eq.(5.47). The values of the two parameters extracted by the fit are $k = 9.5354$ and $x_0 = 59.5942$.

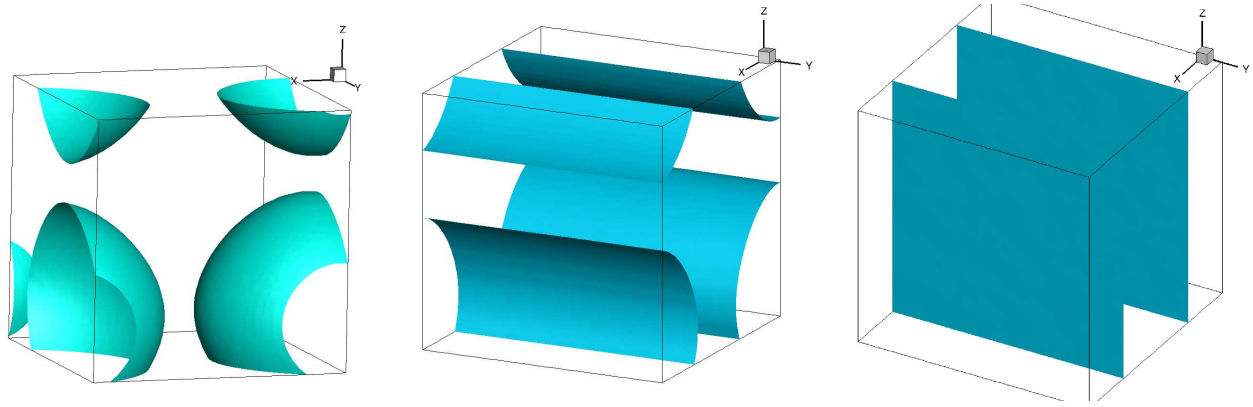

(a) (b) (c)

Figure 5.9: *Plot of density iso-surfaces at different* ρ/ρ_c*;* $T/T_c = 0.65$*. (a)* $\rho/\rho_c = 0.80$ *(b)* $\rho/\rho_c = 1.04$ *(c)* $\rho/\rho_c = 1.40$

We also note that for simulations at lower ρ values, the values for lower and upper densities show slightly overestimated values compared to higher ρ simulations. Also, comparatively larger temperature variations can be observed in small ρ simulations which is almost constant in simulations at large ρ values.

5.8 Outlook

Performance of a phenomenological mean field model for incorporating excluded volume effect in a system comprising point particles is studied using standard and pseudo binary collision models for MPCD. Numerical measurements of pressure, sound speed, and viscosity at different densities show good agreement with the theory. In addition, attraction between the molecules is also included as a Vlasov type force on the particles and a single component two phase system is studied. Densities of the two separated phases are measured and are shown to be in excellent agreement with the theory. Maximum density ratio of 140 is obtained in simulations. It can be noted that liquid-gas phase simulation of water still remains unattainable for which required density ration is of the order of 1000. Moreover, with better discrete Laplacian and divergence operators maximum liquid to gas density ratios can be further improved in the present scenario.

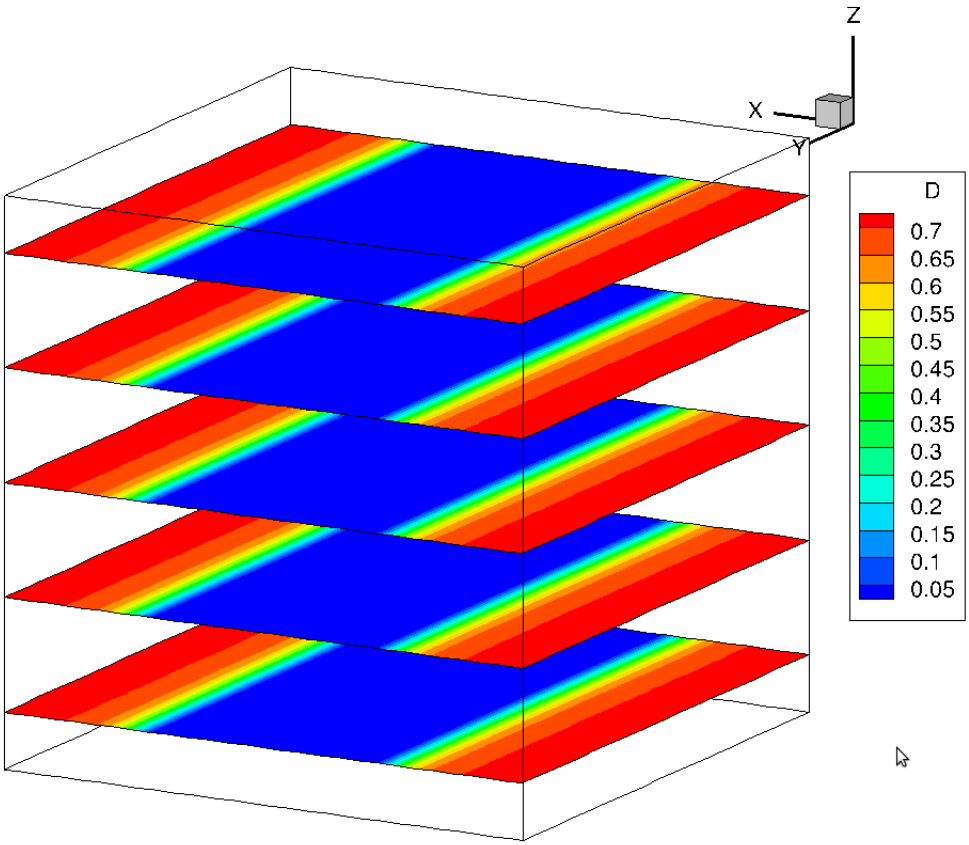

(a)

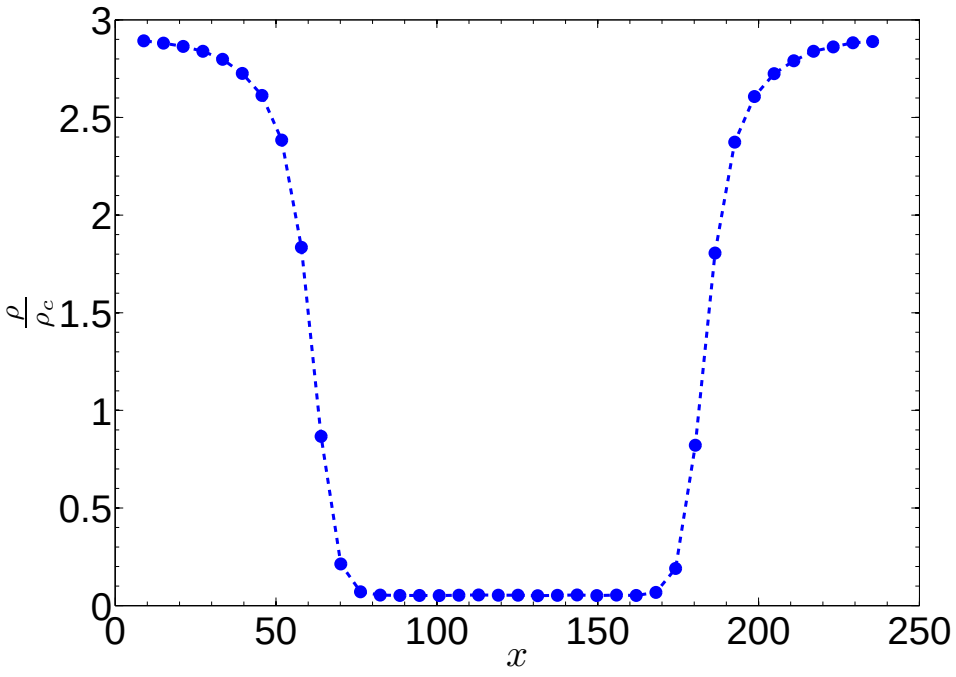

(b)

Figure 5.10: $\rho/\rho_c = 0.35$; $T/T_c = 0.65$. *(a) density contour (b) density plot with* x

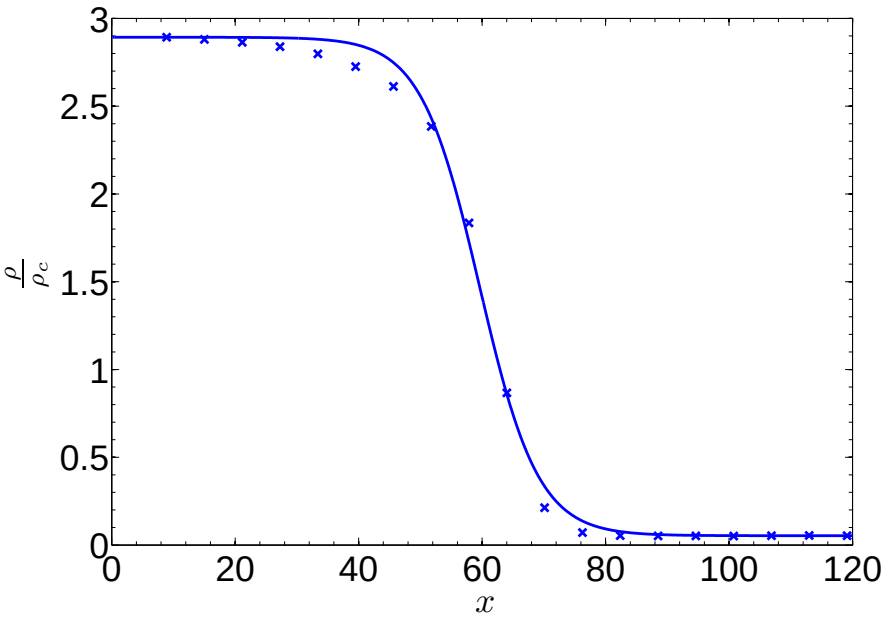

Figure 5.11: *Plot of* $\frac{\rho}{\rho_c}$ *with* x *(in* $(\times)$*) for the first half of curve in Fig.(5.10b) and in solid line we have a* tanh *curve fit of the form* $\rho(x) = (\frac{\rho_L - \rho_G}{2}) - (\frac{\rho_L + \rho_G}{2}) \tanh(\frac{x - x_0}{k})$*;* $\frac{T}{T_c} = 0.65$

Chapter 6
Outlook

In this thesis an attempt is made to address some of the technical issues with MPCD algorithm. Firstly, the range of applicability of this algorithm is studied for finite Knudsen flows using canonical flow set-ups such as shear driven flows, gravity driven flows, and pressure driven flows. It has been shown that the method can be used for simulating flows with Kn < 0.1. In this range of Knudsen, shear and gravity driven flows show good quantitative agreement for the velocity profile with that of Navier-Stokes solution using second order velocity-slip boundary condition and the DSMC data. Moreover, mass flow rate as a function of Knudsen number is obtained for gravity driven flows, and shows good quantitative agreement with the theory and DSMC predictions. Temperature profiles from gravity driven flows are also contrasted with DSMC data, but only qualitative comparison has been found. Further investigation is needed in order to understand the different thermal behaviour of MPCD algorithm compared to DSMC, which is a standard tool for studying finite Knudsen flows. Simulation of Poiseuille flows (pressure driven flows) show linear pressure distribution along the length of channel as opposed to the non-linear pressure profiles found in the experiments. This suggests that compressibility effect, which is commonly observed in microflows, is not captured appropriately. This can be explained considering the fact that MPCD algorithm operates for Reynolds number (Re) in the range 1-10. However, the observed Re in pressure driven microflows is much smaller. Further study of Poiseuille flow for small Re is therefore required.

Here, we have also proposed a new collision model (pseudo binary collision model) in order to remove the restriction on the small time step for simulations using standard MPCD. The standard MPCD system shows anomalous behaviour for small time steps, and it is more pronounced for the systems at low temperatures. Failure in ensuring the Galilean invariance is believed to be reason for this behaviour. In the case of MPCD multiparticle collisions, the same set of particles undergo collisions over multiple time steps, and this leads to building up of the velocity correlations among the particles. As a result, the satisfaction of Galilean invariance is violated. In pseudo binary collision model, only binary collisions are considered between randomly chosen pair of particles. It is clear that selecting the same pair of particles over multiple time steps is quite unlikely, and so the problem of particles developing velocity correlations is remedied. Here, flexibility in choosing small time steps for simulations is confirmed by numerical simulations. We have also studied equilibrium velocity distribution with pseudo binary collision model, and found that, like standard MPCD, it is Maxwellian. Analytical expressions for predicting the viscosities with pseudo binary collision model have been derived by following the kinetic theory arguments used for standard MPCD. Though the derived expressions show good agreement when rotation angle, $\alpha > 90^0$, a more rigorous derivation and numerical validation is still needed. Microflows with different canonical flow arrangements (shear, gravity, and pressure

driven) are also studied with the new collision model. We find that the obtained results are quite similar to standard MPCD results.

Finally, we have studied the equation of state aspect of MPCD. It can be noted that MPCD is commonly used to incorporate hydrodynamic interactions into complex systems, where liquid like properties are desirable for modeling solvents. However, ideality suggests that the system is easily compressible and there is a need to modify the equation of state of the system. Here, we have used a phenomenological mean field model for including excluded volume effect into the system. Pressure, viscosity, and sound speed are studied by changing densities in the modified system and show good agreement with the theory. Further, the effect of attraction between the molecules is also included as Vlasov type force acting on the molecules. This modification has allowed the study of a single component two phase system, e.g. condensation of a gas into liquid. The observed densities of the liquid and gas in the phase separated system is contrasted with the theory and excellent agreement has been found. A maximum liquid to gas density ratio of about 140 is achieved in present simulations.

References

Alexander, F. J. & Garcia, A. L. 1997 The direct simulation monte carlo method. *Computers in Physics* **11** (6), 588.

Alexander, F. J., Garcia, A. L. & Alder, B. J. 1995 A consistent boltzmann algorithm. *Physical review letters* **74** (26), 5212.

Allahyarov, E. & Gompper, G. 2002 Mesoscopic solvent simulations: Multiparticle-collision dynamics of three-dimensional flows. *Physical Review E* **66** (3), 036702.

Ansumali, S. 2011 Mean-field model beyond boltzmann-enskog picture for dense gases. *Communication in Computational Physics* **9**, 1106–1116.

Ansumali, S. & Karlin, I. V. 2002 Kinetic boundary conditions in the lattice boltzmann method. *Physical Review E* **66** (2), 026311.

Ansumali, S., Karlin, I. V., Arcidiacono, S., Abbas, A. & Prasianakis, N. I. 2007 Hydrodynamics beyond navier-stokes: Exact solution to the lattice boltzmann hierarchy. *Physical review letters* **98** (12), 124502.

Ansumali, S., Karlin, I. V., Frouzakis, C. E. & Boulouchos, K. 2006 Entropic lattice boltzmann method for microflows. *Physica A: Statistical Mechanics and its Applications* **359**, 289–305.

Arkilic, E. B., Schmidt, M. A. & Breuer, K. S. 1997 Gaseous slip flow in long microchannels. *Microelectromechanical Systems, Journal of* **6** (2), 167–178.

Beskok, A. & Karniadakis, G. E. 1994 Simulation of heat and momentum transfer in complex microgeometries. *Journal of Thermophysics and Heat transfer* **8** (4), 647–655.

Beskok, A. & Karniadakis, G. E. 1999 Report: a model for flows in channels, pipes, and ducts at micro and nano scales. *Microscale Thermophysical Engineering* **3** (1), 43–77.

Beskok, A., Karniadakis, G. E. & Trimmer, W. 1996 Rarefaction and compressibility effects in gas microflows. *Journal of Fluids Engineering* **118** (3), 448–456.

Bird, G. A. 1994 Molecular gas dynamics and the direct simulation of gas flows .

Bolintineanu, D. S., Lechman, J. B., Plimpton, S. J. & Grest, G. S. 2012 No-slip boundary conditions and forced flow in multiparticle collision dynamics. *Physical Review E* **86** (6), 066703.

Callen, H. B. 2006 *Thermodynamics and an introduction to thermostatistics*. John Wiley & Sons.

Carnahan, N. F. & Starling, K. E. 1969 Equation of state for nonattracting rigid spheres. *The Journal of Chemical Physics* **51** (2), 635–636.

Cercignani, C. 1975 *Theory and application of the Boltzmann equation*, , vol. 701120819. Scottish Academic Press Edinburgh.

Chapman, S., Cowling & Thomas, G. 1970 *The mathematical theory of non-uniform gases: an account of the kinetic theory of viscosity, thermal conduction and diffusion in gases*. Cambridge university press.

Chen, S., Martinez, D. & Mei, R. 1996 On boundary conditions in lattice boltzmann methods. *Physics of Fluids (1994-present)* **8** (9), 2527–2536.

Czerwinska, J. & Adams, N. A. 2003 Numerical modeling of micro-channel flows by a dpd method. In *ASME/JSME 2003 4th Joint Fluids Summer Engineering Conference*, pp. 909–914. American Society of Mechanical Engineers.

De Angelis, E., Chinappi, M. & Graziani, G. 2012 Flow simulations with multi-particle collision dynamics. *Meccanica* **47** (8), 2069–2077.

Gompper, G., Ihle, T., Kroll, D. M. & Winkler, R. G. 2008 Multi-particle collision dynamics: a particle-based mesoscale simulation approach to the hydrodynamics of complex fluids .

Hadjiconstantinou, N. G. 2003 Comment on cercignani's second-order slip coefficient. *Physics of Fluids (1994-present)* **15** (8), 2352–2354.

Hadjiconstantinou, N. G. & Garcia, A. L. 2001 Molecular simulations of sound wave propagation in simple gases. *Physics of Fluids (1994-present)* **13** (4), 1040–1046.

He, X. & Doolen, G. D. 2002 Thermodynamic foundations of kinetic theory and lattice boltzmann models for multiphase flows. *Journal of Statistical Physics* **107** (1-2), 309–328.

Hecht, M., Harting, J., Bier, M., Reinshagen, J. & Herrmann, H. J. 2006 Shear viscosity of claylike colloids in computer simulations and experiments. *Physical Review E* **74** (2), 021403.

Hecht, M., Harting, J., Ihle, T. & Herrmann, H. J. 2005 Simulation of claylike colloids. *Physical Review E* **72** (1), 011408.

Ho, C.-M. & Tai, Y.-C. 1998 Micro-electro-mechanical-systems (mems) and fluid flows. *Annual Review of Fluid Mechanics* **30** (1), 579–612.

Ihle, T. 2009 Chapman–enskog expansion for multi-particle collision models. *Physical Chemistry Chemical Physics* **11** (42), 9667–9676.

Ihle, T. & Kroll, D. 2001 Stochastic rotation dynamics: a galilean-invariant mesoscopic model for fluid flow. *Physical Review E* **63** (2), 020201.

Ihle, T. & Kroll, D. M. 2003*a* Stochastic rotation dynamics. i. formalism, galilean invariance, and green-kubo relations. *Physical Review E* **67** (6), 066705.

Ihle, T. & Kroll, D. M. 2003*b* Stochastic rotation dynamics. ii. transport coefficients, numerics, and long-time tails. *Physical Review E* **67** (6), 066706.

Ihle, T., Tüzel, E. & Kroll, D. M. 2006 Consistent particle-based algorithm with a non-ideal equation of state. *EPL (Europhysics Letters)* **73** (5), 664.

Kapral, R. 2008 Multiparticle collision dynamics: simulation of complex systems on mesoscales. *Advances in Chemical Physics* **140**, 89.

Karniadakis, G. E., Beskok, A. & Gad-el Hak, M. 2002 Micro flows: fundamentals and simulation. *Applied Mechanics Reviews* **55**, 76.

Kikkinides, E. S., Yiotis, A. G., Kainourgiakis, M. E. & Stubos, A. K. 2008 Thermodynamic consistency of liquid-gas lattice boltzmann methods: Interfacial property issues. *Physical Review E* **78** (3), 036702.

Kikuchi, N., Pooley, C. M., Ryder, J. F. & Yeomans, J. M. 2003 Transport coefficients of a mesoscopic fluid dynamics model. *The Journal of chemical physics* **119** (12), 6388–6395.

Kikuchi, N., Ryder, J. F., Pooley, C. M. & Yeomans, J. M. 2005 Kinetics of the polymer collapse transition: the role of hydrodynamics. *Physical Review E* **71** (6), 061804.

Lamura, A., Gompper, G., Ihle, T. & Kroll, D. M. 2001 Multi-particle collision dynamics: Flow around a circular and a square cylinder. *EPL (Europhysics Letters)* **56** (3), 319.

Landau, L. D. & Lifshitz, E. M. 2013 *Fluid Mechanics: Landau and Lifshitz: Course of Theoretical Physics*, , vol. 6. Elsevier.

Lee, S. H. & Kapral, R. 2006 Mesoscopic description of solvent effects on polymer dynamics. *The Journal of chemical physics* **124** (21), 214901.

Liboff, R. L. 1983 *Kinetic theory*. Springer.

Lifshitz, E. M. & Pitaevskii, L. P. 1981 *Physical kinetics*. Butterworth Heinemann.

Lim, C. Y., Shu, C., Niu, X. D. & Chew, Y. T. 2002 Application of lattice boltzmann method to simulate microchannel flows. *Physics of Fluids (1994-present)* **14** (7), 2299–2308.

Liu, M., Meakin, P. & Huang, H. 2006 Dissipative particle dynamics with attractive and repulsive particle-particle interactions. *Physics of Fluids (1994-present)* **18** (1), 017101.

Malevanets, A. & Kapral, R. 1999 Mesoscopic model for solvent dynamics. *The Journal of chemical physics* **110** (17), 8605–8613.

Malevanets, A. & Kapral, R. 2000 Solute molecular dynamics in a mesoscale solvent. *The Journal of Chemical Physics* **112** (16), 7260–7269.

McQuarrie, D. A. 1976 *Statistical mechanics*. Happer and Row, New York.

Mussawisade, K., Ripoll, M., Winkler, R. G. & Gompper, G. 2005 Dynamics of polymers in a particle-based mesoscopic solvent. *The Journal of chemical physics* **123** (14), 144905.

Nanbu, K. 1997 Theory of cumulative small-angle collisions in plasmas. *Physical Review E* **55** (4), 4642.

Nie, X., Doolen, G. D. & Chen, S. 2002 Lattice-boltzmann simulations of fluid flows in mems. *Journal of Statistical Physics* **107** (1-2), 279–289.

Noguchi, H. & Gompper, G. 2005*a* Dynamics of fluid vesicles in shear flow: Effect of membrane viscosity and thermal fluctuations. *Physical Review E* **72** (1), 011901.

Noguchi, H. & Gompper, G. 2005*b* Shape transitions of fluid vesicles and red blood cells in capillary flows. *Proceedings of the National Academy of Sciences of the United States of America* **102** (40), 14159–14164.

Oran, E. S., Oh, C. & Cybyk, B. Z. 1998 Direct simulation monte carlo: Recent advances and applications 1. *Annual Review of Fluid Mechanics* **30** (1), 403–441.

Padding, J. T. & Louis, A. A. 2006 Hydrodynamic interactions and brownian forces in colloidal suspensions: Coarse-graining over time and length scales. *Physical Review E* **74** (3), 031402.

Padding, J. T., Wysocki, A., Löwen, H. & Louis, A. A. 2005 Stick boundary conditions and rotational velocity auto-correlation functions for colloidal particles in a coarse-grained representation of the solvent. *Journal of Physics: Condensed Matter* **17** (45), S3393.

Piekos, E. S. & Breuer, K. S. 1996 Numerical modeling of micromechanical devices using the direct simulation monte carlo method. *Journal of Fluids Engineering* **118** (3), 464–469.

Pong, K.-C., Ho, C.-M., Liu, J. & Tai, Y.-C. 1994 Non-linear pressure distribution in uniform microchannels. *ASME-PUBLICATIONS-FED* **197**, 51–51.

Pooley, C. M. & Yeomans, J. M. 2005 Kinetic theory derivation of the transport coefficients of stochastic rotation dynamics. *The Journal of Physical Chemistry B* **109** (14), 6505–6513.

Rapaport, D. C. 2004 *The art of molecular dynamics simulation*. Cambridge university press.

Ripoll, M., Mussawisade, K., Winkler, R. G. & Gompper, G. 2005 Dynamic regimes of fluids simulated by multiparticle-collision dynamics. *Physical Review E* **72** (1), 016701.

Ryder, J. F. & Yeomans, J. M. 2006 Shear thinning in dilute polymer solutions. *The Journal of chemical physics* **125** (19), 194906.

Shan, X. & Chen, H. 1993 Lattice boltzmann model for simulating flows with multiple phases and components. *Physical Review E* **47** (3), 1815.

Shan, X. & Chen, H. 1994 Simulation of nonideal gases and liquid-gas phase transitions by the lattice boltzmann equation. *Physical Review E* **49** (4), 2941.

Succi, S. 2001 *The lattice Boltzmann equation: for fluid dynamics and beyond*. Oxford university press.

Suryanarayanan, S., Singh, S. & Ansumali, S. 2013 Extended bgk boltzmann for dense gases. *Communication in Computational Physics* **13** (3), 629–648.

Takizuka, T. & Abe, H. 1977 A binary collision model for plasma simulation with a particle code. *Journal of Computational Physics* **25** (3), 205–219.

Tucci, K. & Kapral, R. 2004 Mesoscopic model for diffusion-influenced reaction dynamics. *The Journal of chemical physics* **120** (17), 8262–8270.

Van Beijeren, H. & Ernst, M. H. 1973 The modified enskog equation. *Physica* **68** (3), 437–456.

Wang, C., Lin, T., Caflisch, R., Cohen, B. I. & Dimits, A. M. 2008 Particle simulation of coulomb collisions: Comparing the methods of takizuka & abe and nanbu. *Journal of Computational Physics* **227** (9), 4308–4329.

Whitmer, J. K. & Luijten, E. 2010 Fluid–solid boundary conditions for multiparticle collision dynamics. *Journal of Physics: Condensed Matter* **22** (10), 104106.

Yudistiawan, W. P., Ansumali, S. & Karlin, I. V. 2008 Hydrodynamics beyond navier-stokes: The slip flow model. *Physical Review E* **78** (1), 016705.

Yudistiawan, W. P., Kwak, S. K., Patil, D. V. & Ansumali, S. 2010 Higher-order galilean-invariant lattice boltzmann model for microflows: Single-component gas. *Physical Review E* **82** (4), 046701.

Zheng, Y., Garcia, A. L. & Alder, B. J. 2002 Comparison of kinetic theory and hydrodynamics for poiseuille flow. *Journal of Statistical Physics* **109** (3-4), 495–505.